# 北京理工大学

# 新体系教师聘期(中期)考核附件材料

姓　　名：_____白阳_____

现聘岗位：_____预聘助理教授_____

所在学科：_____材料科学与工程_____

研究方向：_____材料物理与化学_____

所在单位：_____材料学院_____

填表时间：____2021____年____9____月____3____日

# 目录

FULL PAPER

ADVANCED
ENERGY
MATERIALS

www.advenergymat.d

Check for
updates

# 1000 h Operational Lifetime Perovskite Solar Cells by Ambient Melting Encapsulation

*Sai Ma, Yang Bai, Hao Wang, Huachao Zai, Jiafeng Wu, Liang Li, Sisi Xiang, Na Liu, Lang Liu, Cheng Zhu, Guilin Liu, Xiuxiu Niu, Haining Chen, Huanping Zhou, Yujing Li,\* and Qi Chen\**

Improving device lifetime is one of the critical challenges for the practical use of metal halide perovskite solar cells (PSCs), wherein a reliable encapsulation is indispensable. Herein, based on an in-depth understanding of the degradation mechanism for the PSCs, a solvent-free and low-temperature melting encapsulation technique, by employing low-cost paraffin as the encapsulant that is compatible with perovskite absorbers, is demonstrated. The encapsulation strategy enables the full encapsulating operations to be undertaken under an ambient environment. It is found that the strategy not only removes residual oxygen and moisture to prevent the perovskite from phase segregation, but also suppresses the species volatilization to impede absorber decomposition, enabling a PSC devices with good thermal and moisture stability. As a result, the as-encapsulated PSCs achieve a 1000 h operational lifetime for the encapsulated device at continuous maximum power point output under an ambient environment. This work paves the way for scalable and robust encapsulation strategy feasible to hybrid perovskite optoelectronics in an economic manner.

## 1. Introduction

Hybrid organic–inorganic perovskite compounds have attracted tremendous attention in the field of photovoltaic (PV) research due to their superior properties such as efficient light-harvesting, tunable band structure, long carrier diffusion length, low defect density, etc.[1] Due to these characteristics, the power conversion efficiency (PCE) of perovskite solar cells (PSCs) has already exceeded 25% in 2019, starting from only 3.8% in the first publication in 2009.[1a,2] In addition, PSCs require simple processing and low fabrication cost, and thus render them great potential for commercialization.[3] However, beyond such unique and exhilarating advantages, the perovskites suffered from the stability issue which hinders their pace toward commercialization.[4]

For commercial solar cells, efficiency, lifetime, and cost are the three most critical parameters. With very competitive efficiency, the cost of perovskite solar cells is just around half of the silicon solar cell, whereas their lifetime is the main issue.[5] Therefore, enhancing the long-term stability to prolong the lifetime is the first priority for PSCs development. Recently, many chemistry strategies including doping, compositional engineering, dimensional engineering, grain boundary modification, and functional transporting material design have been employed to solve the intrinsic instability issues like ion migration, thermal decomposition/phase transition, and hygroscopicity of perovskite materials.[6] However, the improvement effect is still limited, especially when exposing the cells to the ambient environment and continuous operation condition.[7] The ionic crystal behavior and the composition feature are the two main factors that make the perovskite material sensitive to the main species in ambient condition, especially the oxygen and moisture, resulting in the fast degradation of material as well as the device performance.[8] Isolating the PSCs from these species is essential in protecting them from the environment-induced degradation.

Encapsulation, so far, has been widely used in the commercialized electronic devices, which was also employed in the PSCs and showed obvious enhancement on the device stability.[9] Dong et al. compared three kinds of commonly used encapsulation material, UV-curable adhesive (UVCA), "AB"

S. Ma, Dr. Y. Bai, H. Wang, H. Zai, J. Wu, N. Liu, L. Liu, C. Zhu, X. Niu, Prof. Y. Li, Prof. Q. Chen
Beijing Key Laboratory of Nanophotonics and Ultrafine Optoelectronic Systems
School of Materials Science and Engineering
Beijing Institute of Technology
Beijing 100081, P. R. China
E-mail: yjli@bit.edu.cn; qic@bit.edu.cn
S. Ma, Dr. Y. Bai, H. Wang, H. Zai, J. Wu, N. Liu, L. Liu, C. Zhu, X. Niu, Prof. Y. Li, Prof. Q. Chen
Experimental Center of Advanced Materials
School of Materials Science and Engineering
Beijing Institute of Technology
Beijing 100081, P. R. China
L. Li, Prof. H. Zhou
Department of Materials Science and Engineering
College of Engineering
Peking University
Beijing 100871, P. R. China
S. Xiang, Dr. H. Chen
School of Materials Science and Engineering
Beihang University
Beijing 100191, P. R. China
Prof. G. Liu
School of Science
Jiangnan University
Wuxi, Jiangsu 214122, P. R. China

The ORCID identification number(s) for the author(s) of this article can be found under https://doi.org/10.1002/aenm.201902472.

epoxy, and the thermal curable epoxy, and demonstrated that the UVCA resulted in the best postprocessing efficiency and device stability.[9d] However, Han et al. demonstrated that the direct contact of UVCA and PSCs should be avoided, because the outgassed vapor of UVCA could damage the perovskite during the UV-curing. They suggested that the UVCA encapsulation should only be applied at the edge.[9e] Shi et al. found that a void space should be avoided around the device during the encapsulation, because it provided enough space for the volatile species to escape from the perovskite due to the decomposition.[9c] So far, several encapsulation strategies have been employed to PSCs, but one crucial problem still remains in that the typically used encapsulants cannot meet the goal of long-term stability. For the encapsulants used for PSC devices, in addition to their intrinsic long-term stability, it must also meet four requirements: 1) chemically inert when exposing to the materials used in solar cell devices to enable the direct contact with the cell to avoid the species volatilization; 2) solvent-free or at least no damaging solvent involved during the encapsulation procedure due to the fact that the perovskite material and organic transporting materials are sensitive to most of the organic solvents; 3) low-temperature processability, because the poor thermal stability of perovskite demands the encapsulation processes no higher than 150–170 °C; 4) a low water vapor transmission rate (WVTR) to effectively prevent the invasion of moisture. Besides, the cost and ambient processibility for encapsulation are also equally important for the mass production.

In this work, we demonstrated the advantages of a solvent-free and low-temperature processing encapsulation strategy for the PSC, on the merit of a low-cost encapsulation material, paraffin. Its unique solvent-free and low-temperature processability is compatible with perovskite absorber, which enables the processing at ambient condition with scalability. Besides, the nonpolar paraffin can effectively remove the residue oxygen

and moisture during the encapsulation, prevent the perovskite from phase segregation, and suppresses the volatilization of perovskite to impede absorber decomposition. Bearing these advantages, the encapsulated devices display a superior stability by retaining over 80% of the original efficiency over 1000 h continuous test at the maximum power point (MPP) under ambient condition.

## 2. Results and Discussions

### 2.1. Oxygen- and Moisture-Induced Accelerated Phase Segregation

In this study, we employed the mixed-cation mixed-halide perovskite with formula of $Rb_{0.09}Cs_{0.05}[(FA_{0.85}MA_{0.15})Pb(I_{0.85}Br_{0.15})_3]$ (RbCsFAMA).[10] **Figure 1**a,b shows the scanning electron microscopy (SEM) image of perovskite films before and after aging under illumination for 60 min in the ambient environment with relative humidity of 25–35% RH and temperature of 20–25 °C without encapsulation. It can be seen from the SEM images that the aged perovskite film suffered from obvious morphology change, wherein irregular bright regions appeared on the surface, indicating a strong composition change of the film.[11]

To achieve a longer lifetime, UVCA was used for device encapsulation. However, it was found that the UVCA-encapsulated devices still suffered from oxygen- and moisture-induced degradation. As shown in Figure 1c,d, in the UVCA-encapsulated devices, the perovskite films also show a phase segregation after continuous illumination. The device encapsulated in $N_2$ (Figure 1c) exhibits weaker phase segregation than the one encapsulated in ambient environment (Figure 1d). Figure 1d shows large irregular spots with size over 3 μm, which may result from the formation of new phases or the
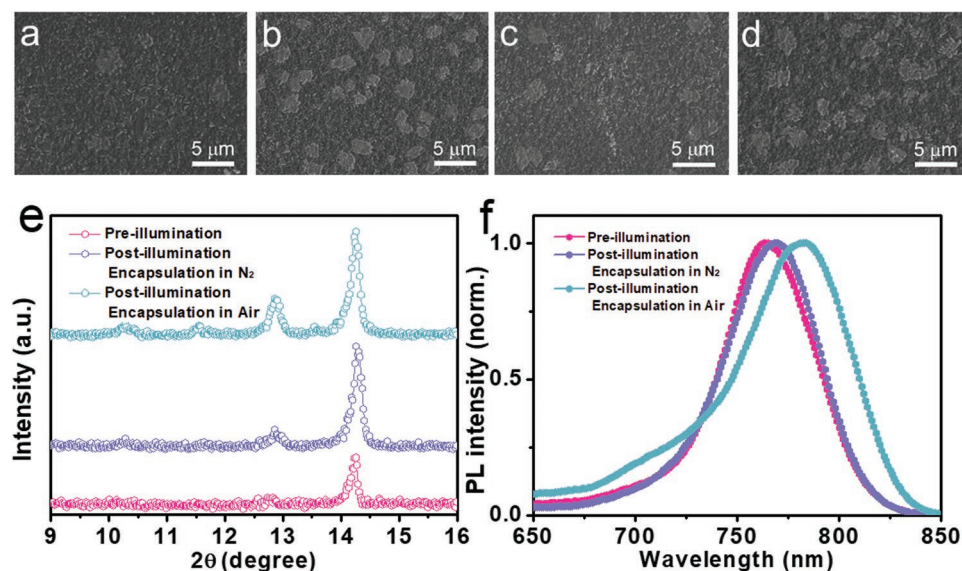


**Figure 1.** The top-view SEM images of perovskite films, a) fresh sample, b) unencapsulated sample, UVCA-encapsulated film in c) $N_2$ and d) ambient environment. (b)–(d) were aged under illumination in ambient environment for 1 h. e) XRD patterns and f) steady-state PL spectra of perovskite film samples prepared under different conditions.

**ADVANCED
SCIENCE NEWS**

www.advancedsciencenews.com

**ADVANCED
ENERGY
MATERIALS**

www.advenergymat.de

volatilized species induced decomposition. The above results unveil that the oxygen and moisture will strongly influence the morphology of perovskite film due to the phase segregation and decomposition.[8] Although the UVCA encapsulation can slow down this process, a more rigorous operation condition in inert atmosphere is demanded.

To further investigate the relationship between the morphology change and film composition, X-ray diffraction (XRD) and steady state photoluminescence (PL) were applied. From the XRD patterns in Figure 1e, only one peak around 14.25° ($2\theta$) can be detected in the fresh sample, which belongs to the diffraction of (110) lattice plane of RbCsFAMA perovskite.[10] However, a more obvious change occurred after 60 min illumination. For the sample encapsulated in $N_2$, two additional diffraction peaks appear at 10.26° and 12.70° which belong to RbPb$(I_{1-x}Br_x)_3$ and $PbI_2$, respectively, indicating the phase segregation and decomposition of original RbCsFAMA film.[11,12] If the film is encapsulated in ambient environment at heavy exposure level to moisture, the formation of RbPb$_2I_4$Br (around 11.5°) is detected after the aging process.[11] Besides, the change of intensity of (110) peak is also detected, which may be due to the thickness variation of different samples. The phase segregation phenomenon is also detected by grazing-incidence wide-angle X-ray scattering (GIWAXS) patterns as shown in Figure S1 (Supporting Information). Figure 1f presents the steady-state PL, which also confirms the phase segregation phenomenon. The $N_2$-encapsulated film shows a slightly redshift of the PL peak after the 60 min illumination, which can be attributed to the formation of I-rich phases. As a contrast, for the film encapsulated in ambient condition, a much stronger redshift of the PL peak is detected. Besides, several shoulder peaks at low wavelength region are also detected due to the formation of Br-rich phases. The above results reveal that the phase segregation phenomenon is due to the intrinsic properties of perovskite materials, and the exposure to ambient environment would accelerate this segregation process. More importantly, our demonstration indicates that the mostly used UVCA encapsulant could hardly suppress the phase segregation as the removal of residual oxygen and moisture is not efficient with this encapsulation strategy.[9c]

## 2.2. Inhibited Phase Segregation

Based on the requirements for PSCs in terms of long-term stability, a low-cost and perovskite-compatible material, paraffin, with a solvent-free and low-temperature protocol was proposed to investigate the feasibility of this encapsulation strategy for the PSCs.

Figure S2a,b (Supporting Information) shows the device encapsulation structure of UVCA with/without paraffin. Figure S2c,e (Supporting Information) shows the two-sided photo-image of device encapsulated by UVCA with paraffin. Figure S2d,f (Supporting Information) shows the two-sided photo-image of device encapsulated by UVCA without paraffin. Due to the incompatibility between PSCs and the solvent in UVCA (Figure S3, Supporting Information), the noncontact encapsulation is essential to avoid the direct contact between UVCA and the top of the PSCs. The composition of encapsulation gas is

depended on the fabrication condition, which typically consists of $N_2$, Ar, or air. For the encapsulation of UVCA with paraffin, since the paraffin is a solvent-free material and chemically inert to PSCs, it can be in direct contact with the device and hence forms a gas/vacuum-free encapsulation over the device. More importantly, this encapsulation strategy can directly remove the residue oxygen and moisture from device surface and enables the full encapsulating operation under ambient environment. For comparison, the PSCs devices were encapsulated by UVCA with paraffin and without paraffin under ambient environment, with details described in the Experimental Section.

To evaluate the phase segregation behavior of perovskite films in the UVCA with/without paraffin-encapsulated devices, the steady-state PL spectra tracking under continuous illumination are shown in **Figure 2**a,d. It is clearly seen that the UVCA without paraffin-encapsulated devices shows significant PL shifted from around 760 to 780 nm after only 3 h illumination, indicating the formation of an iodide-rich phase. Furthermore, after another 3 h illumination, the PL signal become broadened and shift to the lower wavelength region, which verify the formation of Br-rich phases or larger-bandgap species. As a contrast, in the UVCA with paraffin-encapsulated devices, the entire spectra show no significant changes within the same time frame.

The X-ray diffraction (XRD) measurements also confirm the results indicated from PL analysis. In Figure 2b, after 3 h continuous illumination, new phase like RbPb$(I_{1-x}Br_x)_3$ (10.26°) formed in the UVCA without paraffin-encapsulated PSCs, and another reflections around $2\theta = 11.55°$ belonging to RbPb$_2I_4$Br appeared after 6 h, which confirms the previous hypothesis that larger bandgap species formed.[11] Meanwhile, the XRD patterns of UVCA with paraffin-encapsulated device keep unchanged after 3 h illumination. However, after 6 h illumination, a new peak is detected on the XRD patterns (Figure 2e). As mentioned before, the perovskite intrinsically suffers from phase segregation, hence the formation of new phases can hardly be fully prohibited but can only be suppressed by reducing the exposure to oxygen and moisture.

In addition, the UV–vis absorption spectra also clearly identify the changes of the films after continuous illumination. In Figure 2c, the UV–vis spectra show that the light absorption within 400–600 nm significantly decreased along with the formation of a new absorption edge around 420 nm for UVCA without paraffin-encapsulated device, indicating a serious composition change and decomposition of the film. However, as shown in Figure 2f, UVCA with paraffin-encapsulated sample is much stable as the UV–vis absorbance only exhibits negligible change after 6 h illumination.

To further investigate the phase segregation behavior under different encapsulation strategies, the 2D PL maps were measured by using the confocal photoluminescence microscopy. **Figure 3**a–c shows the 2D PL maps changes of UVCA without paraffin-encapsulated devices. Obvious PL redshift can be seen on the perovskite film after 1 h illumination due to the formation of I-rich phases. The redshift becomes more obvious with the prolonged illumination time. More importantly, the scale of phase segregation on the film surface is around micrometer. As the I-rich region acts as the charge recombination sites, the microscale phase segregation would strongly influence the device performance as well as its stability, resulting in a
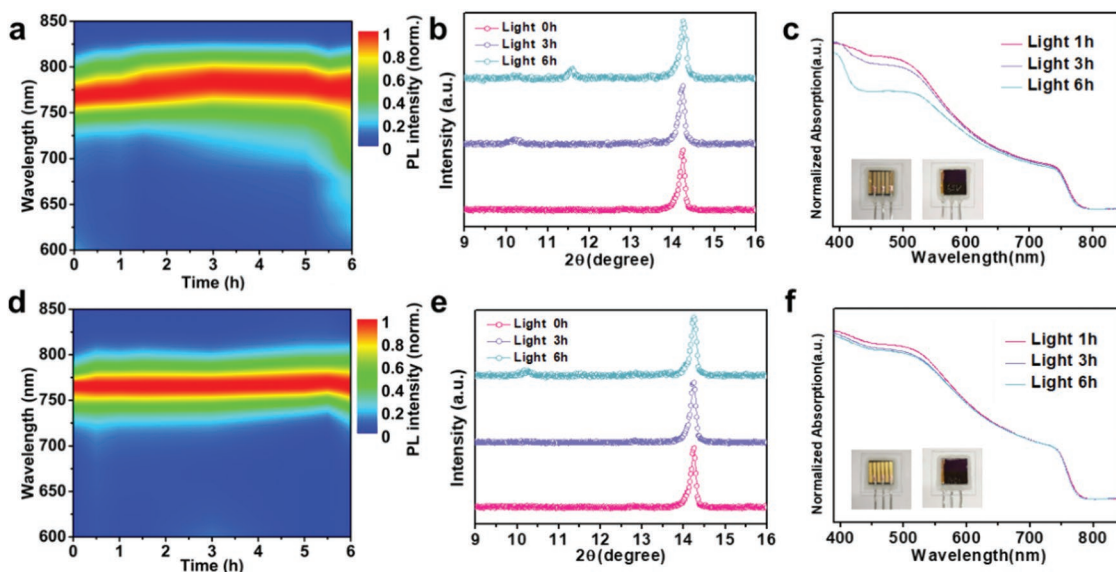
**ADVANCED
SCIENCE NEWS**

www.advancedsciencenews.com

**ADVANCED
ENERGY
MATERIALS**

www.advenergymat.de

**Figure 2.** The steady-state PL spectra of a) UVCA without paraffin and d) UVCA with paraffin encapsulation under continuous illumination. The XRD patterns of b) UVCA without paraffin and e) UVCA with paraffin encapsulation. The UV–vis absorption spectra of c) UVCA without paraffin and f) UVCA with paraffin encapsulation, and inset photos show devices after encapsulation from both sides.

fast degradation. In contrast, the film encapsulated by UVCA with paraffin shows no obvious change on the color of the PL maps, which are presented in Figure 3d–f, indicating the inhibited phase segregation. Due to the resolution of 2D PL maps is limited to 200 nm, it is hard to detect the phase segregation with smaller scale, but these results can prove that the phase segregation of UVCA with paraffin-encapsulated device is much weaker than that without paraffin-encapsulated device. What's more, the encapsulation strategy also works well for the perovskite films with composition of MAPbI$_3$ and FACsPbI$_3$, which is shown in Figures S4 and S5 (Supporting Information). We observed obvious PL shift in the UVCA without paraffin-encapsulated films than that with paraffin-encapsulated films after continuously illumination aging.

In addition, we also tracked the recovery of phase segregation process of the encapsulated perovskite film as shown in Figures S6 and S7 (Supporting Information). The 2D PL maps

in Figures S6d–f and S7d–f (Supporting Information) show that recovery of phase segregation in the UVCA without paraffin-encapsulated film is more harder than that with paraffin-encapsulated one, indicating that the better removal of ambient species like oxygen and moisture could not only suppress the phase segregation but also benefit the recovery of phase segregation.

Based on the above characterizations, the UVCA with paraffin encapsulation strategy presents great effect on inhibiting the film degradation and phase segregation. The solvent-free and low-temperature processability render them good compatibility with PSCs, while the nonpolar nature of paraffin makes it efficient in removing the residue oxygen and moisture during the ambient encapsulation process. Combining such unique properties, the UVCA with paraffin-encapsulated device shows drastically suppressed decomposition and phase segregation compared with that without paraffin-encapsulated device.
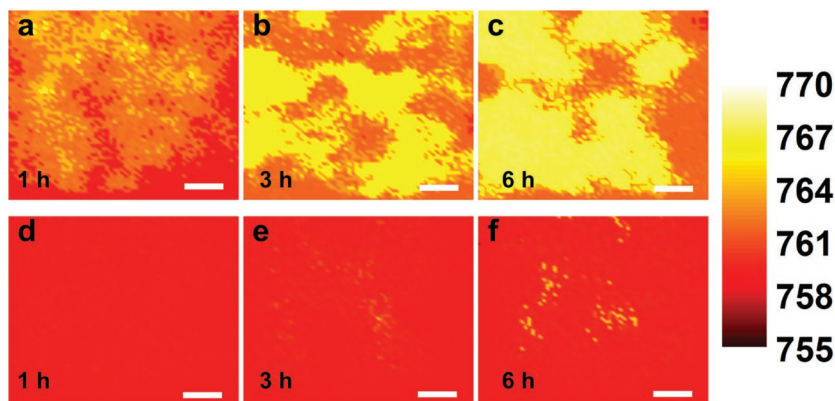


**Figure 3.** The 2D photoluminescence (PL) maps of perovskite films of continuous illumination with a–c) UVCA without paraffin encapsulation and d–f) UVCA with paraffin encapsulation in ambient environment. The scale bar is 1 µm.

## 2.3. Inhibited Water/Oxygen Intrusion and Defect Generation

The water contact angle was tracked to evaluate the waterproof ability of the two encapsulant. The contact angles of water on the UVCA and paraffin encapsulant are around 92.9° and 107.4°, respectively (**Figure 4**a,c), indicating that the paraffin is more hydrophobic than the UVCA. Interestingly, after exposure to water droplet for 5 min, the water contact angle of UVCA decreases to 59.2° (Figure 4b). The reduction of hydrophobicity may originate from the invasion of water as the UVCA holds a high WVTR value (Table S1, Supporting Information). With lower WVTR
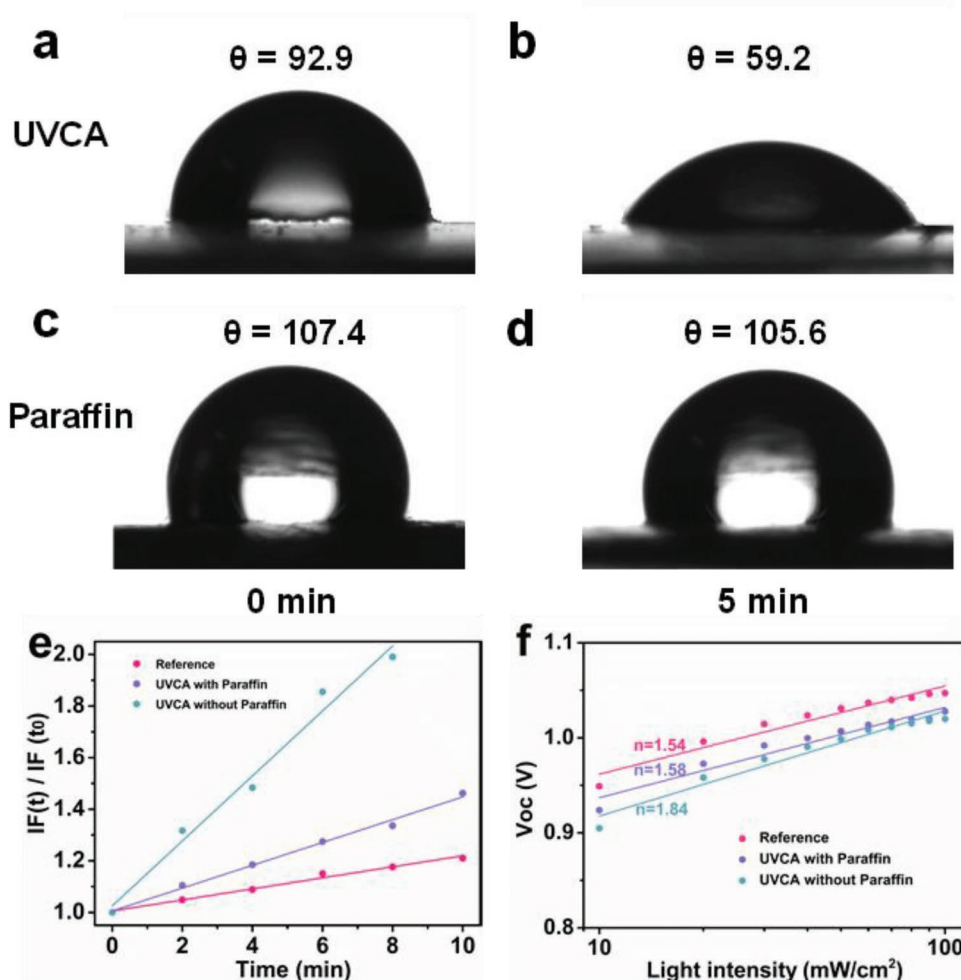
ADVANCED
SCIENCE NEWS
www.advancedsciencenews.com

ADVANCED
ENERGY
MATERIALS
www.advenergymat.de

**Figure 4.** The water contact angles of a,b) UVCA and c,d) paraffin before and after exposure to water for 5 min. e) Normalized fluorescence intensity at 610 nm of the superoxide probe solution, with excitation at 520 nm. $I_F(t)$ is the fluorescence intensity maximum at time $t$, while $I_F(t_0)$ is the background fluorescence intensity of the probe at $t = 0$. The ratio $I_F(t)/I_F(t_0)$ is a measure of the yield of superoxide generation. f) The light intensity dependent $V_{oc}$ of encapsulated devices after 6 h illumination, wherein the reference is the fresh device.

value and nonpolar nature, the paraffin only has a slightly change in the water contact angle, showing good hydrophobicity (Figure 4d).[9c,13] From the in situ water contact angle tracking, the paraffin encapsulant not only presents stronger waterproof ability due to its surface hydrophobic properties, but also has the ability to suppress the invasion of water, thus enables efficient removal of the oxygen and moisture even under the ambient environment.

The vacancy-type defects in perovskite film have been revealed as a crucial factor accelerating the degradation of perovskite material.[4a,b,14] The vacancies in perovskite act as shallow electronic traps, and the absorption of oxygen and moisture molecules at such shallow electronic traps is more favorable than at pristine surfaces, and hence accelerate perovskite degradation via the vacancy-assisted decomposition mechanism.[6a,8b] Meanwhile, the vacancies can be generated during the film decomposition and phase segregation. Therefore, the inhibited phase segregation and decomposition would also suppress the formation of vacancies, thus eliminates another vacancy-assisted decomposition pathway.

Superoxide anion is a key species generated at the vacancy sites of perovskite, and is responsible for the material decomposition. To quantify the formed vacancies within the perovskite film, a molecular fluorescent probe, hydroethidine (HE) probe was employed. HE probe is known to show a characteristic increase in emission at 610 nm upon exposure to the superoxide radical anion as reported in literatures.[6a,8b,15] The RbCsFAMA-based solar cells encapsulated by UVCA without/with paraffin were aged under illumination for 6 h before the test, followed by immersion into a $0.317 \times 10^{-3}$ M solution of the HE probe in dehydrated toluene. The photodegradation condition was initiated under continuous illumination from a LED lamp with dry oxygen flow. Figure 4e shows the normalized increment in emission ($[I_F(t)/[I_F(t_0)]$ at 610 nm vs ageing time) to represent the superoxide generation rate (The original PL data are displayed in Figure S8, Supporting Information). It can be found that the superoxide yield is significantly increased in the UVCA without paraffin-encapsulated devices when compared with the fresh film. Meanwhile, superoxide yield of the UVCA with paraffin-encapsulated devices also presents a slightly increase, but

much lower than that without paraffin-encapsulated devices. From this result, the vacancy generation is efficiently inhibited by the UVCA with paraffin encapsulation, which could further be beneficial to the operational stability of PSCs devices.

In addition, the defects were also investigated by studying the energy loss in each device. The light-intensity-dependent $V_{oc}$ can provide critical insights into the mechanism of recombination processes in the PV device.[16] At $V_{oc}$, no net flow of current ($J = 0$ mA cm$^{-2}$) pass through the device, thus all the photogenerated charge carriers should recombine in the PVSK film. The corresponding charge carrier recombination process is reflected by the ideality factor $n$ determined by the slope of the $V_{oc}$ versus incident light intensity as shown in Equation (1)

$$n = \frac{q}{kT} \frac{d\,V_{oc}}{d\ln(\Phi)} \qquad (1)$$

where $q$ is the elementary charge, $k$ is the Boltzmann constant, $T$ is the temperature, and $\Phi$ is the light intensity.[17] When the ideality factor $n$ approaches 2, Shockley–Read–Hall (SRH) type, trap-assisted recombination dominates. In contrast, in the case of recombination of free electrons and holes, the ideality factor should be 1.

The light-intensity-dependent $V_{oc}$ was measured under different incident light intensity ranging from 2.6 to 100 mW cm$^{-2}$ (from 0.26 to 1 sun) and corresponding parameters are plotted in Figure 4f. The ideality factor $n$ calculated from the slope of the fitting curves are 1.54, 1.58, and 1.84 for the fresh device, UVCA with/without paraffin-encapsulated device, respectively, and the encapsulated devices were aged under illumination for 6 h before test. From the changes of ideality factors, we can conclude that the trap-assisted recombination in the aged

UVCA with paraffin-encapsulated device is close to the fresh device, which is attributed to the inhibited generation of defects from UVCA with paraffin encapsulation. However, the UVCA without paraffin-encapsulated device shows significant change from 1.54 to 1.84, indicating a higher trap-assisted recombination rate.

The above results reveal that in addition to the inhibition of phase segregation and degradation, the UVCA with paraffin encapsulation also shows superior advantages on suppressing the generation of defects. The nonpolar nature enables the paraffin to remove the residue oxygen and moisture entirely, resulting in the excellent materials stability.

### 2.4. 1000 h Operational Lifetime of Paraffin-Encapsulated PSCs

From previous results, it can be found that UVCA with paraffin encapsulation can effectively inhibit the phase segregation and suppresses the defects generation. The device encapsulated with paraffin also shows negligible change in color after aging under AM 1.5 for 40 d as shown in Figure S9 (Supporting Information). Therefore, the device performance and stability tests were performed to evaluate the reliability of UVCA with paraffin encapsulation.

The device constructed with structure ITO/SnO$_2$/perovskite/ Spiro-OMeTAD/Au was used for demonstration, as shown in Figure S2 (Supporting Information), with details described in the Experimental Section. **Figure 5**a shows the $J$–$V$ curves of devices before and after encapsulation by UVCA with/without paraffin, the efficiency of the device is centered at 20.80% with no significantly changed device parameters before and after the encapsulation as shown in **Table 1**, and the efficiency
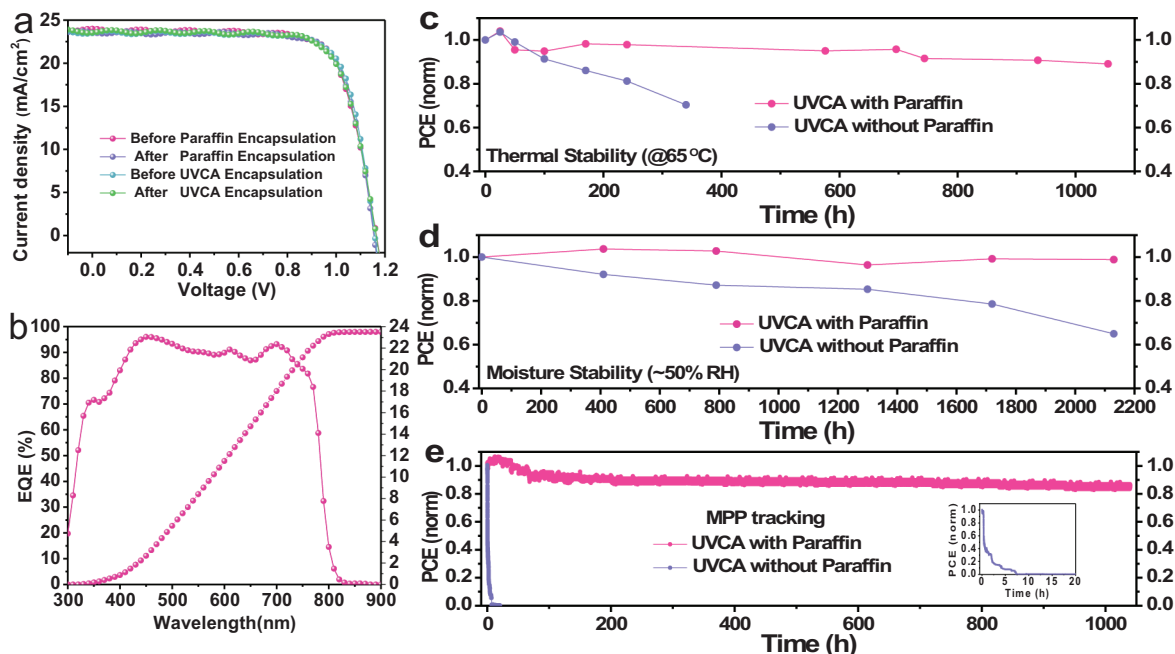


**Figure 5.** a) The $J$–$V$ curves of devices before and after encapsulation. b) External quantum efficiency and corresponding integrated photocurrent of UVCA with paraffin-encapsulated PSCs device. c) Thermal stability and d) moisture stability track of encapsulated devices. e) Continuous MPP track under ambient environment with different encapsulation conditions. Inset: the MPP track of UVCA without paraffin encapsulation with short time range.

**Table 1.** The device performance parameters.

| Encapsulant UVCA | | PCE [%] | $V_{oc}$ [V] | $J_{sc}$ [mA cm$^{-2}$] | FF [%] |
|---|---|---|---|---|---|
| With paraffin | Before | 20.85 | 1.16 | 24.00 | 75.89 |
| | After | 20.84 | 1.16 | 23.56 | 76.25 |
| Without paraffin | Before | 20.80 | 1.15 | 23.48 | 77.03 |
| | After | 20.54 | 1.16 | 23.55 | 75.19 |

distribution of devices before and after encapsulation by each method are given in Figures S10 and S11 (Supporting Information). Figure 5b shows the external quantum efficiency (EQE) spectra of the UVCA with paraffin-encapsulated device, displaying an onset around 800 nm. And the integrated $J_{sc}$ from the EQE spectra agrees well with the $J$–$V$ measurement result.

The thermal stability and moisture stability of the UVCA with/without paraffin-encapsulated devices are tracked by tested periodically, as shown in Figure 5c,d. It clearly can be seen that the device encapsulated by UVCA with paraffin shows superior thermal stability, which retain ≈90% of its initial efficiency after annealed under 65 °C in the ambient environment with 40–60% RH for over 1000 h. At the same time, the efficiency of the UVCA without paraffin-encapsulated device dropped rapidly. Several previous works showed that small molecule Spiro-OMeTAD with a low intrinsic glass transition temperature would crystallize under thermal stress.[18] The hole transport layer (Spiro-OMeTAD) has been modified by conductive polymer poly(triarylamine), which is effective to improve the thermal stability of the device. Besides, the improved thermal stability of the device encapsulated by UVCA with paraffin compared to that of UVCA without paraffin is possibly due to the removal of residual oxygen and moisture during encapsulation process. Literatures have shown that oxygen and moisture trigger phase segregation and decomposition of absorber layer.[8] Meanwhile, the Spiro-OMeTAD is degraded faster with the assistance of moisture.[19] In addition, the thermal stability tracked at 85 °C is shown in Figure S12 (Supporting Information), and the UVCA with paraffin encapsulated device also present much better stability than that without paraffin-encapsulated devices. In addition, the UVCA with paraffin-encapsulated device also shows great ability for preventing the moisture invasion. After stored in the ambient environment with 50% RH, the UVCA with paraffin-encapsulated device shows negligible efficiency degradation. However, at the same time slot, the UVCA without paraffin-encapsulated device lost over 40% of its initial PCE. The detail parameters are summarized in Figures S13 and S14 (Supporting Information). To further verify the reliability of the encapsulation under high temperature and high humidity, the moisture-sensitive FACs perovskite devices were applied to the damp heat test of the encapsulated device at 85 °C with relative humidity around 60–90% as shown in Figure S15 (Supporting Information). We also collected the temperature cycling test results, which are presented in Figure S16 (Supporting Information). The above results indicate that our new developed solvent-free encapsulation strategy significantly improves the thermal and moisture stability of the encapsulated devices.

MPP measurement is now considered as the most valuable and convincible test protocol for evaluating the stability of PSCs. The MPP tracks of devices encapsulated by UVCA with paraffin/without paraffin were recorded as shown in Figure 5e. The MPP measurement was conducted under the ambient environment with relative humidity around 30–50%. It can be seen that the UVCA without paraffin-encapsulated device experiences a dramatic efficiency decay, and the device efficiency decayed to almost zero within 10 h due to the existence of oxygen and moisture in the headspace above the device. In contrast, the UVCA with paraffin-encapsulated device shows excellent stability. Even after 1000 h of MPP measurement, the device still retains over 80% of its initial PCE. Figure S17 and Table S2 (Supporting Information) summarize the lifetime of PSCs achieved from previous reports and this work. This work demonstrates that the PSCs by using the ambient encapsulation can also survive from the MPP tracking under ambient environment for over 1000 h. To our knowledge, this is also one of the few works that accomplished the encapsulation process under ambient environment.[20] Therefore, we believe that this low-cost and straightforward encapsulation method will shorten the gap between the fundamental research and commercialization of PSCs.

## 3. Conclusions

In conclusion, we developed a low-temperature (below 100 °C) encapsulation technique compatible to perovskite solar cells by using nonpolar low-cost paraffins as the encapsulant. The paraffin with low melting point was found to be capable of removing the residual oxygen and moisture during the encapsulation processing, and to retard the escape of volatile species upon perovskite decomposition. With this encapsulation, the perovskite absorber layer suffered from much less phase segregation and vacancy defect generation, which inhibited the film decomposition consequently, and dramatically enhanced the devices' thermal and moisture stability. Ultimately, the resultant device achieves superior long-term stability, whereby the efficiency retained 80% of initial value under MPP tracking for over 1000 h. More importantly, this solvent-free encapsulation method based on paraffin can be operated under ambient environment, which is easier to be adopted by mass production. It thus provides new insight for the further development of encapsulation technology for commercialized utilization of perovskite optoelectronics.

## Supporting Information

Supporting Information is available from the Wiley Online Library or from the author.

## Acknowledgements

## Conflict of Interest

The authors declare no conflict of interest.

## Keywords

[1] a) A. Kojima, K. Teshima, Y. Shirai, T. Miyasaka, *J. Am. Chem. Soc.* 2009, *131*, 6050; b) N. Pellet, P. Gao, G. Gregori, T.-Y. Yang, M. K. Nazeeruddin, J. Maier, M. Grätzel, *Angew. Chem.* 2014, *126*, 3215; *Angew. Chem., Int. Ed.* 2014, *53*, 3151; c) J.-H. Im, I.-H. Jang, N. Pellet, M. Grätzel, N.-G. Park, *Nat. Nanotechnol.* 2014, *9*, 927; d) M. R. Filip, G. E. Eperon, H. J. Snaith, F. Giustino, *Nat. Commun.* 2014, *5*, 5757; e) S. D. Stranks, G. E. Eperon, G. Grancini, C. Menelaou, M. J. Alcocer, T. Leijtens, L. M. Herz, A. Petrozza, H. J. Snaith, *Science* 2013, *342*, 341; f) C. S. Ponseca, T. J. Savenije, M. Abdellah, K. Zheng, A. Yartsev, T. Pascher, T. Harlang, P. Chabera, T. Pullerits, A. Stepanov, J.-P. Wolf, V. Sundström, *J. Am. Chem. Soc.* 2014, *136*, 5189.

[2] a) H. Zhou, Q. Chen, G. Li, S. Luo, T. b. Song, H. S. Duan, Z. Hong, J. You, Y. Liu, Y. Yang, *Science* 2014, *345*, 542; b) H. Tan, A. Jain, O. Voznyy, X. Lan, F. P. García de Arquer, J. Z. Fan, R. Quintero-Bermudez, M. Yuan, B. Zhang, Y. Zhao, F. Fan, P. Li, L. N. Quan, Y. Zhao, Z.-H. Lu, Z. Yang, S. Hoogland, E. H. Sargent, *Science* 2017, *355*, 722.

[3] a) Q. Chen, H. Zhou, Z. Hong, S. Luo, H.-S. Duan, H.-H. Wang, Y. Liu, G. Li, Y. Yang, *J. Am. Chem. Soc.* 2014, *136*, 622; b) S. Ye, H. Rao, W. Yan, Y. Li, W. Sun, H. Peng, Z. Liu, Z. Bian, Y. Li, C. Huang, *Adv. Mater.* 2016, *28*, 9648; c) N.-G. Park, *J. Phys. Chem. Lett.* 2013, *4*, 2423.

[4] a) C. C. Boyd, R. Cheacharoen, T. Leijtens, M. D. McGehee, *Chem. Rev.* 2019, *119*, 3418; b) T. A. Berhe, W.-N. Su, C.-H. Chen, C.-J. Pan, J.-H. Cheng, H.-M. Chen, M.-C. Tsai, L.-Y. Chen, A. A. Dubale, B.-J. Hwang, *Energy Environ. Sci.* 2015, *9*, 323; c) N. H. Tiep, Z. Ku, H. J. Fan, *Adv. Energy Mater.* 2016, *6*, 1501420.

[5] a) N. J. Jeon, H. Na, E. H. Jung, T.-Y. Yang, Y. G. Lee, G. Kim, H.-W. Shin, S. I. Seok, J. Lee, J. Seo, *Nat. Energy* 2018, *3*, 682; b) Z. Li, Y. Zhao, X. Wang, Y. Sun, Z. Zhao, Y. Li, H. Zhou, Q. Chen, *Joule* 2018, *2*, 1; c) G. Grancini, C. Roldan-Carmona, I. Zimmermann, E. Mosconi, X. Lee, D. Martineau, S. Narbey, F. Oswald, F. De Angelis, M. Graetzel, M. K. Nazeeruddin, *Nat. Commun.* 2017, *8*, 15684.

[6] a) M. I. Saidaminov, J. Kim, A. Jain, R. Quintero-Bermudez, H. Tan, G. Long, F. Tan, A. Johnston, Y. Zhao, O. Voznyy, E. H. Sargent, *Nat. Energy* 2018, *3*, 648; b) L. Liu, S. Huang, Y. Lu, P. Liu, Y. Zhao, C. Shi, S. Zhang, J. Wu, H. Zhong, M. Sui, H. Zhou, H. Jin, Y. Li, Q. Chen, *Adv. Mater.* 2018, *30*, 1800544; c) T. Liu, Y. Zhou, Z. Li, L. Zhang, M.-G. Ju, D. Luo, Y. Yang, M. Yang, D. H. Kim, W. Yang, N. P. Padture, M. C. Beard, X. C. Zeng, K. Zhu, Q. Gong, R. Zhu, *Adv. Energy Mater.* 2018, *8*, 1800232; d) J. A. Christians, P. Schulz, J. S. Tinkham, T. H. Schloemer, S. P. Harvey, B. J. Tremolet de Villers, A. Sellinger, J. J. Berry, J. M. Luther, *Nat. Energy* 2018, *3*, 68; e) H. Zhang, X. Ren, X. Chen, J. Mao, J. Cheng, Y. Zhao, Y. Liu, J. Milic, W. Yin, M. Grätzel, W. C. H. Choy, *Energy Environ. Sci.* 2018, *11*, 2253; f) B. Yang, D. Ouyang, Z. Huang, X. Ren, H. Zhang, W. C. H. Choy, *Adv. Funct. Mater.* 2019, *29*, 1902600; g) Y. Zhao, H. Zhang, X. Ren, H. L. Zhu, Z. Huang, F. Ye, D. Ouyang, K. W. Cheah, A. K.-Y. Jen, W. C. H. Choy, *ACS Energy Lett.* 2018, *3*, 2891.

[7] a) K. Domanski, E. A. Alharbi, A. Hagfeldt, M. Grätzel, W. Tress, *Nat. Energy* 2018, *3*, 61; b) A. R. Bowring, L. Bertoluzzi, B. C. O'Regan, M. D. McGehee, *Adv. Energy Mater.* 2018, *8*, 1702365.

[8] a) J. Huang, S. Tan, P. D. Lund, H. Zhou, *Energy Environ. Sci.* 2017, *10*, 2284; b) N. Aristidou, C. Eames, I. Sanchez-Molina, X. Bu, J. Kosco, M. S. Islam, S. A. Haque, *Nat. Commun.* 2017, *8*, 15218; c) S. Draguta, O. Sharia, S. J. Yoon, M. C. Brennan, Y. V. Morozov, J. S. Manser, P. V. Kamat, W. F. Schneider, M. Kuno, *Nat. Commun.* 2017, *8*, 200.

[9] a) M. Crespo-Quesada, L. M. Pazos-Outón, J. Warnan, M. F. Kuehnel, R. H. Friend, E. Reisner, *Nat. Commun.* 2016, *7*, 12555; b) R. Cheacharoen, N. Rolston, D. Harwood, K. A. Bush, R. H. Dauskardt, M. D. McGehee, *Energy Environ. Sci.* 2018, *11*, 144; c) L. Shi, T. L. Young, J. Kim, Y. Sheng, L. Wang, Y. Chen, Z. Feng, M. J. Keevers, X. Hao, P. J. Verlinden, M. A. Green, A. W. Y. Ho-Baillie, *ACS Appl. Mater. Interfaces* 2017, *9*, 25073; d) Q. Dong, F. Liu, M. K. Wong, H. W. Tam, A. B. Djurišić, A. Ng, C. Surya, W. K. Chan, A. M. C. Ng, *ChemSusChem* 2016, *9*, 2597; e) Y. Han, S. Meyer, Y. Dkhissi, K. Weber, J. M. Pringle, U. Bach, L. Spiccia, Y.-B. Cheng, *J. Mater. Chem. A* 2015, *3*, 8139.

[10] M. Saliba, T. Matsui, K. Domanski, J.-Y. Seo, A. Ummadisingu, S. M. Zakeeruddin, J.-P. Correa-Baena, W. R. Tress, A. Abate, A. Hagfeldt, M. Grätzel, *Science* 2016, *354*, 206.

[11] Y. Hu, M. F. Aygüler, M. L. Petrus, T. Bein, P. Docampo, *ACS Energy Lett.* 2017, *2*, 2212.

[12] Y. C. Kim, N. J. Jeon, J. H. Noh, W. S. Yang, J. Seo, J. S. Yun, A. Ho-Baillie, S. Huang, M. A. Green, J. Seidel, T. K. Ahn, S. I. Seok, *Adv. Energy Mater.* 2016, *6*, 1502104.

[13] R. A. Venditti, K. L. Spence, O. J. Rojas, J. J. Pawlak, M. A. Hubbe, *BioResources* 2011, *6*, 4370.

[14] A. Walsh, D. O. Scanlon, S. Chen, X. G. Gong, S.-H. Wei, *Angew. Chem.* 2014, *127*, 1811; *Angew. Chem., Int. Ed.* 2014, *54*, 1791.

[15] N. Aristidou, I. Sanchez-Molina, T. Chotchuangchutchaval, M. Brown, L. Martinez, T. Rath, S. A. Haque, *Angew. Chem.* 2015, *127*, 8326; *Angew. Chem., Int. Ed.* 2015, *54*, 8208.

[16] J.-W. Xiao, S. Ma, S. Yu, C. Zhou, P. Liu, Y. Chen, H. Zhou, Y. Li, Q. Chen, *Nano Energy* 2018, *46*, 45.

[17] T. Kirchartz, F. Deledalle, P. S. Tuladhar, J. R. Durrant, J. Nelson, *J. Phys. Chem. Lett.* 2013, *4*, 2371.

[18] M. Ren, J. Wang, X. Xie, J. Zhang, P. Wang, *ACS Energy Lett.* 2019, *4*, 2683.

[19] S. Wang, Z. Huang, X. Wang, Y. Li, M. Günther, S. Valenzuela, P. Parikh, A. Cabreros, W. Xiong, Y. Meng, *J. Am. Chem. Soc.* 2018, *140*, 16720.

[20] T.-Y. Yang, N. JoongJeon, H.-W. Shin, S. S. Shin, Y. Y. Kim, J. Seo, *Adv. Sci.* 2019, *6*, 1900528.

# Cation Diffusion Guides Hybrid Halide Perovskite Crystallization during the Gel Stage

*Lang Liu[+], Yang Bai[+], Xiao Zhang, Yuequn Shang, Chenyue Wang, Hao Wang, Cheng Zhu, Chen Hu, Jiafeng Wu, Huanping Zhou, Yujing Li, Shihe Yang, Zhijun Ning, and Qi Chen\**

***Abstract:*** *Lead halide perovskites with mixed cations/anions often suffer from phase segregation, which is detrimental to device efficiency and their long-term stability. During perovskite film growth, the gel stage (in between liquid and crystalline) correlates to phase segregation, which has been rarely explored. Herein, cation diffusion kinetics are systematically investigated at the gel stage to develop a diffusion model obeying Fick's second law. Taking 2D layered perovskite as an example, theoretical and experimental results reveal the impact of diffusion coefficient, temperature, and gel duration on the film growth and phase formation. A homogenous 2D perovskite thin film was then fabricated without significant phase segregation. This in-depth understanding of gel stage and relevant cation diffusion kinetics would further guide the design and processing of halide perovskites with mixed composition to meet requirements for optoelectronic applications.*

## Introduction

Owing to their outstanding optoelectronic performance, organic–inorganic halide perovskite materials have attracted great attention.[1] These materials adopt a formula of $ABX_3$, where A is monovalent organic or inorganic cation, B is a metal cation ($Pb^{2+}$, $Sn^{2+}$, $Ge^{2+}$), and X is a halide anion ($Cl^-$, $Br^-$, $I^-$). This family of materials have an enormous compositional space, wherein components in A, B, X sites can be substituted at various stoichiometry to a large extent. Therefore, the optoelectronic properties of the resultant materials are highly tunable. By choosing suitable mixed components, the power conversion efficiency and long-term stability of the resultant photovoltaic cells improved significantly.[2]

However, recent reports indicate that the halide perovskite with mixed composition (mostly at A/X sites) suffer

from phase segregation.[3] Take the mixed-halide perovskite as an example, it was found that the $MAPb(Br_xI_{1-x})_3$ tended to segregate into iodide and bromide-rich phases under illumination.[3b] Zhang and co-workers suggested that the all inorganic perovskite ($CsPbBr_{1.2}I_{1.8}$) nanocrystals also underwent segregation at electrical bias as evidenced by the blue-shifted photoluminescence peak.[4] Even for the widely employed composition of $(FAPbI_3)_{0.85}(MAPbBr_3)_{0.15}$, the thin film was not homogeneous, but intrinsically segregating into iodide-rich nanodomains.[3d] Beyond the halide segregation, recent results suggested it was neither uniform for the spatial distribution of cations in mixed-cation perovskite.[3f,5] Take the mixed cesium–rubidium lead iodide perovskites for example, it is found that the introduced rubidium is segregated into $RbPbI_3$ phases with the aid of solid-state nuclear magnetic resonance.[5b] Moreover, the 2D Ruddlesden–Popper (RP) layered perovskites (with general formula of $A_2MA_{n-1}Pb_nX_{3n+1}$) suffer from severe phase segregation, which is even more prominent than that of the 3D perovskite counterpart. For example, $BA_2MA_3Pb_4I_{13}$ thin films exhibited asymmetrical photoluminescence (PL) emission, wherein the $n \approx \infty$ phases were mainly located on the upper surface, and small n value ($n = 1$, 2, 3 and 4) phase were likely concentrated on the bottom.[6]

The inherent phase segregation occurs during the film formation process, which involves the gel stage when liquid films are transformed to crystalline ones (Scheme 1). Recent in situ grazing incidence wide-angle X-ray scattering (GIWAXS) results clearly suggested the existence of this gel stage, during which perovskite precursor in the liquid film grows into the polycrystalline film. It is claimed the formation of gel stage is associated to the interaction between precursor and solvents.[7] Further studies indicated this gel stage had a profound influence on the following crystal growth, wherein

[*] L. Liu,[+] Dr. Y. Bai,[+] X. Zhang, C. Wang, H. Wang, C. Zhu, J. Wu,
Prof. Y. Li, Prof. Q. Chen
Beijing Key Laboratory of Construction Tailorable Advanced Functional Materials and Green Applications, Experimental Center of Advanced Materials, School of Materials Science & Engineering, Beijing Institute of Technology, 100081 Beijing (China)
E-mail: qic@bit.edu.cn

Y. Shang, Prof. Z. Ning
School of Physical Science and Technology, ShanghaiTech University
Shanghai 201210 (China)

C. Hu, Prof. S. Yang
Department of Chemistry
The Hong Kong University of Science and Technology
Clear Water Bay, Kowloon, Hong Kong (China)

Prof. H. Zhou
Department of Materials Science and Engineering
College of Engineering, Peking University
100871 Beijing (China)

Prof. S. Yang
Guangdong Provincial Key Lab of Nano-Micro Materials Research,
School of Chemical Biology and Biotechnology, Peking University
Shenzhen Graduate School
Shenzhen 518055 (China)

[+] These authors contributed equally to this work.

Supporting information (including PL spectra, diffusion model, UV/Vis absorption, GIWAXS, and XRD pattern) and the ORCID identification number(s) for the author(s) of this article can be found under: https://doi.org/10.1002/anie.201914183.
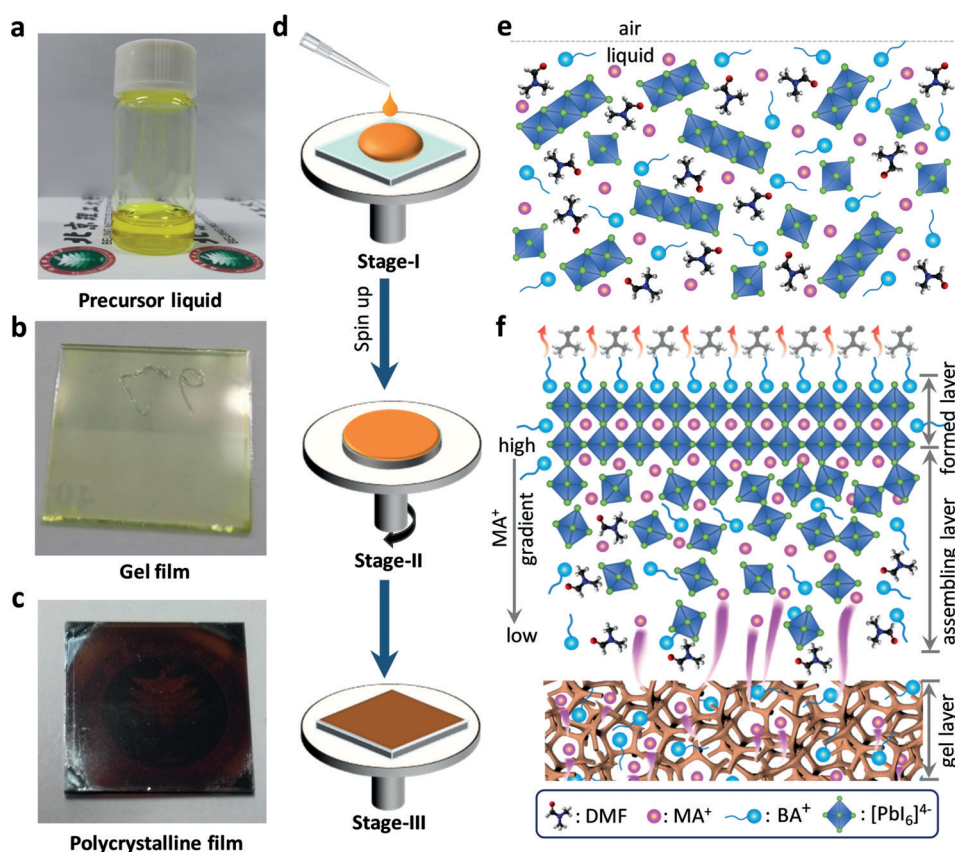
**Scheme 1.** Photographs and representations of different film formation stages. a) Precursor liquid stage. b) Gel stage. This photograph shows the gel film is light yellow without fluidity. c) Polycrystalline film stage. For this stage, the film converted into perovskite completely and turned dark brown. d)–f) Diagrams of the d) film formation process, e) the precursor liquid, and f) gel converted into perovskite phase.

the intermediate phases provide a scaffold to initiate the subsequent crystal growth.[8] It is reported the gel state affects the growth rate of crystal and the assembly behavior between the inorganic framework and the cations intercalated, which leads to desirable perovskite phases and consequent film texture and microstructure.[8a] Furthermore, it is found that by suitable processing (for example, hot casting), the gel life span can be modulated to affect the final film quality in the context of morphology and crystal orientation.[7b, 8a]

These excellent pioneer works highlight a gleaming but indispensable stage that is crucial to the film formation and the performance of the optoelectronic devices (both efficiency and stability). Owing to the short duration of this stage (which lasts only several seconds/minutes) however, it receives quite limited efforts to understand the gel stage. To date, it lacks a theoretic model that reveals the gel dynamics with respect to different components in the mixed hybrid perovskite during the thin film growth. Therefore, it is particularly interesting to examine the gel formation for the state-of-art perovskite formula with contains different components, which are expected to behave distinguishably on the diffusion and crystallization behavior along the film growth. More importantly, it is urgently needed to establish a profound and general understanding on the gel state by emphasizing it over the entire film growth, which will guide future materials design and film processing of different types of hybrid perovskites.

Herein for the first time, we carefully investigate the cation diffusion process at gel stage before perovskite crystallization by adopting the diffusion model responsible for the phase segregation. In light of the diffusion model, we reveal several parameters that affect the diffusion and subsequent phase segregation, which correlate to the corresponding compositional evolution experimentally. The local phase distribution of perovskite thin films, irrespective of 2D or 3D composition, is highly dependent on the gel stage kinetically governed by diffusion. Based on the understanding, we successfully explained the phase segregation prevailing in layered 2D perovskites thin film, and further fabricated homogenous films without significant phase segregation.

## Results and Discussion

### Gel and Phase Segregation in Layered 2D Perovskite Film

Phase segregation along the film thickness direction is often observed in layered 2D perovskite films,[6b, 9] yet its origin is not fully illustrated. Here we checked the photoluminescence (PL) spectra of the 2D perovskite film deposited by the hot-casting method with a nominal precursor stoichiometry of $BA_2MA_3Pb_4I_{13}$ (see the Supporting Information for details).[10] As shown in Figure 1 a, the PL signals illuminated from the front side (perovskite film side) and the
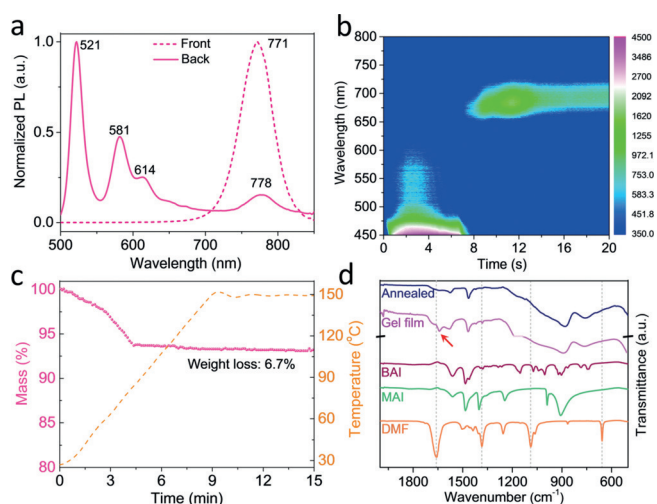
***Figure 1.*** a) PL spectra of typical as-prepared 2D perovskite film prepared at 110°C. b) In situ PL spectra of the film during spin-coating process. c) TGA curve of the as-cast gel film. d) FTIR spectra of the precursors, the as-cast gel film and the annealed film.

back side (ITO side) showed significant difference. The PL spectra from front presented a dominant emission peak at 771 nm, which probably stemmed from components of large *n* value perovskites. The spectra from back exhibited several short-wavelength signals of 521 nm, 581 nm, and 614 nm, in accordance to the emission peaks of 2D perovskites with $n = 1$, 2, and 3, respectively.[6b,9] Combining the XRD pattern (Supporting Information, Figure S1a) and optical absorbance spectra (Supporting Information, Figure S1b), it clearly shows the phase segregation in the layered 2D perovskite films, in line with previous studies.[6,9b,10,11]

Different from other phase segregation developed during film aging in conventional 3D perovskites,[3,4] the above-mentioned phase segregation was observed in the pristine film, indicating the segregation is inherently related to the film formation process. As such, we investigated the PL spectra evolution at the top surface where the nucleation and crystallization process initiated during film growth.[12] First, we conducted in situ PL measurement with the excitation wavelength of 390 nm to explore the compositional evolution of corresponding perovskite film. Given the low transmittance (Supporting Information, Figure S2), this measurement mainly reveals the information at the surface along the direction of incident beam.[13] Figure 1b recorded the PL evolution of the film at room temperature starting from the spinning point. We observed a wide emission band centered at around 687 nm emerging at around 8 s, which was mainly ascribed to the formation of 2D perovskite with $n = 6$.[8d] Additionally, a strong band from 450 to 600 nm was also observed at earlier stage (0–8 s). It is assigned to the emission of the gel film (Supporting Information, Figure S3).

We further probed the composition of the entire gel film by thermogravimetric analysis (TGA) measurement (Figure 1c). The as-casted film experienced a weight loss of 6.7% when gradually heated to 110°C. It confirms there are substantial amount of residual solvents in the solidified film before subsequent growth of the polycrystalline film. The

residual solvents were further found to interact with the solutes to form the gel, which is shown in the Fourier-transform infrared spectroscopy (FTIR) of the gel film (Figure 1d). As compared to the pure solvents, the stretching vibration of C=O from DMF molecule shifted to 1640 cm$^{-1}$ from 1660 cm$^{-1}$ (Figure 1d). This wavenumber shift is attributed to the formation of a solvent–solute complex.[7a] After further annealing, this specific vibration absorption peak disappeared due to the removal of the solvent. It thus clearly indicates the distinctive gel stage, which involves the residual solvent interacting with the solutes.

Accordingly, we identify three stages during the film growth of hybrid halide perovskite including, Stage I solution, Stage II gel, and Stage III crystallization, which are illustrated in Scheme 1. Stage I involves the precursor solution and the formation of liquid films, which contains solute colloids with different sizes ranging from several nanometers to several hundred nanometers. The dynamic light scattering measurement shows the colloid size distribution (Scheme 1; Supporting Information, Figure S4), which is in line with previous reports.[14] During spin-coating process, the gel emerges (Stage II) wherein the a portion of solvents volatilizes and the entire system gradually solidifies. The as-formed gel is mainly composed of negatively charged lead halide colloids ($[PbI_6]^{4-}$) and free organic cations, which are interacted with residual solvents via coordination effects.[15] Further removal of solvent by annealing and/or spinning lead to the nucleation of perovskite that initiates the crystallization (Stage III).

Tremendous efforts have been focused on Stage III to describe the kinetics of this crystallization process. It is generally accepted that the nuclei mainly compose of $[PbI_6]^{4-}$ intermediate colloids with smaller n value species ($n < 4$),[15] which further serve as the template to guide assembly of inorganic framework and cation intercalation simultaneously.[7b,8d,16] Unfortunately, the existing models often treat different cations indistinguishably, which may not be feasible in the layered 2D perovskites that features over two types of distinguished cations. Therefore, there remains the question in the mixed cation systems that should be further considered in the context of diffusion, which correlates to the Stage II that is largely neglected.

## The Cation Diffusion Model During the Gel Stage

For any chemical reactions, including cation intercalation during crystal growth, it is the local chemical potential that determines the reaction kinetics/thermodynamics, wherein the reactant concentration plays an important role. Given the even concentration distribution of each component in a precursor colloidal at Stage I, it is out of our expectation to observe compositional segregation at final Stage III. It is thus of great interest to probe the diffusion features of different cations in Stage II, which probably determines the local chemical concentration at the subsequent Stage III.

The cation diffusion characteristics generally obeys the Fick's Second Law following the non-steady state diffusion pattern, since the local concentration of solutes changes with time. For simplicity, we adopt one dimensional model to
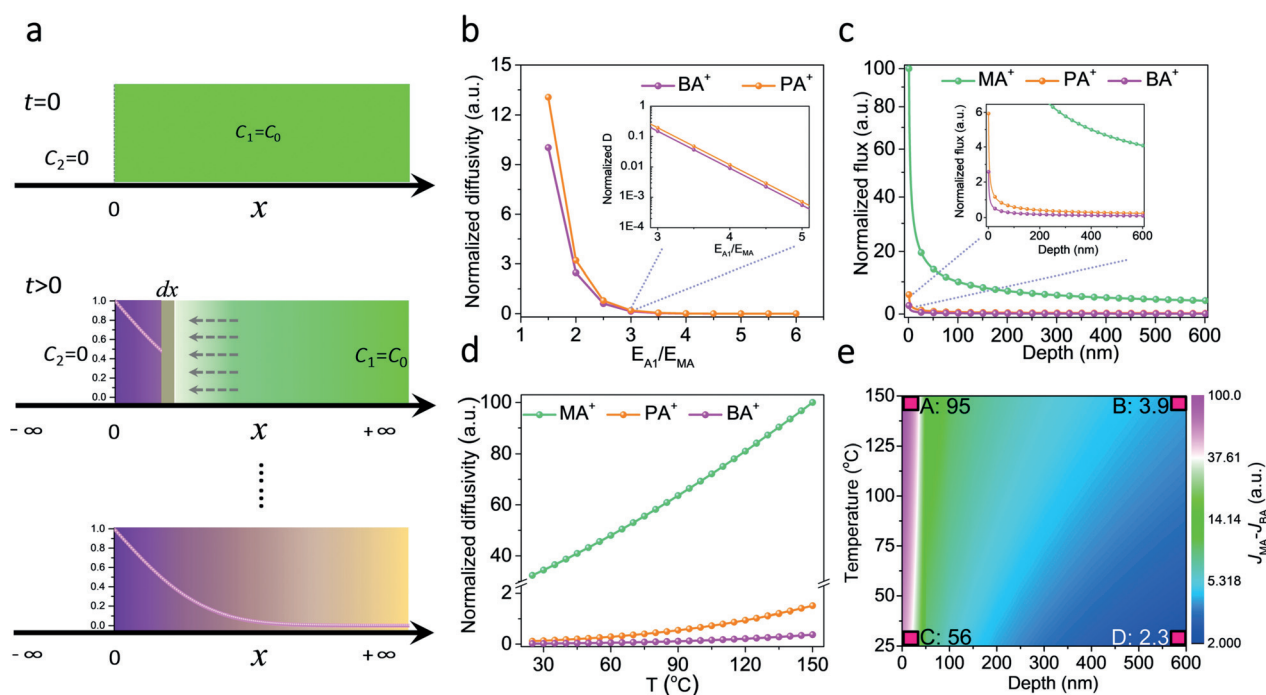
**Figure 2.** Diffusion model and causes of diffusion difference. a) Diagram of the diffusion model. b) The diffusivity of cation under varied $E_{A1}/E_{MA}$ ratio at 70°C. c) The diffusivity of MA$^+$ and BA$^+$ (when $E_{BA}=2E_{MA}$) under varied temperatures. d) Cations fluxes at different depths under 70°C. e) Flux gap ($J_{MA}-J_{BA}$) mapping at different temperatures.

check the local concentration evolution of each cation (MA/BA) along the film thickness direction (Figure 2a), which follows the equation:[17]

$$\frac{\partial C}{\partial t} = D \frac{\partial^2 C}{\partial x^2} \qquad (1)$$

where $C$ is the concentration of diffusing species, which is related to local time $t$ and the position $x$ (here is the film depth). $D$ is diffusion coefficient, namely, diffusivity, which is highly dependent on cations, as is discussed later.

Assuming all diffused cations are intercalated into the crystal structure, their diffusive flux $J$ should correlate to the local concentration of a given cation in the polycrystalline film. Assuming $J$ with respect to different cations are independent, the stoichiometry in the local crystal is reflected by $J$ to reveal the phase segregation in the film. To obtain diffusive flux $J$, we solve Equation (1) with certain boundary conditions (see details in supporting information). Finally, we have:

$$J = -\frac{C_0}{2}\sqrt{\frac{Dr}{\pi x}}\exp\left(-\frac{rx}{4D}\right) \qquad (2)$$

where $C_0$ is the initial concentration for a given cation, and $r$ is crystallization rate, which is constant given the fast intercalation reaction and high completeness of this reaction.

To be noted, the diffusive flux $J$ is the function of $x$ (film thickness) and $D$ (the diffusivity of cations), which is further estimated according to the Eyring's theory:[18]

$$D = \frac{\lambda^2}{v_f^{1/3}}\left(\frac{kT}{2\pi m}\right)^{1/2}\exp\left(-\frac{E}{RT}\right) \qquad (3)$$

where $\lambda$ is the distance between cations at equilibrium positions, $k$ is the Boltzmann constant, $T$ is the temperature in Kelvin, $v_f$ is the molecular volume, $m$ is mass of the molecule, $R$ is the gas constant, and $E$ is the diffusion activation energy.

As shown, the diffusion process is governed by two categories of factors, the intrinsic factors corresponding to the characteristic of cations, such as $m$, $E$, $\lambda$, and $v_f$, and the extrinsic factor of $T$. In a cation mixed perovskite system, the phase segregation is related to the local stoichiometry, which is determined by local flux ratio of each type of cation. According to the above diffusion model, we further conducted numerical simulation to examine several parameters which substantially impact the local flux, namely the characteristic of cations and the temperature.

We first examine the intrinsic factors, such as $m$, $E$, $\lambda$, and $v_f$, which are constant for a cation under a given processing condition. In our analysis when comparing alkyl ammonium cations such as BA$^+$, n-propylammonium (PA$^+$), and MA$^+$, we find with the increase of cation size, $m$ and $v_f$ increases (Supporting Information, Figure S6) to result in smaller diffusivity $D$ (Figure 2b). It is in accordance with general believe that larger cations diffuse slowly as compared to smaller ones. Moreover, the molecular distance $\lambda$ mainly depends on the local concentration of cations, indicative of the extent of the cation–cation interaction. Here, we reasonably assume the similar interaction to fix this parameter of $\lambda$ for further analysis (see the Supporting Information).

The activation energy $E$ in the exponential term suggests its significant influence on cation diffusion process, which reflects the cation–solvent interaction mainly governs by functional groups that the cation bears.[19] It is generally known, the stronger interaction, the larger value of $E$. It is thus suggested that $MA^+$ features the smallest $E$ among the three cations. Owing to the lack of experimental data, it is difficult to obtain exact $E$ value with respect to $MA^+$, $PA^+$, or $BA^+$. However, we can semi-quantitatively illustrate the relationship between D and E by assuming a different $E$ ratio relative to that of $MA^+$. As shown in Figure 2 b, the diffusivity dropped significantly to 2.5% (note the diffusivity value of $MA^+$ is 100%) when $E_{BA}/E_{MA}$ ratio increased to 2. This downtrend was also observed in that of the $PA^+$.

Based on the hypothetic diffusivity, we further predicted the diffusive fluxes at different depth of the film. As shown in Figure 2 c, both the fluxes of $MA^+$ and $BA^+$ decreased dramatically during the initial 0–50 nm from the surface, while the flux drop of $MA^+$ is greater than that of $BA^+$. And in the deeper region (50–600 nm), $MA^+$ flux decreased continuously, but in a mild manner. As a comparison, the flux for the $BA^+$ experienced only a small decrease across the same region of the film.

Furthermore, the extrinsic factor $T$ are found to affect the diffusivity substantially according to the diffusion model. As shown in Figure 2 d, the diffusivity of $MA^+$, $PA^+$, and $BA^+$ increased with the elevated temperature. Owing to its smallest $E$, the diffusivity of $MA^+$ shows the most significant increment by increasing the temperature. It indicates the diffusivity of cations show even greater difference at higher temperature, which suggests the temperature is one important parameter to differentiate the diffusivity of different cations.

Moreover, we use the model to predict the fluxes (normalized) difference between $BA^+$ and $MA^+$ at different depths with different temperature (Figure 2 e). This visualization further reveal several interesting points: 1) the flux difference shows most significant change at surface region (depth of 0–50 nm), wherein other part of the film experiences a much smaller flux difference (comparing A and B), 2) the surface region shows higher flux difference at higher temperature (comparing A and C), and 3) the evolution of flux difference along the film depth is more significant at higher temperature (comparing A,B and C,D). These observations are further verified with following experiments to correlate to the phase segregation in layered 2D perovskite films.

### Cations and Phase Segregation

According to the proposed diffusion model, the intrinsic characteristic of cations is one crucial factor responsible for the phase segregation. To prove the feasibility of the diffusion model, we employed a different cation, $PA^+$ with less bulky carbon chain compared to $BA^+$,[20] and investigated the cation distribution in the resultant thin films. We prepared films with the formula of $PA_2MA_3Pb_4I_{13}$ (tagged as PA, see the Supporting Information). The XRD pattern and UV/Vis spectra of PA are presented in the Supporting Information,

Figure S1, which also demonstrated the formation of multiple phases. When we checked the PL signal (Figure 3 b), the PL spectra from the front side of PA blue-shifted to 742 nm, indicating smaller $n$ value species compared to that of the BA sample (Figure 3 a). For the back-side illumination, it showed a dominant but broad peak at 645 nm mostly stemmed from the $n = 4$ phases. And this broad peak bridged the gap between low n value species and high $n$ value parts. It is in contrast to that of the BA with apparent emission from low n value components ($n = 1, 2, 3$), indicating greatly relieved phase segregation in the PA sample.
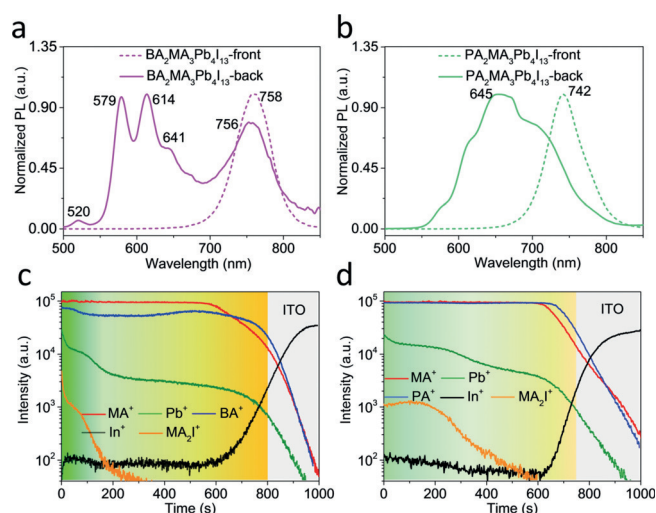


***Figure 3.*** Cations and segregation. PL spectrum and corresponding ToF-SIMS patterns of a),c) $BA_2MA_3Pb_4I_{13}$ and b),d) $PA_2MA_3Pb_4I_{13}$ film (prepared at 70°C).

To obtain more comprehensive spatial distribution information, we further resorted to the time of flight secondary ion mass spectrometry (TOF-SIMS), which was sensitive to traceable elements and organic fragments.[21] By etching the sample with a high-energy ion beam and analyzing the corresponding charged fragments, depth resolved elemental maps could be obtained. Figure 3 c displayed a depth profile of the as-prepared BA film. Since the intensity of $MA^+$ was too strong and beyond the upper detection limit, here we chose $MA_2I^+$ to analyze the distribution of $MA^+$. In the first 30 s etching, the relative intensity of $MA_2I^+$ decreased steeply, possibly indicating drastic decrease of $n$ value of the perovskite. In the depth of 30–80 s etching, the downward trend was much alleviated, which suggested the $n$ value change is less significant comparing to the first 30 s. Then another sudden drop (80–200 s) occurred and lastly its intensity decayed to the background level. The fragments of $Pb^+$ was also detected whose signal almost shared the same trend as that of the $MA_2I^+$, further reflected the variation tendency of different $n$-value perovskite species. However, for the $BA^+$ fragments, its intensity fluctuation was almost negligible except for the weak attenuation during 30–100 s, which is in line with our simulation results (Figure 2 c).

When $BA^+$ was replaced by $PA^+$ in the mixed perovskite thin film, the cation distribution showed quite different

behavior. As shown in Figure 3 d, the intensity of both $MA_2I^+$ and $Pb^+$ decayed much more slowly as compared to that in the BA sample (Figure 3 c). It indicates the compositional fluctuation (cations) in PA samples is less significant than that of in BA ones. Therefore, we suggest that the distribution of different perovskite species and the corresponding *n*-value along the film depth mainly depends on the diffusivity difference of cations. Especially, $MA^+/BA^+$ cation pairs show larger diffusivity difference (than $MA^+/PA^+$ cation pairs), which results in more predominant phase segregation.



**Figure 4.** Temperature and segregation. PL spectrum of $BA_2MA_3Pb_4I_{13}$ films prepared at a) 50°C, b) 90°C, and c) 130°C.

This finding not only stands in quasi-2D perovskite films, but also suits for the mixed 3D perovskites. We further investigated the popular hybrid perovskite with the nominal formula of $(FAPbI_3)_{0.85}(MAPbBr_3)_{0.15}$ as an example. We find the PL peak from the front side (772 nm) was not identical to that from the back side (784 nm; Supporting Information, Figure S7). Our recent ToF-SIMS profiles and cross-sectional TEM results confirmed the distribution of $MA^+$ decreased progressively from surface to bottom.[22] These results indicate that the phase segregation commonly occurs in halide perovskites with different A-site cations. It should be noted the segregation is caused by the diffusivity difference of different cations when this model is applied. It does not apply to the single cation perovskite system, wherein all cations follow the same diffusion pattern. Recent reports also confirmed the bearing groups with the cation has profound influence on the phase distribution.[23] In particular, the bulky alkyl group affects compatibility of cations to the inorganic $[PbI_6]^{4-}$ framework leading to the preferential formation of small-*n* value species.[23a] It further suggests that tuning the composition of A site could systematically manipulate the phase segregation in the resultant film.

### *Temperature and Phase Segregation*

The diffusion model also reveals the extrinsic factor, Temperature, plays an important role in phase segregation. The in situ PL results (Figure 1 b; Supporting Information, Figure S8) suggested the gel stage becomes shorter when temperature increases. To verify the argument, we studied the materials system based on quasi-2D layered perovskite films with fixed $BA^+/MA^+$ ratio as the A site cations. Films annealed at different temperatures were subjected to PL measurement (Figure 4). When illuminated from the front side, all samples possess the single emission peak attributed to high *n* value components close to 3D perovskite. With rising annealing temperature, the peak positions are red-shifted. Generally speaking, defects can induce PL peak red-shift. Combined with the PL and ToF-SIMS results (Figure 3 a,c), we believe the main reason for this red-shift was the composition change wherein n value become larger. How-
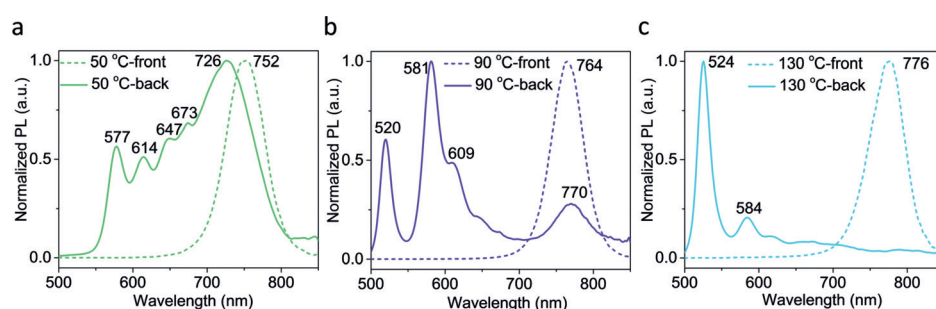
ever, defects may also take effects which cannot be fully excluded at the moment. It means that the concentration of $MA^+$ at the surface was higher than that annealed at lower temperature. It agrees well with the above diffusion model wherein the flux of $MA^+$ increase more than that of BA (Figure 2 e). As discussed previously, high temperature could enlarge the diffusivity difference between $MA^+$ and $BA^+$, resulting in significant increase of concentration ratio of $MA^+/BA^+$ at the surface.

Interestingly, PL spectra from the back side show distinctive features for samples obtained at different temperature. The compositional change with respect to *n* value, indicative of degree of phase segregation, become more obvious with increased temperature. At 50°C (Figure 4 a), the PL spectrum of back side showed a broad peak locating at 726 nm, along with the 2D phases with $n = 2$–5. When the temperature was raised to 90°C, the main peak blue-shifted to 581 nm corresponding to the $n = 2$ perovskite (Figure 4 b). The intensity of longer wavelength emission decreased substantially, suggesting much less components of high *n* value. Further increasing the temperature to 130°C, emission from the species with $n = 1$ appeared to be predominate (Figure 4 c). And it is absent of the emission signal from larger *n* phases, which suggests an extremely imbalanced distribution of $MA^+$ and $BA^+$ along the film depth direction.

The device performance at different temperatures was also investigated. The device prepared at 70°C shows the highest PCE (Supporting Information, Figure S9), which maintained almost 76% of its initial efficiency (12.35%) after 600 h of continuous MPP tracking at room temperature in nitrogen atmosphere. To be noted, the processing temperature affects not only segregation, but also crystal orientation (Supporting Information, Figure S10), which play a crucial role in determining device performance. In this case, it is not appropriate to give a conclusive remark on the relationship between phase segregation and device performance.

To be aware, the diffusion model successfully explains the vertical phase segregation in the perovskite film wherein components with high *n* values prefer to stay at the top surface. However, this model fails to explain the existence of a large number of low *n* value species at the bottom of the film. We note two major simplifications in the model that is likely to bring in the deviation from our experimental observations. Firstly, the one-dimensional diffusion model is based on the infinite depth of the film wherein cation supply is

continuous anywhere along the film. Actually, the cations reservoir is exhausted when close to the bottom of the film. This boundary condition is not included in our simulation to show the abrupt change of the perovskite crystals when diffusion ends. Secondly, this diffusion model is established on an implicit assumption that the cations have enough time to complete the diffusion process, which is not universally applied given the various processing condition. It thus inspires us to carefully investigate a hidden parameter of importance that guides the phase-segregation: the gel duration (time required for cation diffusion).

### Gel Stage Duration and Phase Segregation

The above diffusion model describes how mobile cations affects the composition evolution in the final perovskite film over the film thickness in the viewpoint of kinetics. However, the cations, once transformed to polycrystalline films, should diffuse much slower as compared to that in the gel. It further suggests the duration of gel as an important parameter that affects the film composition and corresponding phase segregation. Given the same processing conditions (mainly annealing temperature), if the gel duration time is strictly regulated to suppress the cation diffusion, it is possible to avoid phase segregation in the layered 2D perovskite films.

Here, we employ a new precursor solution with two solvents, tetrahydrofuran (THF) and acetonitrile (MeCN), to deposit the perovskite thin films with the nominal formula of $BA_2MA_3Pb_4I_{13}$. At the same processing temperature, the gel duration is much shorter since the solvents THF/MeCN evaporate much faster owing to the low boiling points (BP). Figure 5a shows the PL pattern, the emission peak from the front is almost the same as that from the back side, which indicates negligible phase segregation. We checked the UV/Vis absorption spectra (Supporting Information, Figure S11) to find the absence of any appreciable components with low $n$ value. Furthermore, the ToF-SIMS profile in Figure 5b confirms that all signature species, including $MA^+$, $BA^+$, as well as $Pb^+$, distributed uniformly in the entire film. Combining the PL and ToF-SIMS results, it is claimed that this low BP solvent system efficiently suppresses the phase segregation along the film depth direction. We also checked the crystallinity and crystal orientation (Supporting Information, Figure S11) of the film and found it was different from that of the film prepared by the conventional solvents. How to balance the phase segregation and crystallinity is still an open question. Recently, Qing and co-workers found adding DMSO into the DMF solvent system can greatly improve the crystallinity and device performance.[24a] Other technique such as vacuum poling was also proved to be beneficial to the crystallization.[24b] These results demonstrated that by controlling gel stage, it is possible to improve crystallinity. We believe solvent engineering and other technique of relevance based on the understanding of gel stage may be further developed in the near future.

To further investigate the influence of gel duration, another higher BP solvent dimethylacetamide (DMAC) is introduced into the precursor system to modulate the gel duration (Supporting Information, Table S1). The TGA results of as-casted films in Figure 5c confirms the extension of gel stage duration. For the pure THF–MeCN precursor, no obvious weight change from beginning to the end. While, the DMAC-50 sample (with 50 μL addition of DMAC in the mixture) exhibits a continuous weight loss reaches to the maximum point after 3 min, which is further extended to 3.9 and 5 min for that of the DMAC-100 and DMAC-150 sample, respectively. We also noted that though the gel stage duration extended, the interaction between precursor and solution may be affected as well. At current stage, it is still a big challenge
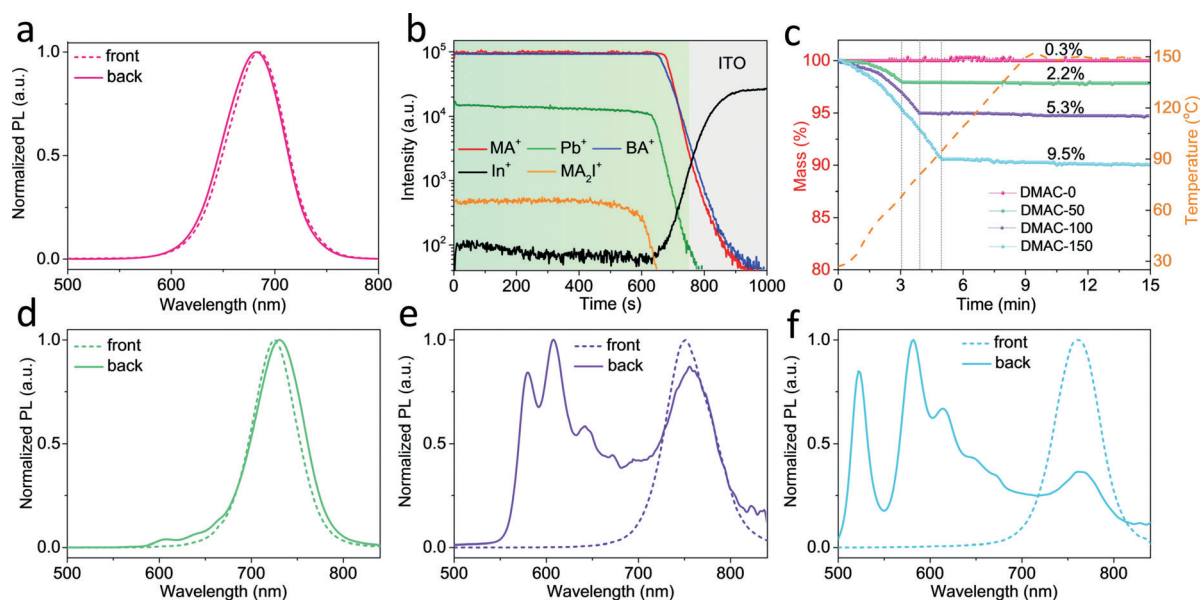


***Figure 5.*** Gel stage duration and segregation. PL spectrum of $BA_2MA_3Pb_4I_{13}$ films prepared by different addition dosage of DMAC based on the THF–MeCN solvent system a) 0 μL, d) 50 μL, e) 100 μL, and f) 150 μL. b) ToF-SIMS result of $BA_2MA_3Pb_4I_{13}$ film prepared by the THF–MeCN. c) TGA curves of the as-cast gel films prepared with different solvents.

to change the gel duration time while keep other conditions constant. We hope future research could focus on this issue and provide appropriate solutions.

Figure 5d shows the PL spectra of DMAC-50 sample. Both the back and front spectra feature the main peak at the region of 720–730 nm. Interestingly, two extra satellite peaks corresponding to the $n = 3$ and 4 phases appear in the spectra from back side, indicating the phase segregation occurred. With the longer gel duration, the DMAC-100 sample showed stronger intensity of emission from small n phases (Figure 5e), indicative of phase segregation. Further increase the concentration of DMAC (Figure 5f), the relative intensity of the long wavelength region decreases dramatically in the spectra from back side, and the peak of the $n = 2$ and $n = 1$ become stronger, indicating the small $n$ species dominate the bottom of the film. The above demonstration proves that the gel stage duration is also an important factor for the diffusion and phase segregation. More importantly, the adjusting of the gel duration by precursor tuning is an effective strategy for achieving homogeneous and phase segregation free perovskite films in the mixed cations systems.

## Conclusion

We carefully investigate the gel stage during halide perovskite film growth, which has been neglected to date. We adopt the diffusion model obeying Fick's second law of diffusion to simulate the cation diffusion process at the gel stage before crystallization. It is illustrated that the diffusivity difference of A-site cations affects local chemical concentration, which is further amplified by processing temperature to result in substantial phase segregation. This model reveals the vertical phase distribution in mixed-cation perovskites, that is, high n-value species prefer to stay at the film surface, while the low n-value analogues mainly concentrated on the bottom. Given higher temperature and/or wider diffusivity gap between A-site cations, phase segregation aggravates. Moreover, we reveal the gel duration can be regulated by adoption of low BP solvents, which suppresses the cation diffusion. It further leads to the successfully fabrication of a vertically homogenous layered 2D perovskite films with negligible segregation.

The halide perovskites with mixed cations/anions are promising for practical applications, while the difference in cations (also anions) are worthy of careful attention. The gel stage during film processing unveils the cation difference in the kinetic viewpoint. By carefully investigating the gel stage, other characteristics of cations can be explored hopefully. This in-depth understanding of gel stage and diffusion process will benefit the future development of mixed perovskites for highly reliable and high-performance optoelectronic devices.

## Acknowledgements

## Conflict of interest

The authors declare no conflict of interest.

[1] a) L. Mao, C. C. Stoumpos, M. G. Kanatzidis, *J. Am. Chem. Soc.* **2019**, *141*, 1171–1190; b) M. A. Green, A. Ho-Baillie, H. J. Snaith, *Nat. Photonics* **2014**, *8*, 506–514; c) M. Grätzel, *Nat. Mater.* **2014**, *13*, 838–842; d) L. Liu, S. Huang, Y. Lu, P. Liu, Y. Zhao, C. Shi, S. Zhang, J. Wu, H. Zhong, M. Sui, H. Zhou, H. Jin, Y. Li, Q. Chen, *Adv. Mater.* **2018**, *30*, 1800544.

[2] a) N. J. Jeon, J. H. Noh, W. S. Yang, Y. C. Kim, S. Ryu, J. Seo, S. I. Seok, *Nature* **2015**, *517*, 476–480; b) G. E. Eperon, S. D. Stranks, C. Menelaou, M. B. Johnston, L. M. Herz, H. J. Snaith, *Energy Environ. Sci.* **2014**, *7*, 982–988; c) J. W. Xiao, L. Liu, D. Zhang, N. De Marco, J. W. Lee, O. Lin, Q. Chen, Y. Yang, *Adv. Energy Mater.* **2017**, *7*, 1700491.

[3] a) W. Li, M. U. Rothmann, A. Liu, Z. Wang, Y. Zhang, A. R. Pascoe, J. Lu, L. Jiang, Y. Chen, F. Huang, Y. Peng, Q. Bao, J. Etheridge, U. Bach, Y.-B. Cheng, *Adv. Energy Mater.* **2017**, *7*, 1700946; b) E. T. Hoke, D. J. Slotcavage, E. R. Dohner, A. R. Bowring, H. I. Karunadasa, M. D. McGehee, *Chem. Sci.* **2015**, *6*, 613–617; c) R. E. Beal, D. J. Slotcavage, T. Leijtens, A. R. Bowring, R. A. Belisle, W. H. Nguyen, G. F. Burkhard, E. T. Hoke, M. D. McGehee, *J. Phys. Chem. Lett.* **2016**, *7*, 746–751; d) P. Gratia, G. Grancini, J.-N. Audinot, X. Jeanbourquin, E. Mosconi, I. Zimmermann, D. Dowsett, Y. Lee, M. Grätzel, F. De Angelis, K. Sivula, T. Wirtz, M. K. Nazeeruddin, *J. Am. Chem. Soc.* **2016**, *138*, 15821–15824; e) X. Wang, Y. Ling, X. Lian, Y. Xin, K. B. Dhungana, F. Perez-Orive, J. Knox, Z. Chen, Y. Zhou, D. Beery, K. Hanson, J. Shi, S. Lin, H. Gao, *Nat. Commun.* **2019**, *10*, 695; f) J.-P. Correa-Baena, Y. Luo, T. M. Brenner, J. Snaider, S. Sun, X. Li, M. A. Jensen, N. T. P. Hartono, L. Nienhaus, S. Wieghold, J. R. Poindexter, S. Wang, Y. S. Meng, T. Wang, B. Lai, M. V. Holt, Z. Cai, M. G. Bawendi, L. Huang, T. Buonassisi, D. P. Fenning, *Science* **2019**, *363*, 627–631.

[4] H. Zhang, X. Fu, Y. Tang, H. Wang, C. Zhang, W. W. Yu, X. Wang, Y. Zhang, M. Xiao, *Nat. Commun.* **2019**, *10*, 1088.

[5] a) Y. Hu, E. M. Hutter, P. Rieder, I. Grill, J. Hanisch, M. F. Aygüler, A. G. Hufnagel, M. Handloser, T. Bein, A. Hartschuh, K. Tvingstedt, V. Dyakonov, A. Baumann, T. J. Savenije, M. L. Petrus, P. Docampo, *Adv. Energy Mater.* **2018**, *8*, 1703057; b) D. J.

Kubicki, D. Prochowicz, A. Hofstetter, S. M. Zakeeruddin, M. Grätzel, L. Emsley, *J. Am. Chem. Soc.* **2017**, *139*, 14173–14180.

[6] a) N. Zhou, Y. Shen, L. Li, S. Tan, N. Liu, G. Zheng, Q. Chen, H. Zhou, *J. Am. Chem. Soc.* **2018**, *140*, 459–465; b) J. Liu, J. Leng, K. Wu, J. Zhang, S. Jin, *J. Am. Chem. Soc.* **2017**, *139*, 1432–1435.

[7] a) R. Munir, A. D. Sheikh, M. Abdelsamie, H. Hu, L. Yu, K. Zhao, T. Kim, O. E. Tall, R. Li, D. M. Smilgies, *Adv. Mater.* **2017**, *29*, 1604113; b) X. Zhang, R. Munir, Z. Xu, Y. Liu, H. Tsai, W. Nie, J. Li, T. Niu, D. M. Smilgies, M. G. Kanatzidis, A. D. Mohite, K. Zhao, A. Amassian, S. Liu, *Adv. Mater.* **2018**, *30*, 1707166; c) D. Barrit, A. D. Sheikh, R. Munir, J. M. Barbé, R. Li, D.-M. Smilgies, A. Amassian, *J. Mater. Res.* **2017**, *32*, 1899–1907.

[8] a) K. Wang, M.-C. Tang, H. X. Dang, R. Munir, D. Barrit, M. De Bastiani, E. Aydin, D.-M. Smilgies, S. De Wolf, A. Amassian, *Adv. Mater.* **2019**, *31*, 1808357; b) H. X. Dang, K. Wang, M. Ghasemi, M.-C. Tang, M. De Bastiani, E. Aydin, E. Dauzon, D. Barrit, J. Peng, D.-M. Smilgies, S. De Wolf, A. Amassian, *Joule* **2019**, *3*, 1746–1764; c) Y. Zhang, P. Wang, M.-C. Tang, D. Barrit, W. Ke, J. Liu, T. Luo, Y. Liu, T. Niu, D.-M. Smilgies, Z. Yang, Z. Liu, S. Jin, M. G. Kanatzidis, A. Amassian, S. F. Liu, K. Zhao, *J. Am. Chem. Soc.* **2019**, *141*, 2684–2694; d) R. Quintero-Bermu- dez, A. Gold-Parker, A. H. Proppe, R. Munir, Z. Yang, S. O. Kelley, A. Amassian, M. F. Toney, E. H. Sargent, *Nat. Mater.* **2018**, *17*, 900–907.

[9] a) T. Liu, Y. Jiang, M. Qin, J. Liu, L. Sun, F. Qin, L. Hu, S. Xiong, X. Jiang, F. Jiang, P. Peng, S. Jin, X. Lu, Y. Zhou, *Nat. Commun.* **2019**, *10*, 878; b) Y. Lin, Y. Fang, J. Zhao, Y. Shao, S. J. Stuard, M. M. Nahid, H. Ade, Q. Wang, J. E. Shield, N. Zhou, A. M. Moran, J. Huang, *Nat. Commun.* **2019**, *10*, 1008.

[10] H. Tsai, W. Nie, J.-C. Blancon, C. C. Stoumpos, R. Asadpour, B. Harutyunyan, A. J. Neukirch, R. Verduzco, J. J. Crochet, S. Tretiak, *Nature* **2016**, *536*, 312–316.

[11] a) M. Yuan, L. N. Quan, R. Comin, G. Walters, R. Sabatini, O. Voznyy, S. Hoogland, Y. Zhao, E. M. Beauregard, P. Kanjana- boos, *Nat. Nanotechnol.* **2016**, *11*, 872–877; b) N. Wang, L. Cheng, R. Ge, S. Zhang, Y. Miao, W. Zou, C. Yi, Y. Sun, Y. Cao, R. Yang, Y. Wei, Q. Guo, Y. Ke, M. Yu, Y. Jin, Y. Liu, Q. Ding, D. Di, L. Yang, G. Xing, H. Tian, C. Jin, F. Gao, R. H. Friend, J. Wang, W. Huang, *Nat. Photonics* **2016**, *10*, 699–704.

[12] A. Z. Chen, M. Shiu, J. H. Ma, M. R. Alpert, D. Zhang, B. J. Foley, D.-M. Smilgies, S.-H. Lee, J. J. Choi, *Nat. Commun.* **2018**, *9*, 1336.

[13] a) F. Wang, X. Jiang, H. Chen, Y. Shang, H. Liu, J. Wei, W. Zhou, H. He, W. Liu, Z. Ning, *Joule* **2018**, *2*, 2732–2743; b) P. Löper, M. Stuckelberger, B. Niesen, J. Werner, M. Filipič, S.-J. Moon, J.-H. Yum, M. Topič, S. De Wolf, C. Ballif, *J. Phys. Chem. Lett.* **2015**, *6*, 66–71.

[14] a) K. Yan, M. Long, T. Zhang, Z. Wei, H. Chen, S. Yang, J. Xu, *J. Am. Chem. Soc.* **2015**, *137*, 4460–4468; b) D. P. McMeekin, Z. Wang, W. Rehman, F. Pulvirenti, J. B. Patel, N. K. Noel, M. B. Johnston, S. R. Marder, L. M. Herz, H. J. Snaith, *Adv. Mater.* **2017**, *29*, 1607039.

[15] Q. Hu, L. Zhao, J. Wu, K. Gao, D. Luo, Y. Jiang, Z. Zhang, C. Zhu, E. Schaible, A. Hexemer, C. Wang, Y. Liu, W. Zhang, M. Grätzel, F. Liu, T. P. Russell, R. Zhu, Q. Gong, *Nat. Commun.* **2017**, *8*, 15688.

[16] L. N. Quan, M. Yuan, R. Comin, O. Voznyy, E. M. Beauregard, S. Hoogland, A. Buin, A. R. Kirmani, K. Zhao, A. Amassian, *J. Am. Chem. Soc.* **2016**, *138*, 2649–2655.

[17] J. Crank, *The mathematics of diffusion*, Oxford university press, Oxford, **1979**.

[18] a) J. F. Kincaid, H. Eyring, A. E. Stearn, *Chem. Rev.* **1941**, *28*, 301–365; b) A. E. Steam, E. M. Irish, H. Eyring, *J. Phys. Chem.* **1940**, *44*, 981–995.

[19] W. Fei, H.-J. Bart, *Chem. Eng. Technol.* **1998**, *21*, 659–665.

[20] P. Cheng, Z. Xu, J. Li, Y. Liu, Y. Fan, L. Yu, D.-M. Smilgies, C. Müller, K. Zhao, S. F. Liu, *ACS Energy Lett.* **2018**, *3*, 1975–1982.

[21] a) K. Domanski, J.-P. Correa-Baena, N. Mine, M. K. Nazeer- uddin, A. Abate, M. Saliba, W. Tress, A. Hagfeldt, M. Grätzel, *ACS Nano* **2016**, *10*, 6306–6314; b) T. Zhang, X. Meng, Y. Bai, S. Xiao, C. Hu, Y. Yang, H. Chen, S. Yang, *J. Mater. Chem. A* **2017**, *5*, 1103–1111.

[22] C. Zhu, X. Niu, Y. Fu, N. Li, C. Hu, Y. Chen, X. He, G. Na, P. Liu, H. Zai, Y. Ge, Y. Lu, X. Ke, Y. Bai, S. Yang, P. Chen, Y. Li, M. Sui, L. Zhang, H. Zhou, Q. Chen, *Nat. Commun.* **2019**, *10*, 815.

[23] a) P. Cheng, P. Wang, Z. Xu, X. Jia, Q. Wei, N. Yuan, J. Ding, R. Li, G. Zhao, Y. Cheng, K. Zhao, S. F. Liu, *ACS Energy Lett.* **2019**, *4*, 1830–1838; b) T. Niu, J. Lu, X. Jia, Z. Xu, M.-C. Tang, D. Barrit, N. Yuan, J. Ding, X. Zhang, Y. Fan, T. Luo, Y. Zhang, D.-M. Smilgies, Z. Liu, A. Amassian, S. Jin, K. Zhao, S. Liu, *Nano Lett.* **2019**, *19*, 7181–7190.

[24] a) J. Qing, X. K. Liu, M. Li, F. Liu, Z. Yuan, E. Tiukalova, Z. Yan, M. Duchamp, S. Chen, Y. Wang, *Adv. Energy Mater.* **2018**, *8*, 1800185; b) J. Zhang, J. Qin, M. Wang, Y. Bai, H. Zou, J. K. Keum, R. Tao, H. Xu, H. Yu, S. Haacke, B. Hu, *Joule* **2019**, *3*, 3061–3071.

# Probing Phase Distribution in 2D Perovskites for Efficient Device Design

Na Liu,[†,∥] Pengfei Liu,[†,∥] Haoxiang Ren,[†] Haipeng Xie,[§] Ning Zhou,[‡] Yongli Gao,[§] Yujing Li,[†] Huanping Zhou,[‡] Yang Bai,*[,†] and Qi Chen*[,†]

[†]School of Materials Science and Engineering, Beijing Institute of Technology, Beijing 100081, P. R. China

[‡]Beijing Key Laboratory for Theory and Technology of Advanced Battery Materials, Department of Materials Science and Engineering, Department of Energy and Resources Engineering, College of Engineering, Peking University, Beijing 100871, P. R. China

[§]Hunan Key Laboratory for Super-microstructure and Ultrafast Process, School of Physics and Electronics, Central South University, Changsha 410083, P. R. China

**S** Supporting Information

**ABSTRACT:** Two-dimensional (2D) lead halide perovskite has recently been recognized as a promising candidate to stabilize perovskite solar cells due to its extraordinary moisture resistance. These 2D perovskite films often consist of multiple phases with layered ($n$) lead halide (from $n$ = 1, 2, 3 to ≈∞). However, a convincing evidence is still lacking to clarify the phase distribution with respect to different $n$, thus causes the misleading for device design. Herein, confocal photoluminescence (PL) spectroscopy was applied to probe the inhomogeneity of 2D perovskite films along the vertical direction to construct a clear-phase distribution mapping consequently. It reveals that the 2D perovskite phases ($n$ = 2, 3, 4) locate preferentially near the substrate, while large $n$ phases are predominantly near the top surface. Moreover, we successfully developed a simple method to manipulate the phase distribution in 2D perovskite thin films, which results in a dramatic increase of device efficiency from 4.95 to 11.6%. Our findings thus provide insights to the understanding of 2D perovskite film growth. The utilization of visualized phase distribution data could also guide the further development of 2D perovskite materials for optoelectronic devices.

**KEYWORDS:** 2D perovskite, phase distribution, growth manipulation, charge transfer, heating−spinning method
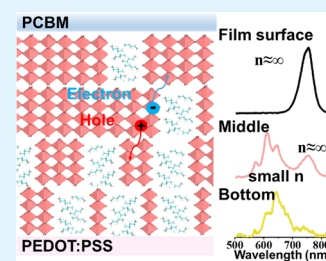
## INTRODUCTION

In recent years, metal halide perovskite solar cells (PSCs) have attracted tremendous attentions due to their rapid increase in power conversion efficiency (PCE), which has risen unprecedentedly from 3.8 to 25.2%.[1−7] However, long-term stability of the materials and devices remains to be the biggest challenge that hinders their further application.[8−14] Recently, two-dimensional (2D) organolead halide perovskites, in addition to their three-dimensional (3D) analogues, have emerged as an attractive material for photovoltaics and other optoelectronic device applications due to their superior stability properties.[15−25]

The typical structure used in photovoltaic applications was the Ruddlesden−Popper (RP) phase 2D perovskite with a formula of $A_2(CH_3NH_3)_{n-1}M_nX_{3n+1}$, where A is a large aliphatic or aromatic alkylammonium cation, M is the metal cation, which is usually $Pb^{2+}$, and X is the halide anion.[26,27] The integer $n$ is the layer number of inorganic perovskite octahedron between two larger organic cation spacers (A), which can be tuned by adjusting the ratio of a spacer cation to a small organic cation. In previous studies, 2D PSCs showed poor PCEs of only 4−5% due to its low carrier mobility and short diffusion length caused by the large-size spacers.[15] Kanatzidis et al. introduced a preheating deposition method to

enable the growth of 2D perovskite films with perpendicularly oriented inorganic framework on the substrates, thus facilitated the charge transport, resulting in an enhanced PCE of 12.5%.[17] This work effectively pushed the development of 2D perovskite solar cells, but at that time, an important issue was neglected, the phase problem. Recently, works of both Sargent et al. and Huang et al. have reported that mixing phases existed in the 2D perovskite film, and the carrier transfer mechanism could not be simply described by a pure 2D perovskite model.[18,28] Furthermore, the work of Jin et al. also showed that multiple perovskite phases coexisted on the nominal $n$ = 4 2D perovskite film, and from the transient absorption spectra analysis, they successfully observed the charge transfer between 2D perovskite phases with a different $n$ value.[29]

To date, although more and more works have proved the coexistence of multiple phases in a 2D perovskite film, the real distribution of different phases is still unclear. Furthermore, the model has always been ignored or simply described as a "pure" 2D perovskite in the high-performance device, which is
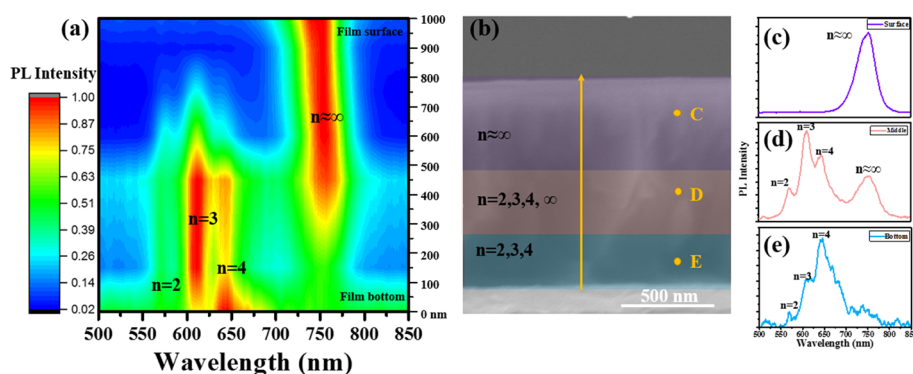
**Figure 1.** (a) Cross-sectional line scanning confocal PL mapping spectrum and (b) SEM image of the 2D perovskite film. (c−e) PL spectrum of points C, D, and E corresponded to different three regions marked in panel (b).

strongly controversial with the theoretical results. Most importantly, the unclear phase distribution behavior would further mislead the design for photovoltaic devices, slowing down the research development. Thus, it is crucial to identify the relationship between phases and spatial distribution, which would strongly benefit the design of materials and devices based on a 2D perovskite.

In this work, we used photoluminescence (PL) mapping technology to characterize the cross section of the 2D perovskite film, and for the first time, the spatial distribution of different perovskite phases was obtained. We found that the top area of the 2D perovskite films consisted mainly of the $n \approx \infty$ perovskite phase, and the middle part was a coexistence of $n = 2, 3, 4$ and $\approx\infty$ perovskite phases, while only small $n$ phases could be detected at the bottom of the film. More importantly, we effectively adjusted the 2D perovskite phase distribution by manipulating the crystallization kinetics with a developed heating−spinning method. A 2D perovskite film with a better charge transfer behavior and suitable surface Fermi level was obtained, and the well-designed device employed an enhanced current density, which was 80% higher than the control sample, resulting in a highly improved PCE of 11.6%.

## ■ RESULTS AND DISCUSSION

**2D Perovskite Phase Arrangement.** Normally, the 2D perovskite films, prepared with a precursor composition of $n = 4$, are found to be a mixture of multiple perovskite phases with $n = 2, 3, 4$ and $\approx\infty$, which have already been clearly identified from the absorption and PL spectra, as shown in Figures S1 and S2.[29,30] However, the distribution of multiple perovskite phases within the film is still unclear.[29] In part of previous literatures, 2D perovskite films were described as being arranged in the order of $n$ in a direction perpendicular to the substrate.[29] Meanwhile, the others suggested that the multiple perovskite phases were disordered in the film.[18] To determine the distribution of multiple perovskite phases, for the first time, the confocal PL mapping technology is used to characterize the cross-sectional 2D perovskite film as their obvious band gap differences can be easily visualized by the PL position. The $XY$ mode of PL mapping measurement is used, the schematic diagram of the $XY$ mode for cross-sectional PL mapping characterization is shown in Figure S3, and the PL resolution of this instrument is 200 nm, which is limited by the laser spot size. A 2D perovskite film with a thickness around 1000 nm is prepared, and the corresponding cross-sectional scanning electron microscopy (SEM) image is shown in Figure1b. Meanwhile, a line scanning PL mapping spectrum along the

yellow line (as shown in Figure 1b) is present in Figure 1a. From the PL mapping spectrum, obvious changes on the peak positions can be observed within the film from top to bottom. Only one emission peak belonging to the $n \approx \infty$ 2D phase exists at the near surface region of the film.[29] During the movement of detection position from the top area to the middle part, the PL emission intensity of the $n \approx \infty$ 2D perovskite phase becomes weaker; at the same time, emission peaks belonging to the small $n$ 2D perovskite phases become much stronger. Meanwhile, when near the bottom of the film, the $n \approx \infty$ perovskite phase disappeared with only the small $n$ phases existing. In general, the distribution of multiple perovskites can be divided into three regions, the $n \approx \infty$ 2D region, the mixed region, and the small $n$ 2D region. As the resolution of confocal microscopy is limited to 200 nm, the entire perovskite film can be divided into three regions, with a thickness about 300 nm based on the PL spectrum evolution trend. The PL spectrum of these three regions is also presented in Figure 1c−e, and three representative points are selected, as shown in Figure 1b. Furthermore, the photos of machine data from different points at the cross section of the perovskite film are also shown in Figure S4. It can be clearly seen that the upper part is the $n \approx \infty$ 2D perovskite phase, the middle part is a mixture of the small $n$ and $n \approx \infty$ 2D perovskite phase, and the bottom part is only the small $n$ 2D perovskite phases. Based on the above results, the composition distribution in the 2D perovskite film is well identified, and the visualized evidence proved that the different $n$ value 2D perovskite phases are aligned in a particular order instead of a disordered mixture.

**Phase Distribution Manipulation.** To facilitate the carrier diffusion and to enhance the photovoltaic performance, the distribution of internal multiple 2D perovskite phases is manipulated by controlling the crystallization kinetics. Here, a developed deposition strategy, the heating−spinning method, is proposed, in which the substrate temperature remains constant throughout the whole spin-coating process. A series of 2D perovskite films are prepared by varying the spinning temperature, the corresponding top-view SEM images are shown in Figure 2a−c, and the cross-sectional SEM image is presented in Figure S5. It is clear that the grain size, amount of pinholes, and film coverage are greatly influenced by the heating−spinning temperature. First, the coverage of the perovskite film is highly improved when rising the heating temperature. The film deposited under 30 °C shows poor coverage with large numbers of large-size pinholes. Furthermore, when the temperature increases to 70 °C, the pinhole
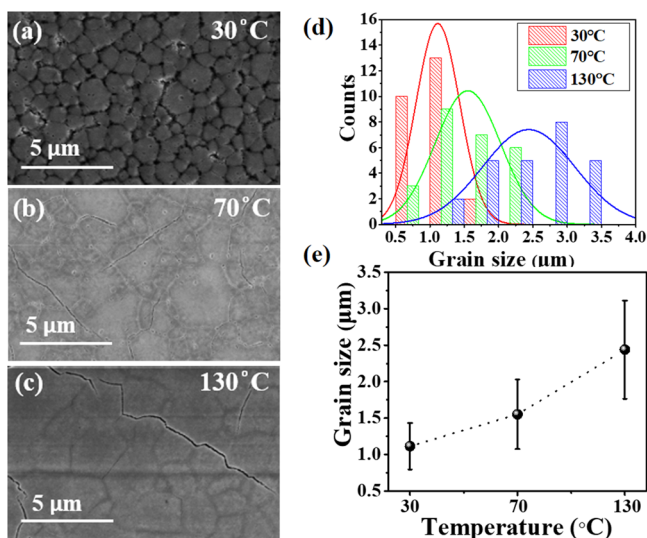
**Figure 2.** (a−e) Top-view SEM images of the 2D perovskite films fabricated under different heating−spinning temperatures of (a) 30, (b) 70, and (c) 130 °C. (d) Histogram of the 2D perovskite grain size for temperatures of 30, 70, and 130 °C and fitted with normal distribution curves. (e) Plot of the average 2D perovskite grain size versus temperature. The error bar represents standard deviation.

disappeared, and the film employs a full coverage. Besides that, the average grain size of a 2D perovskite is also increased under higher spinning temperature as 1 $\mu$m for 30 °C, 1.5 $\mu$m for 70 °C, and 2.0 $\mu$m for 130 °C. The grain size distribution is summarized in Figure 2d and is plotted as a function of substrate temperature in Figure 2e. Furthermore, the crystallinity of the 2D perovskite film is studied by X-ray diffraction (XRD) patterns (Figure S6), and the trends of full width at half-maximum (FWHM) of diffraction peaks of 13.9 and 28.2° are summarized in Table S1. When the temperature increases from 30 to 70 °C, the value of FWHM decreases, indicating a better crystallinity of the perovskite crystal. However, further increase of the temperature results in the broadening of FWHM due to the reduced crystal quality. Thus, the 2D perovskite fabricated under 70 °C exhibits the

best crystallinity with a fully covered surface and fewer number of pinholes. The results illustrate that the 2D perovskite crystallization process closely correlates to the heating temperature. We also investigate the film via grazing-incidence wide-angle X-ray scattering (GIWAX), as shown in Figure S7. The 2D perovskite film shows sharp and discrete Bragg spots, which indicate the highly oriented crystal grain with (111) planes parallel to the substrate surface, proving the existence of 2D perovskite phases.

In addition, photoluminescence spectroscopy is character-ized to investigate the internal 2D perovskite phase distribution under different spinning temperatures. Figure 3a,b shows the PL spectra obtained from the front (the perovskite excited from the surface is defined as the front PL) and back side excitation (the perovskite excited from glass substrate side is defined as the back PL), respectively. As the distribution of perovskite phases has already been confirmed in previous discussions, in which the large $n$ phase is located at the upper surface and the small $n$ phase is located at the bottom of the film, the one emission peak from the front spectra is attributed to the 2D perovskite phase with $n \approx \infty$. From Figure 3a, an obvious redshift of emission peak is presented, in which the PL peak position gradually shifts from 763.5 nm for 30 °C to 767.5, 767.8, 771.5, 781.5, and 782 nm for 50, 70, 90, 110, and 130 °C, respectively. The redshift is due to the reduction of the band gap ($E_g$) of the $n \approx \infty$ phase 2D perovskite, indicating that the perovskite near the surface is much closer to the 3D structure with a much larger $n$ value when under a higher spinning temperature. At the same time, from the back excitation in Figure 3b, the five PL emission peaks are attributed to the perovskite phase with $n = 1, 2, 3, 4$ and $\approx\infty$.[26] The emission intensity from the small $n$ phase becomes stronger with the rising of spinning temperature, indicating that the amount of small $n$ phase perovskite increases, which is also in agreement with the results obtained from the front excitation. The above results prove that high spinning temperature is beneficial for the growth of the small $n$ phase perovskite at the bottom of the film. So, tuning the heating−spinning temperature should be an effective and simple way to manipulate the distribution of different 2D perovskite phases. Based on the steady-state PL measurement results (Figure
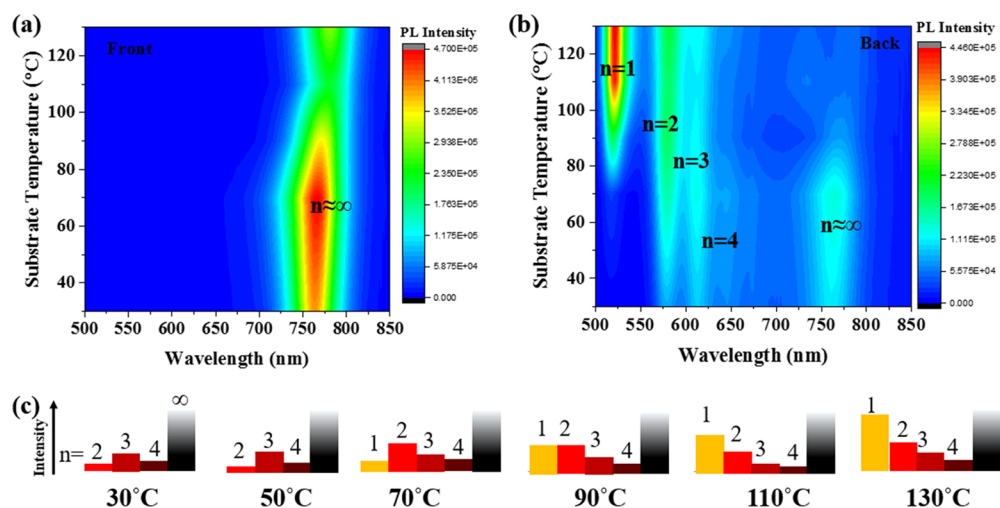


**Figure 3.** (a, b) Steady-state photoluminescence (PL) spectra of the 2D perovskite films based on different spinning temperature excited from (a) perovskite and (b) glass sides. (c) Schematic diagram of multiple $n$ 2D perovskite phase distribution. All the samples were fabricated on the glass substrate.
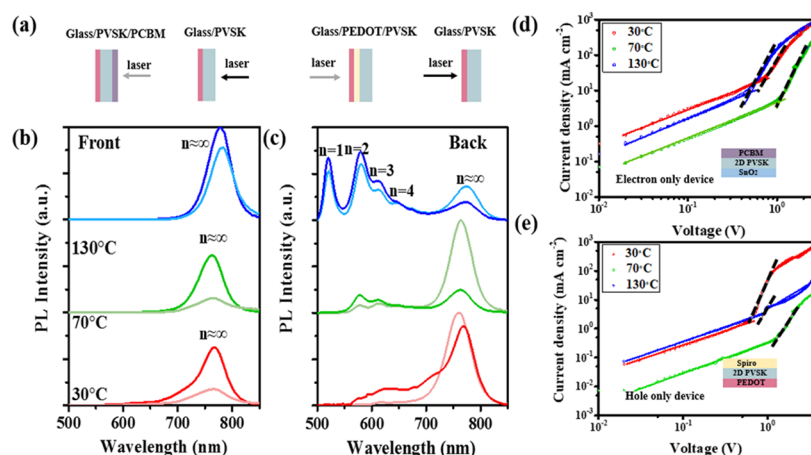
**Figure 4.** (a) Schematic diagram of device structures for steady-state PL spectra measurement. (b, c) Steady-state PL spectra of 2D perovskite films prepared at 30, 70, and 130 °C excited from the (b) front and (c) back sides; here, the light color represents the spectra obtained from the structure with a transport layer (glass/2D perovskite/PCBM or glass/PEDOT:PSS/2D perovskite), and the dark color represents the spectra obtained from the structure without a transport layer (glass/2D perovskite). Current−voltage curve for (d) an electron-only 2D perovskite device and (e) a hole-only 2D perovskite device. The insets show the device structures of electron-only and hole-only 2D perovskite devices. (The black dashed lines refer to the trap-SCLC region, while the left and right parts refer to the Ohmic and SCLC regions, respectively).

3a,b), the corresponding distribution of different $n$ value 2D perovskite under different spinning temperatures is summarized in Figure 3c, which clearly shows the relation between small $n$ phases and spinning temperature.

**Carrier Transfer Behavior.** In this part, the influence of internal 2D perovskite phase distribution on the carrier transport is investigated. The PL measurement is used to characterize the carrier transportation within the film. Based on the mechanism of the electron and hole transfers in the 2D perovskite film, in which the photo-induced electron transfer from the film bottom to the surface and the hole transfer from the film surface to the bottom, various device structures are designed for PL measurement (glass/perovskite/PCBM and glass/PEDOT:PSS/perovskite) to characterize the charge transfer behavior. The corresponding schematic illustration is presented in Figure 4a. As shown in Figure 4b, the intensity of front PL spectra obtained from the sample with the structure of glass/2D perovskite/PCBM is weaker than that from the glass/2D perovskite sample due to the extraction of photo-electron by the PCBM layer, which reduces the radiation recombination. Interestingly, when comparing the back PL spectra of samples grown on PEDOT:PSS with the one without PEDOT:PSS, as shown in Figure 4c, the intensity of PL peaks belonging to the small $n$ 2D perovskite phase decreases, while that of the $n \approx \infty$ 2D perovskite phase is enhanced. The carrier transfer mechanism can be used to explain this phenomenon, which suggests that the hole transport to the bottom is extracted by PEDOT:PSS, while the electron transfers upwards and is accumulated in the large $n$ 2D perovskite phase. As a result, the peak intensity of small $n$ phase 2D perovskite is weakened, and that of the $n \approx \infty$ 3D perovskite is enhanced. The results from the PL spectra change are consistent with a previous report.[29] PL spectra of 2D perovskite films with fitted peaks are presented in Figure S8. Comparing the integral areas of the $n \approx \infty$ 2D perovskite phase in Figure 4b,c, the corresponding separation efficiency of electrons and holes can be obtained and is summarized in Table S2, indicating that the 2D perovskite film obtained under 70 °C exhibits the most efficient charge separation.

In the following, ultraviolet photoelectron spectroscopy (UPS) and X-ray photoelectron spectroscopy (XPS) are applied to probe the work function (WF) and element binding energy of the perovskite film surface to investigate the interfacial carrier transfer. Figure S9 shows the values of valence and conduction bands, and the film fabricated under 70 °C has the most suitable band alignment with the PCBM layer, which would benefit the electron extraction. In Figure S10, the XPS spectra show variation of the binding energy of Pb 4f and I 3d, which is consistent with the WF change obtained from UPS. Furthermore, the detailed parameters are summarized in Table S3.

The space charge limit current (SCLC) measurement is performed to characterize the electron and hole mobility in 2D perovskite-based devices.[5,31] The electron mobility of the 2D perovskite film is measured using an electron-only device with the structure of ITO/SnO$_2$/perovskite/PCBM/Au, while the structure of PEDOT:PSS/perovskite/Spiro/Au is used for hole-only devices. Figure 4d,e shows the dark current density−voltage ($J$−$V$) and fitted curves of the electron- and hole-only devices with three representative fabricating temperatures. According to eq 1

$$J_D = \frac{9\varepsilon\varepsilon_0\mu V_b^2}{8L^3} \qquad (1)$$

where $V_b$ is the applied voltage, $\varepsilon$ is the relative dielectric constant of the 2D perovskite film (the value of BA$_2$MA$_3$Pb$_4$I$_{13}$ was used), $\varepsilon_0$ is the vacuum permittivity, and $L$ is the thickness of the 2D perovskite film.

Deriving from the curve fitting, the electron mobility is 4.44 × 10$^{-3}$, 5.64 × 10$^{-2}$, and 6.68 × 10$^{-2}$ cm$^2$ V$^{-1}$ s$^{-1}$, and the hole mobility is 6.63 × 10$^{-3}$, 6.34 × 10$^{-2}$, and 5.09 × 10$^{-2}$ cm$^2$ V$^{-1}$ s$^{-1}$ for 30, 70, and 130 °C, respectively. The 2D perovskite films prepared under 70 °C presents both the highest electron and hole mobility. By lowering the spinning temperature leads to the film with poor quality and more defects, the carrier transport is hindered. On the other hand, higher temperature results in the increase of small $n$ perovskite phases at the bottom, whose large exciton binding energy strongly recombines the charges before reaching the extraction layers,
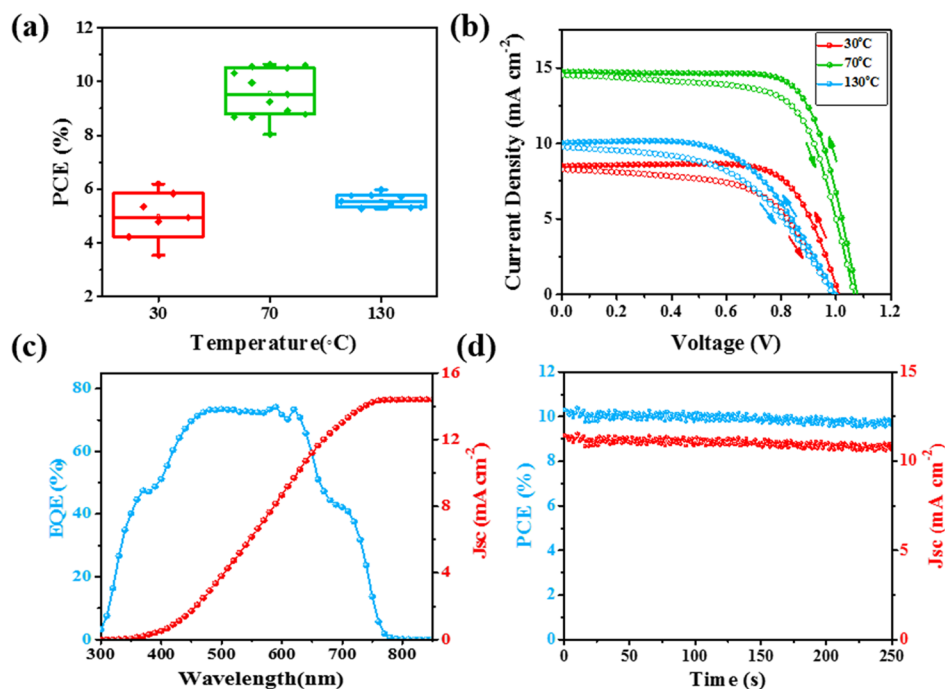
**Figure 5.** (a) Distribution of power conversion efficiency (PCE) versus spinning temperature. (b) $J-V$ curves for the device fabricated under temperatures of 30, 70, and 130 °C measured by forward and reverse scans with a 0.1 cm$^2$ active area. (c) EQE spectra together with integrated $J_{SC}$ for the champion device of a 2D perovskite solar cell. (d) Steady-state photocurrent measured under a bias voltage of 0.92 V near the maximum power point with a 0.1 cm$^2$ active area.

and at the same time forms poor band alignment between perovskite and PEDOE:PSS. The SCLC measurements results also agree well with the above PL results, illustrating that the film obtained under 70 °C performs the best carrier transfer behavior among all the samples.

**Photovoltaic Performance.** To evaluate the influence of crystallization kinetics on photovoltaic performance, the solar cell with planner p−i−n device configuration is prepared, and the layered 2D perovskite material as the light-absorbing layer is sandwiched between p-type (PEDOT:PSS) and n-type (PCBM) contact layers. The PCE of devices is analyzed and is plotted as the function of spinning temperature, as shown in Figure 5a, and other photovoltaic parameter ($J_{SC}$, $V_{OC}$, and FF) distributions of devices are given in Figure S11. The overall PCE of the 2D perovskite solar cells increases from 30 °C (PCE = 4.95 ± 0.90%) during the rising of fabrication temperature and reaches to a maximum value at 70 °C (PCE = 9.73 ± 0.78%). The low PCE obtained from the device prepared at low temperature is mainly due to the unfavored phase distribution and lower crystallinity with too many defects, which are not suitable for carrier transfer. However, by further increasing the spinning temperature, the PCE gradually drops to 5.56 ± 0.21% (130 °C) due to an unfavored interface band alignment. The $J-V$ curves with forward and reverse scan directions for the device fabricated under 30, 70, and 130 °C are shown in Figure 5b, and the device fabricated under 70 °C shows the smallest hysteresis. The corresponding photovoltaic parameters are summarized in Table S4. The champion device, obtained under a spinning temperature of 70 °C, exhibits a $V_{OC}$ of 1.07 V, an FF of 67.61%, and a $J_{SC}$ of 14.76 mA/cm$^2$, yielding a PCE of 11.6%. The corresponding cross-sectional SEM image of the champion device prepared under 70 °C heating−spinning temperature is shown in Figure S12. Comparing with devices under other conditions, except for

the higher $V_{OC}$ of 1.07 V, which indicates the low nonradiative recombination, the highly improved $J_{SC}$ value is the main reason for the PCE enhancement. The higher $J_{SC}$ can be attributed to the efficient carrier separation and transportation within the device, which is also consistent with our previous analysis on the charge separation efficiency and carrier mobility. Besides that, the forward and reverse scanning current density−voltage ($J-V$) curves also show negligible hysteresis in the resulting device due to the suitable energy alignment-induced efficient interfacial charge extraction. The external quantum efficiency (EQE) spectra of the best performance device are also recorded and show the absorption wavelength range of 300−800 nm, as shown in Figure 5c. The integrated photocurrent density is 12.4 mA/cm$^2$, which is in good agreement with the $J_{SC}$ obtained from the $J-V$ measurement. By holding a bias voltage at near the maximum power output point (0.92 V), we also obtain a stabilized photocurrent of 11.2 mA/cm$^2$, corresponding to a stabilized efficiency of 10.4%, as presented in Figure 5d. From the temperature-dependent results, we demonstrate that carrier separation and transportation in the 2D perovskite film are significantly improved by optimizing the crystallization kinetics process.

## ■ CONCLUSIONS

In conclusion, we first applied the confocal PL mapping method to visualize the phase distribution of layered lead halide $n$ in a 2D perovskite film, wherein low $n$ phases decreased along the vertical direction starting from the substrate. Furthermore, we developed a facile strategy, the heating−spinning method, to manipulate multiple 2D perovskite phase distribution. The optimized 2D perovskite film enabled improved charge transportation and separation, which is verified by the PL and SCLC measurements. Based on the

optimized energy band alignment and efficient charge transfer behavior, a significant increase of PCE from 3.6 to 11.6% was obtained due to the tremendous enhanced current density. Therefore, our work provides a deeper understanding and visible feature on the 2D perovskite film growth mechanism and introduces an effective method to control the crystallization kinetics of 2D perovskite, which may help to guide the further design of materials and devices based on the 2D perovskite.

## EXPERIMENTAL SECTION

**Material and Precursor Preparation.** Poly(3,4-ethylenedioxythiophene):poly(styrenesulfonate) (PEDOT:PSS) water dispersion (Clevios VP AI 4083) was acquired from Heraeus. Butylamine iodine (BAI), bathocuproine (BCP), and [6,6]-phenyl-$C_{61}$-butyric acid methyl ester ($PC_{61}BM$) were purchased from Xi'an BaoLaiTe Technology Ltd. Methylamine iodide (MAI) was prepared according to the reported procedure. Lead iodide ($PbI_2$; 99.999%), $N,N$-dimethylformamide (DMF; 99.99%), chlorobenzene (CB; 99.9%), and methyl alcohol (MA; 99.9%) were purchased from Sigma-Aldrich. All reagents were used as received without further purification. The 2D perovskite precursor of $PbI_2$:MAI:BAI in a molar ration of 4:3:2 was dissolved in DMF with a concentration of 0.8 mol/L.

**Device Fabrication.** The inverted planar heterojunction 2D perovskite solar cells were fabricated on ITO substrates. The ITO substrates were ultrasonically cleaned with a diluted detergent, deionized water, acetone, ethanol, and isopropanol (IPA) in succession. The as-cleaned substrates were UV−ozone-treated for 20 min. The PEDOT:PSS solution was spin-coated onto the ITO substrates at 3000 rpm for 30 s, and the samples were then annealed at 120 °C for 20 min in air. The perovskite precursor solution was spin-coated on top of the PEDOT:PSS-modified ITO substrate at 2000 rpm for 30 s under various heating−spinning temperature (from 30 to 130 °C). The samples were further annealed on a hot plate at 70 °C for 20 min. Next, 30 $\mu$L of $PC_{61}BM$ (20 mg/mL in CB) solution was then spin-coated on top of the perovskite layer at 2000 rpm for 30 s, BCP (2.5 mg/mL in methanol) was dropped onto $PC_{61}BM$ at a rotational speed of 6000 rpm to form an electron extracting layer, and the samples were annealed on a hot plate at 70 °C for 10 min. Finally, a 100 nm silver electrode was deposited via thermal evaporation under a pressure of $1 \times 10^{-4}$ Pa. The active area was 0.102 cm$^2$.

**Characterization.** UV−visible absorption spectra were recorded with a UV−visible spectrophotometer (Agilent 8453). The XRD patterns were collected by using a PANalytical X'Pert Pro X-ray powder diffractometer with Cu K$\alpha$ radiation ($\lambda$ = 1.54050 Å). The morphology was measured using a scanning electron microscope (S4800). Photoluminescence (PL) mapping was measured by a laser scanning confocal microscope (Enlitech, SPCM-1000) equipped with a 470 pulse laser and galvo-based scanner. Photoluminescence (PL) was measured by FLS980 (Edinburgh Instruments Ltd) with an excitation at 470 nm. Ultraviolet photoelectron spectroscopy (UPS) measurements were carried out on the XPS AXIS Ultra DLD (Kratos Analytical). X-ray photoelectron spectroscopy (XPS) measurements were carried out on a STARPES system (SPECS) with a monochromatic SPEXS XR-MF microwave X-ray source (Al K$\alpha$ 1/4 1486.7 eV). Elemental analyses were performed by using an inductively coupled plasma atomic emission spectrometer (ICP-AES; Leeman PROFILE SPEC) instrument. The current density−voltage characteristics of photovoltaic devices were obtained using a Keithley 2400 source measure unit. The photocurrent was measured under AM1.5 G illumination at 100 mW cm$^2$ using a Newport Thermal Oriel 91192 1000 W solar simulator. The light intensity was calibrated using a KG-5 Si diode. The effective area of each cell was 0.102 cm$^2$, defined by masks for all the photovoltaic devices discussed in this work. External quantum efficiencies (EQEs) were determined on a solar cell quantum efficiency measurement system (QER), provided by Enli Technology Co. Ltd.

## ASSOCIATED CONTENT

**Ⓢ Supporting Information**

The Supporting Information is available free of charge at https://pubs.acs.org/doi/10.1021/acsami.9b17047.

Absorption spectra, PL spectra, the schematic diagram of *XY* mode used for cross-section PL mapping, the photos of PL mapping original data, the cross-section SEM image, XRD patterns, GIWAXS patterns, PL spectra, UPS spectra, XPS spectra, photovoltaic parameter distribution of the device, and the cross-section SEM image (PDF)

## AUTHOR INFORMATION

**Corresponding Authors**
*E-mail: qic@bit.edu.cn (Q.C.).
*E-mail: mse.ybai@bit.edu.cn (Y.B.).

**ORCID ●**
Haipeng Xie: 0000-0002-1220-4778
Huanping Zhou: 0000-0002-0070-5540
Qi Chen: 0000-0002-9647-5873

**Author Contributions**
‖N.L. and P.L. contributed equally to this work.

**Notes**
The authors declare no competing financial interest.

## REFERENCES

(1) Wilson, G.; Mooney, D. *Research Cell Efficiency Records*; National Center for Photovoltaics: 2012.
(2) Burschka, J.; Pellet, N.; Moon, S.-J.; Humphry-Baker, R.; Gao, P.; Nazeeruddin, M. K.; Grätzel, M. Sequential Deposition as a Route to High-performance Perovskite-sensitized Solar Cells. *Nature* **2013**, *499*, 316−319.
(3) Kojima, A.; Teshima, K.; Shirai, Y.; Miyasaka, T. Organometal Halide Perovskites as Visible-light Sensitizers for Photovoltaic Cells. *J. Am. Chem. Soc.* **2009**, *131*, 6050−6051.
(4) Zhou, H.; Chen, Q.; Li, G.; Luo, S.; Song, T.-b.; Duan, H.-S.; Hong, Z.; You, J.; Liu, Y.; Yang, Y. Interface Engineering of Highly Efficient Perovskite Solar Cells. *Science* **2014**, *345*, 542−546.
(5) Dong, Q.; Fang, Y.; Shao, Y.; Mulligan, P.; Qiu, J.; Cao, L.; Huang, J. Electron-hole Diffusion Lengths > 175 mum in Solution-grown $CH_3NH_3PbI_3$ Single Crystals. *Science* **2015**, *347*, 967−970.
(6) Jeon, N. J.; Noh, J. H.; Kim, Y. C.; Yang, W. S.; Ryu, S.; Seok, S. I. Solvent Engineering for High-performance Inorganic−organic Hybrid Perovskite Solar Cells. *Nat. Mater.* **2014**, *13*, 897−903.
(7) Yin, G.; Zhao, H.; Jiang, H.; Yuan, S.; Niu, T.; Zhao, K.; Liu, Z.; Liu, S. F. Precursor Engineering for All-Inorganic $CsPbI_2Br$ Perovskite Solar Cells with 14.78% Efficiency. *Adv. Funct. Mater.* **2018**, *28*, 1803269.

(8) Leijtens, T.; Eperon, G. E.; Noel, N. K.; Habisreutinger, S. N.; Petrozza, A.; Snaith, H. J. Stability of Metal Halide Perovskite Solar Cells. *Adv. Energy Mater.* **2015**, *5*, 1500963.

(9) Lee, J. W.; Kim, D. H.; Kim, H. S.; Seo, S. W.; Cho, S. M.; Park, N. G. Formamidinium and Cesium Hybridization for Photo-and Moisture-stable Perovskite Solar Cell. *Adv. Energy Mater.* **2015**, *5*, 1501310.

(10) Shao, Y.; Fang, Y.; Li, T.; Wang, Q.; Dong, Q.; Deng, Y.; Yuan, Y.; Wei, H.; Wang, M.; Gruverman, A.; Shield, J.; Huang, J. Grain Boundary Dominated Ion Migration in Polycrystalline Organic–inorganic Halide Perovskite Films. *Energy Environ. Sci.* **2016**, *9*, 1752–1759.

(11) Li, Y.; Xu, X.; Wang, C.; Ecker, B.; Yang, J.; Huang, J.; Gao, Y. Light-Induced Degradation of $CH_3NH_3PbI_3$ Hybrid Perovskite Thin Film. *J. Phys. Chem. C* **2017**, *121*, 3904–3910.

(12) Yang, J.; Siempelkamp, B. D.; Liu, D.; Kelly, T. L. Investigation of $CH_3NH_3PbI_3$ Degradation Rates and Mechanisms in Controlled Humidity Environments Using in Situ Techniques. *ACS Nano* **2015**, *9*, 1955–1963.

(13) Han, G. S.; Yoo, J. S.; Yu, F.; Duff, M. L.; Kang, B. K.; Lee, J.-K. Highly Stable Perovskite Solar Cells in Humid and Hot Environment. *J. Mater. Chem. A* **2017**, *5*, 14733–14740.

(14) Hashmi, S. G.; Martineau, D.; Dar, M. I.; Myllymäki, T. T. T.; Sarikka, T.; Ulla, V.; Zakeeruddin, S. M.; Grätzel, M. High Performance Carbon-based Printed Perovskite Solar Cells with Humidity Assisted Thermal Treatment. *J. Mater. Chem. A* **2017**, *5*, 12060–12067.

(15) Smith, I. C.; Hoke, E. T.; Solis-Ibarra, D.; McGehee, M. D.; Karunadasa, H. I. A Layered Hybrid Perovskite Solar-cell Absorber with Enhanced Moisture Stability. *Angew. Chem., Int. Ed.* **2014**, *53*, 11232–11235.

(16) Zhou, J.; Chu, Y.; Huang, J. Photodetectors Based on Two-Dimensional Layer-Structured Hybrid Lead Iodide Perovskite Semiconductors. *ACS Appl. Mater. Interfaces* **2016**, *8*, 25660–25666.

(17) Tsai, H.; Nie, W.; Blancon, J.-C.; Stoumpos, C. C.; Asadpour, R.; Harutyunyan, B.; Neukirch, A. J.; Verduzco, R.; Crochet, J. J.; Tretiak, S.; Pedesseau, L.; Even, J.; Alam, M. A.; Gupta, G.; Lou, J.; Ajayan, P. M.; Bedzyk, M. J.; Kanatzidis, M. G.; Mohite, A. D. High-efficiency Two-dimensional Ruddlesden–Popper Perovskite Solar Cells. *Nature* **2016**, *536*, 312–316.

(18) Yuan, M.; Quan, L. N.; Comin, R.; Walters, G.; Sabatini, R.; Voznyy, O.; Hoogland, S.; Zhao, Y.; Beauregard, E. M.; Kanjanaboos, P.; Lu, Z.; Kim, D. H.; Sargent, E. H. Perovskite Energy Funnels for Efficient Light-emitting Diodes. *Nat. Nanotechnol.* **2016**, *11*, 872–877.

(19) Wang, Z.; Lin, Q.; Chmiel, F. P.; Sakai, N.; Herz, L. M.; Snaith, H. J. Efficient Ambient-air-stable Solar Cells with 2D–3D Heterostructured Butylammonium-caesium-formamidinium Lead Halide Perovskites. *Nat. Energy* **2017**, *2*, 17135.

(20) Cohen, B.-E.; Wierzbowska, M.; Etgar, L. High Efficiency and High Open Circuit Voltage in Quasi 2D Perovskite Based Solar Cells. *Adv. Funct. Mater.* **2017**, *27*, 1604733.

(21) Shang, Y.; Li, G.; Liu, W.; Ning, Z. Quasi-2D Inorganic CsPbBr3Perovskite for Efficient and Stable Light-Emitting Diodes. *Adv. Funct. Mater.* **2018**, 1801193.

(22) Lin, Y.; Bai, Y.; Fang, Y.; Chen, Z.; Yang, S.; Zheng, X.; Tang, S.; Liu, Y.; Zhao, J.; Huang, J. Enhanced Thermal Stability in Perovskite Solar Cells by Assembling 2D/3D Stacking Structures. *J. Phys. Chem. Lett.* **2018**, *9*, 654–658.

(23) Li, M.-H.; Yeh, H.-H.; Chiang, Y.-H.; Jeng, U.-S.; Su, C.-J.; Shiu, H.-W.; Hsu, Y.-J.; Kosugi, N.; Ohigashi, T.; Chen, Y.-A.; Shen, P.-S.; Chen, P.; Guo, T.-F. Highly Efficient 2D/3D Hybrid Perovskite Solar Cells via Low-Pressure Vapor-Assisted Solution Process. *Adv. Mater.* **2018**, *30*, 1801401.

(24) Shang, M.-H.; Zhang, J.; Zhang, P.; Yang, Z.; Zheng, J.; Haque, M. A.; Yang, W.; Wei, S.-H.; Wu, T. Stable Bandgap-Tunable Hybrid Perovskites with Alloyed Pb-Ba Cations for High-Performance Photovoltaic Applications. *J. Phys. Chem. Lett.* **2019**, *10*, 59–66.

(25) Grancini, G.; Roldán-Carmona, C.; Zimmermann, I.; Mosconi, E.; Lee, X.; Martineau, D.; Narbey, S.; Oswald, F.; De Angelis, F.; Graetzel, M.; Nazeeruddin, M. K. One-year Stable Perovskite Solar Cells by 2D/3D Interface Engineering. *Nat. Commun.* **2017**, *8*, 15684.

(26) Cao, D. H.; Stoumpos, C. C.; Farha, O. K.; Hupp, J. T.; Kanatzidis, M. G. 2D Homologous Perovskites as Light-Absorbing Materials for Solar Cell Applications. *J. Am. Chem. Soc.* **2015**, *137*, 7843–7850.

(27) Stoumpos, C. C.; Cao, D. H.; Clark, D. J.; Young, J.; Rondinelli, J. M.; Jang, J. I.; Hupp, J. T.; Kanatzidis, M. G. Ruddlesden–Popper Hybrid Lead Iodide Perovskite 2D Homologous Semiconductors. *Chem. Mater.* **2016**, *28*, 2852–2867.

(28) Wang, N.; Cheng, L.; Ge, R.; Zhang, S.; Miao, Y.; Zou, W.; Yi, C.; Sun, Y.; Cao, Y.; Yang, R.; Wei, Y.; Guo, Q.; Ke, Y.; Yu, M.; Jin, Y.; Liu, Y.; Ding, Q.; Di, D.; Yang, L.; Xing, G.; Tian, H.; Jin, C.; Gao, F.; Friend, R. H.; Wang, J.; Huang, W. Perovskite Light-emitting Diodes Based on Solution-processed Self-organized Multiple Quantum Wells. *Nat. Photonics* **2016**, *10*, 699–704.

(29) Liu, J.; Leng, J.; Wu, K.; Zhang, J.; Jin, S. Observation of Internal Photoinduced Electron and Hole Separation in Hybrid Two-Dimensional Perovskite Films. *J. Am. Chem. Soc.* **2017**, *139*, 1432–1435.

(30) Zhou, N.; Shen, Y.; Li, L.; Tan, S.; Liu, N.; Zheng, G.; Chen, Q.; Zhou, H. Exploration of Crystallization Kinetics in Quasi Two-Dimensional Perovskite and High Performance Solar Cells. *J. Am. Chem. Soc.* **2015**, *140*, 459–465.

(31) Adinolfi, V.; Yuan, M.; Comin, R.; Thibau, E. S.; Shi, D.; Saidaminov, M. I.; Kanjanaboos, P.; Kopilovic, D.; Hoogland, S.; Lu, Z.-H.; Bakr, O. M.; Sargent, E. H. The In-Gap Electronic State Spectrum of Methylammonium Lead Iodide Single-Crystal Perovskites. *Adv. Mater.* **2016**, *28*, 3406–3410.

Letter

# Understanding the Defect Properties of Quasi-2D Halide Perovskites for Photovoltaic Applications

Na Liu, Pengfei Liu, Huanping Zhou, Yang Bai,* and Qi Chen*

Read Online

ACCESS | Metrics & More | Article Recommendations | SI Supporting Information

**ABSTRACT:** Quasi-2D halide perovskites have emerged as some of the most promising photovoltaic materials owing to their excellent stability, yet the device power conversion efficiency is far from satisfactory. Besides crystal orientation-related carrier transport, defects in absorbers also play a crucial role in device performance, which has received limited attention in the 2D perovskite field. Herein, we systematically profile the defect states in 2D perovskite film by the temperature-dependent admittance spectroscopy (AS), light intensity-dependent $V_{OC}$, space-charge-limited-circuit (SCLC), and photoluminescence measurements. It is revealed that the quasi-2D perovskite films suffer from severe defects as compared to the 3D counterparts in terms of both trap energy levels and trap densities. Consequently, the level of nonradiative recombination of photogenerated carriers is much greater in the corresponding devices, wherein the monomolecular recombination is dominant. These findings substantially contribute to a deeper understanding of the nature of 2D perovskite materials, which promotes the further development of 2D perovskite solar cells.
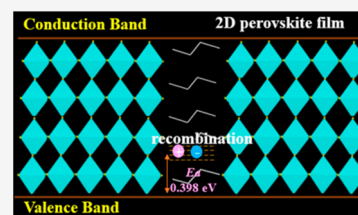
Organic—inorganic metal halide perovskites have emerged as some of the most promising next-generation photovoltaic materials due to their outstanding properties, such as their tunable band gaps, long electron—hole diffusion lengths, low recombination rates, and low fabrication temperatures, which provide hope for both high efficiency and ultralow fabrication cost.[1−4] The perovskite-based solar cell efficiency has already reached a certified value of 25.2%, which is competitive with that of the mainstream multicrystalline silicon.[5] Three-dimensional (3D) perovskite materials are prone to degradation after exposure to moisture and light. Developing an all-inorganic perovskite is a promising strategy for solving the thermal instability problem of 3D perovskites, and the highest power conversion efficiency (PCE) has rapidly increased to >16%.[6−9] Meanwhile, two-dimensional (2D) perovskite, owing to its encouraging stability in high-moisture and continuous lighting conditions, has been recognized as a promising strategy for perovskite solar cell development.[10] 2D perovskite can be structurally derived from the 3D analogue upon "cutting" the compound along a specific crystallographic plane. Depending on the cutting site in the 3D framework, the 2D perovskites can be subcategorized as ⟨100⟩-, ⟨110⟩-, and ⟨111⟩-oriented perovskites. The Ruddlesden—Popper (RP),[11] Dion—Jacobson (DJ),[12] Aurivillius (AV), and alternating cations in the interlayer space (ACI)[13] configurations are four structural configurations of the ⟨110⟩ perovskites; among them, the RP perovskites are by far the most developed structural type.[14]

2D RP perovskites have a generic chemical formula of $(A1)_2(A2)_{n−1}M_nX_{3n+1}$. A1 long-chain organic amine ions, such as $C_6H_5(CH_2)_2NH_3^+$ (PEA$^+$) and $CH_3CH_2CH_2CH_2NH_3^+$ (BA$^+$), act as a spacer between the perovskite frameworks

formed by the A (MA$^+$, FA$^+$, or Cs$^+$) and M (Pb$^{2+}$ or Sn$^{2+}$) cations and X halide anions. The value of the layer number ($n$) of the perovskite frameworks can be controlled by adjusting the ratio between the spacer cation (A1) and the small organic cation (A2).[11] The corresponding crystal structure and optical characterization of 2D $BA_2MA_{n−1}Pb_nI_{3n+1}$ ($n$ = 1, 2, 3, or 4) have been described.[11] Recently, the $BA_2MA_3Pb_4I_{13}$ compounds ($n$ = 4) are widely used for 2D perovskite solar cell studies due to their good stability combined with their promising photoelectric properties. Perovskite solar cells based on 2D structural compounds have exhibited a relatively low efficiency because of the inhibition of out-of-plane charge transport by the insulating spacer cations.[10] Although the development of new fabrication techniques has encouraged the improvement in the PCE,[14] the PCE of the 2D perovskite device is still much lower than that of the 3D device. Recent works involving 2D perovskite device have been focused on the component control,[15,16] the crystallization kinetics of the 2D perovskite films,[16,17] and the internal electron—hole separation.[18] The defects in grain boundaries and interfaces, as carrier recombination centers, strongly influence the device performance, and a series of works have been performed on defect analysis in 3D perovskite.[2] In most cases, point defects in the bulk of perovskite lead to the shallow level defects owing
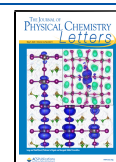
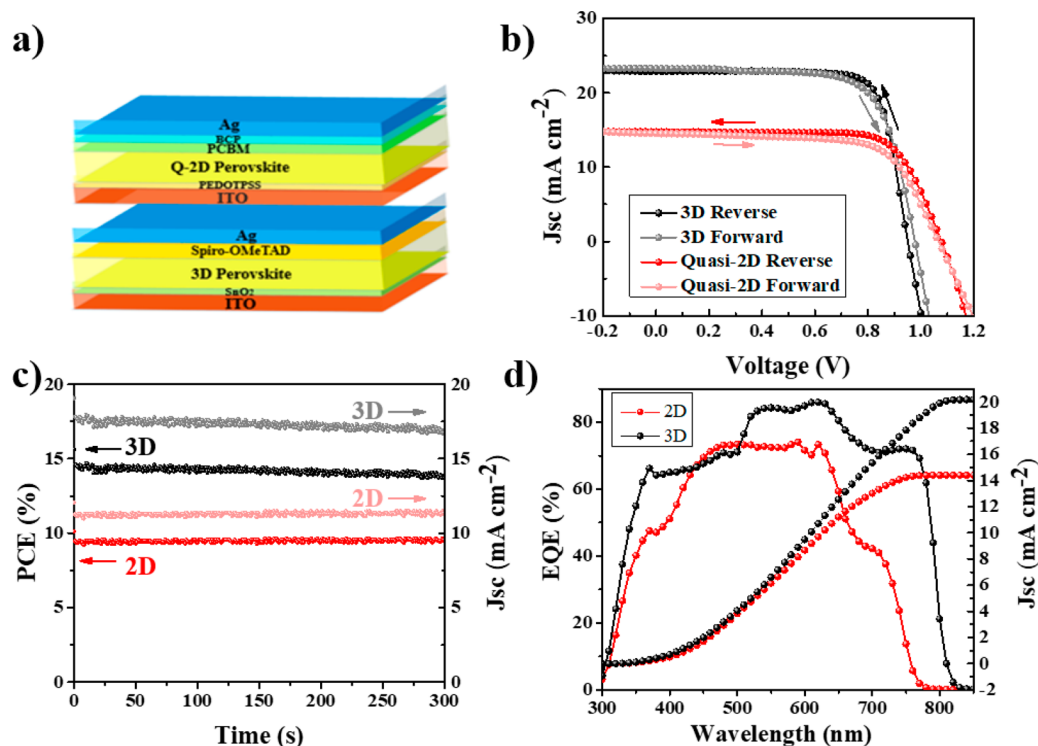**Figure 1.** (a) Device structure of 2D ($BA_2MA_3Pb_4I_{13}$) and 3D ($MAPbI_3$) perovskite solar cells. (b) $J−V$ characteristics under simulated AM 1.5G irradiation (100 mW/cm$^2$) for 2D and 3D perovskite solar cells. (c) Stabilized photocurrent at the voltage of maximum power point of 2D and 3D perovskite solar cells. (d) External quantum efficiency (EQE) and corresponding integrated short-circuit current density ($J_{SC}$) of 2D and 3D perovskite solar cells.

to the lower formation energy.[19] While the structural defects at the grain boundary and film surface could induce deep level defects, the trapped carrier hardly escapes from it, resulting in a reduced PCE.[20−22] Previous literature has reported many strategies for passivating defects, including interface, compositional engineering, grain orientation tuning, etc.[23−25] However, the corresponding study is still limited in 2D perovskite. Accurate characterization of the defect nature in 2D perovskite material is crucial for understanding the associated optoelectronic properties of these materials, which is essential for the development of device design strategy.

Here, by using EIS, AS, TRPL, and SCLC technologies, we investigate the defect properties and carrier recombination dynamics of the $BA_2MA_3Pb_4I_{13}$ perovskite film and device. For the first time, the AS technology is applied to calculate the energy level of defects in 2D perovskite, and we find that the defects in 2D perovskite are mainly deep level defects with an $E_a$ of 0.398 eV, which is much higher than that of 3D perovskite (0.075 eV). In addition, the electron and hole trap densities are measured to be $6.82 \times 10^{16}$ and $8.22 \times 10^{16}$ cm$^{-3}$, respectively, which are 2 orders of magnitude higher than that of 3D perovskite. Furthermore, the recombination process is characterized by the light intensity-dependent $V_{OC}$ that identifies the increased defect-assisted recombination process in the 2D perovskite devices.

First, the device performance of typical 3D $MAPbI_3$ perovskite solar cells and 2D $BA_2MA_3Pb_4I_{13}$ ($n = 4$) perovskite solar cells is compared, and the structures of 3D and 2D devices used in this study are based on ITO/SnO$_2$/MAPbI$_3$/Spiro/Ag and ITO/PEDOT:PSS/BA$_2$MA$_3$Pb$_4$I$_{13}$/PCBM/BCP/Ag structures, respectively, which are shown in Figure 1a. The photoactive layers of 2D and 3D perovskite film are

prepared by the one-step spin-coating method; the details of device fabrication are described in the experimental section, and the corresponding SEM images and X-ray diffraction patterns are shown in Figures S1−S3. Figure 1b shows the current density−voltage ($J−V$) characteristics of corresponding devices measured under simulated sunlight with AM 1.5 at a high relative humidity (RH) of 60% and 25 °C, and the full performance parameters are presented in Table S1. The 2D perovskite device exhibits a short-circuit current ($J_{SC}$) of 14.53 mA cm$^{-2}$, a fill factor (FF) of 67.61%, and an open-circuit voltage ($V_{OC}$) of 1.07 V, yielding a PCE of 10.48%. The 3D device shows a PCE of 14.80%, with a $J_{SC}$ of 22.57 mA cm$^{-2}$, a $V_{OC}$ of 0.97 V, and a FF of 67.61%. Figure 1c shows that the stabilized PCEs of 9.7% and 14.6% are achieved by holding the voltage at the maximum power point for 2D and 3D perovskite solar cells, respectively. In addition, the $J_{SC}$ values obtained from the $J−V$ characteristics match well with the external quantum efficiency (EQE) obtained by the integration of the spectral response, which are shown in Figure 1d. The value of $J_{SC}$ is determined by many factors, such as light capture, carrier generation, charge transfer, and electrode charge collection. The weak light capture of 2D perovskite resulted from its smaller light absorption coefficient, which is highly related to the composition, and its larger band gap narrows the light absorption range. Besides that, the defects in the perovskite film also have a strong influence on the charge transfer and collection.

To investigate the defect behavior in 2D perovskite, systematical studies are used and compared with 3D perovskite. Accurate characterization of the charge trap density in perovskite material is a crucial step toward understanding the associated optoelectronic properties. To understand the
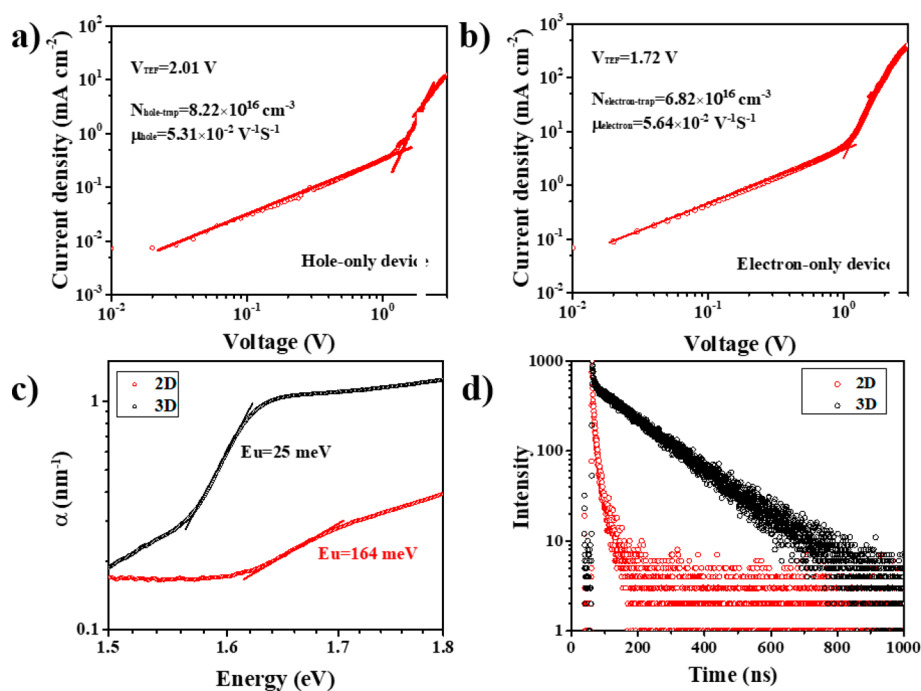
**Figure 2.** Current density−voltage characteristics of (a) hole- and (b) electron-only devices for estimating defect density in a 2D perovskite film. (c) Ultraviolet absorption and (d) time-resolved photoluminescence decay for 2D and 3D perovskite films.

charge trap density and carrier mobility in 2D perovskite films, we performed the space-charge-limited-current (SCLC) method.[2] Panels a and b of Figure 2 show the current density−voltage (J−V) curves of electron-only and hole-only devices. The electron and hole trap density are calculated according to eq 1:

$$N_{trap} = 2 \varepsilon \varepsilon_0 V_{TFL} / eL^2 \tag{1}$$

where $N_{trap}$ is the defect density, $\varepsilon$ is the static permittivity of perovskite, $\varepsilon_0$ is the permittivity of free space, $e$ is the elementary charge, and $L$ is the thickness of the perovskite film. The hole and electron trap densities in 2D perovskite films are calculated to be $8.22 \times 10^{16}$ and $6.82 \times 10^{16}$ cm$^{-3}$, respectively, while the value is significantly higher than that in 3D perovskite films ($4.12 \times 10^{15}$ and $3.22 \times 10^{15}$ cm$^{-3}$, respectively) reported from previous research,[2] indicating that more severe carrier recombination could occur in 2D perovskite films. By fitting J−V curves at the SCLC region, the hole and electron mobility of 2D perovskite films are estimated to be $5.31 \times 10^{-2}$ and $5.64 \times 10^{-2}$ cm$^2$ V$^{-1}$ s$^{-1}$, respectively, which are considerably lower than that of the 3D perovskite film, indicating the introduction of long-chain butylamine as a spacer leads to a decrease in carrier mobility and impedes carrier transmission.

In addition, the ultraviolet−visible (UV) absorption and time-resolved PL (TRPL) decay measurements are applied to study the defect properties. The samples used for the study are all prepared by depositing 2D and 3D perovskite films on glass substrates, and the corresponding UV and TRPL spectra are shown in panels c and d of Figure 2, respectively. The Urbach energies that carry the defect information from the UV band tails are calculated, and the value of the 2D perovskite film is 164 meV, which is 6 times higher than that of 3D perovskite film (25 meV). Two time components are obtained from TRPL curves to evaluate the carrier recombination lifetime via a biexponential function of time [$F(t) = A_1^{-t/\tau_1} + A_2^{-t/\tau_2} + y_0$],

where $\tau_1$ and $\tau_2$ represent the time of the fast and slow decay processes, respectively. The fast decay component is attributed to the film surface recombination, while the slow decay component is associated with the recombination occurred in the bulk. All of the fitted TRPL parameters for 2D and 3D perovskite films are summarized in Table 1. The photocarrier

**Table 1. Lifetimes Derived from TRPL Decay**

|  | 2D perovskite | 3D perovskite |
| --- | --- | --- |
| $\tau_1$ (ns) | 19.81 | 5.21 |
| $\tau_2$ (ns) | 3.84 | 155.12 |

lifetimes of the bulk of 2D and 3D perovskites are estimated to be 3.84 and 155.12 ns, respectively, indicating a severe bulk recombination in 2D perovskite. The steady state PL spectra of 2D and 3D perovskite films are shown in Figure S4 for reference.

To gain deep insights into charge transport and recombination in a 2D perovskite device, impedance spectra are measured at room temperature in the dark at an applied bias of 0 V. The impedance spectra were recorded over the frequency range from 1 Hz to 1 MHz under an AC of 20 mV. Panels a and b of Figure 3 present the experimental Bode and Nyquist plots for 2D and 3D perovskite devices, respectively. The Bode plot reveals that the equivalent circuit is 2RC elements in series, which is shown in the inset of Figure 3b. A series resistance $R_s$ represents the resistance offered by ITO, connecting wires and gold contacts. The high-frequency spectrum from the impedance of perovskite material is assigned to $R_{HF}$. The $R_{HF}$ impedance element refers to the selective contacts or their interfaces with the absorber layer, which can be diverted from the fitted spectra. In addition, a constant phase element $CPE_{HF}$ is used instead of pure capacitance. Finally, the low-frequency spectrum from the impedance of perovskite material is assigned to $R_{LF}$, which is a
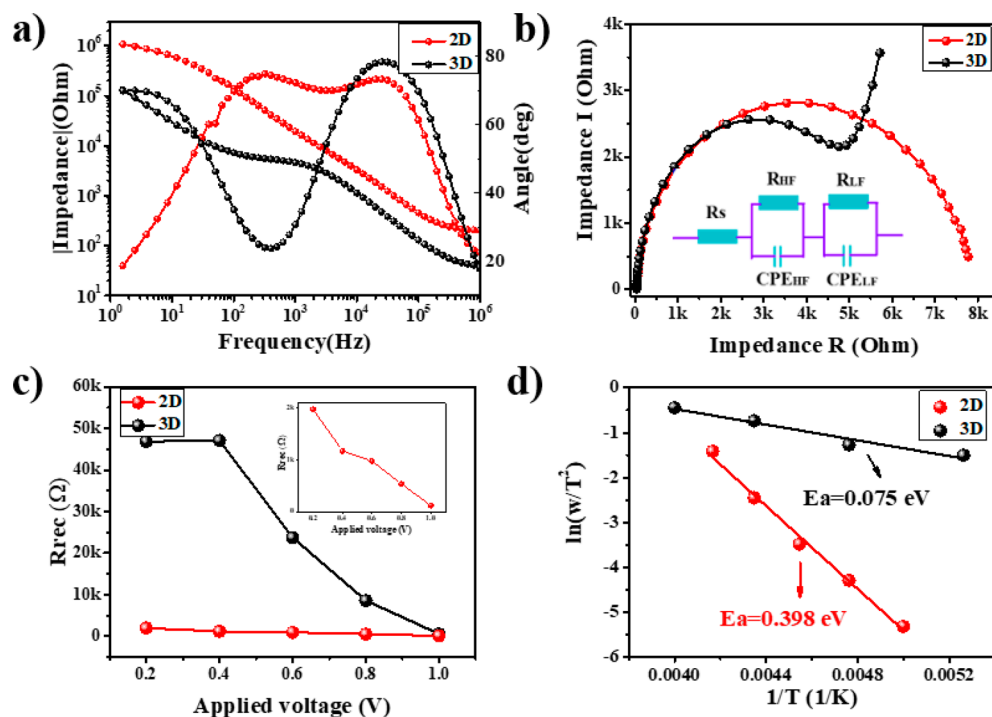
**Figure 3.** (a) Bode and (b) Nyquist spectra from electrochemical impedance spectroscopy (EIS) measured under open-circuit conditions for 2D and 3D perovskite devices. (c) Recombination resistance spectra of 2D and 3D perovskite device extracted from the EIS curve. (d) Energy level of trap states in 2D and 3D perovskite solar cells.

combination of recombination resistance and chemical capacitance in parallel.[26] Clearly, in the Bode plots, the spectra in the high-frequency range are similar, while the intermediate- and low-frequency ranges show huge differences. As the low-frequency range spectra are more related to the recombination resistance, recombination in the 2D device may become more serious as a faster process. The $R_{HF}$ values for 2D and 3D perovskite solar cells are diverted to be 7605 and 5550 Ω, respectively, which are similar as expected. Meanwhile, the recombination resistance of 2D and 3D perovskite solar cells is calculated from the EIS spectra tested under various conditions and is presented in Figure 3c. Obviously, the recombination resistance of 2D perovskite is much lower than that of its 3D counterpart under all test conditions, indicating that serious carrier recombination occurs in 2D perovskite.

To further clearly reveal the energy level of the trap state in the perovskite solar cells, temperature-dependent admittance spectroscopy of 2D and 3D perovskite devices was performed. The specific test methods and parameters are the same as in previous studies.[1,27] As reported, for a p-type perovskite semiconductor, the defect activation energy ($E_a$) is approximately the depth of the trap state energy level relative to the VBM of the perovskite ($E_a = E_T - E_{VBM}$), which means that if a charge is trapped with a smaller value of $E_a$, it could escape easily. The $E_a$ and the characteristic transition angular frequency ($\omega_0$) can be expressed in eq 2:

$$\omega_0 = \beta T^2 \exp\left(-\frac{E_a}{k_B T}\right) \tag{2}$$

where $\beta$ is a temperature-dependent parameter, $T$ is the temperature, and $k_B$ is Boltzmann's constant. The value of $E_a$ can be obtained from eq 3:

$$\ln\left(\frac{\omega_0}{T^2}\right) = \ln \beta - \frac{E_a}{k_B T} \tag{3}$$

and the corresponding plots are shown in Figure 3d. The value of $E_a$ can be obtained from the slope of the fitted curve.

The $E_a$ values of 2D and 3D perovskite solar cells are calculated to be 0.398 and 0.075 eV, respectively. It is obviously that the 2D perovskite device energy level of defects is relatively deeper than that of 3D perovskite; thus, the electron and hole trapped in the defects are hard to escape but recombine.

In the following, the distribution of trap state density in the perovskite solar cells is investigated via admittance spectroscopy.[28,29] The distribution of the trap state density can be derived from the following equations:

$$N_T(E_\omega) = -\frac{V_{bi}}{qW} \frac{dC}{d\omega} \frac{\omega}{k_B T} \tag{4}$$

$$E_\omega = k_B T \ln\left(\frac{\beta T^2}{\omega}\right) \tag{5}$$

where $V_{bi}$ is the built-in potential, $W$ is the depletion width, $q$ is the elementary charge, $C$ is the capacitance, and $\omega$ is the applied angular frequency. To estimate the built-in potential ($V_{bi}$) and the apparent doping profile in the depleted layer ($N$) of the devices, the Mott−Schottky measurement is applied at a frequency of 1 kHz with potentials ranging from 0 to 1.2 V. According to the depletion approximation, $C$, $V_{bi}$, and $W$ at the junction can be expressed in the relations

$$\frac{C}{A} = \frac{\varepsilon\varepsilon_0}{W} = \sqrt{\frac{q\varepsilon\varepsilon_0 N}{2(V_{bi} - V)}} \tag{6}$$
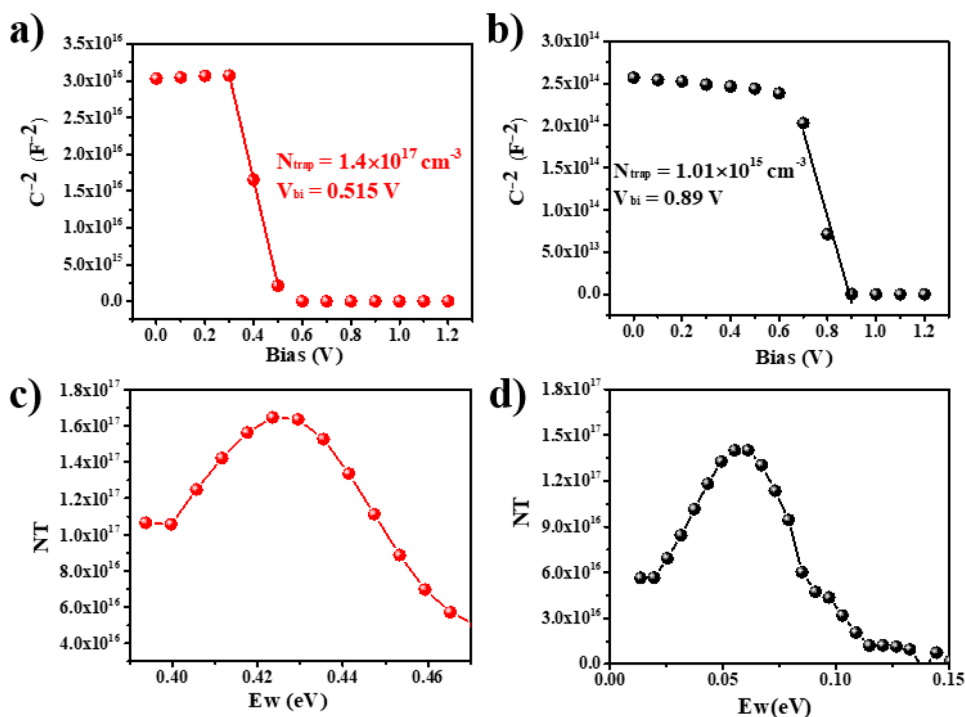
**Figure 4.** Mott−Schottky analysis at 1 kHz for (a) 2D and (b) 3D perovskite solar cells. Trap state density ($N_T$) of (c) 2D and (d) 3D perovskite devices.
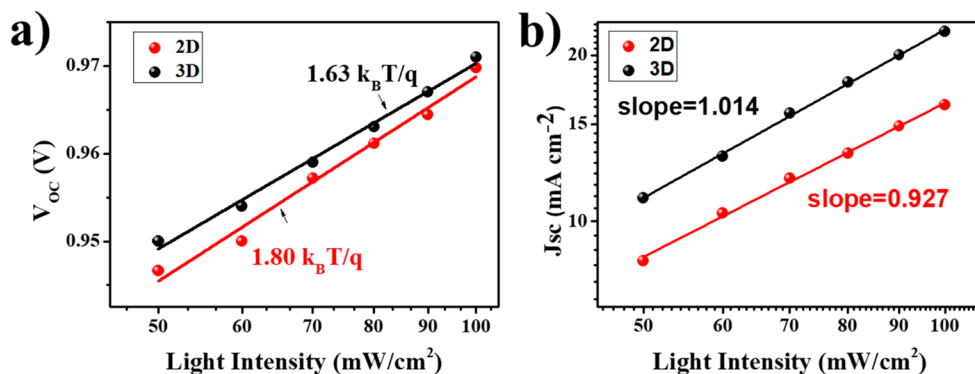


**Figure 5.** (a) Light intensity dependence of $V_{OC}$ and (b) $J_{SC}$ with the corresponding slopes obtained by linear fits for 2D (red line) and 3D (black line) perovskite devices, respectively.

$$\frac{A^2}{C^2} = \frac{2(V_{bi} - V)}{q\varepsilon\varepsilon_0 N} \tag{7}$$

The Mott−Schottky plots are shown in panels a and b of Figure 4; the intersection on the bias axis determines $V_{bi}$, and the slope gives the impurity doping density $N$. The $V_{bi}$ values of 3D and 2D perovskite solar cells are 0.89 and 0.515 V, respectively, and the $N_{trap}$ values of 3D and 2D devices are 1.01 × 10$^{15}$ and 1.4 × 10$^{17}$ cm$^{-3}$, respectively. The $V_{bi}$ value of the 3D perovskite device is higher than that of the 2D device, indicating that the 3D perovskite device is strong enough to extract the charge in the depletion region effectively, which may due to the continuous 3D framework without an insulator spacer. The higher $N_{trap}$ value of 2D devices also agrees with the results from TRPL and impedance measurements. Then, the distributions of trap state density in these devices are calculated and illustrated in panels c and d of Figure 4. It has been found that the trap state energy level of the 2D perovskite device is relatively deep (0.39 eV), which indicates that the

carriers would be easily captured by the traps and the trapped carriers are hard to escape; meanwhile, the trap state density of the 2D device is also slightly high compared with that of the 3D device.

Eventually, the carrier recombination processes in perovskite devices are studied by measuring $V_{OC}$ and $J_{SC}$ at various light intensities from 50 to 100 mW cm$^{-2}$.[30] The light intensity-dependent $V_{OC}$ can provide information about the recombination process. Under open-circuit conditions, the current is zero and all carriers recombine within the device. According to eq 8

$$V_{OC} = n(k_B T/e) \ln(I) + \text{constant} \tag{8}$$

where $n$ is the ideality factor, $k$ is the Boltzmann constant, $e$ is the elementary charge, $T$ is the absolute temperature, and $I$ is the light intensity. A plot of $V_{OC}$ as a function of the logarithmic light intensity $[\ln(I)]$ is linearly fitted to evaluate the slope, which usually represents the recombination process caused by trap states in the device. If the ideality factor is close

to 1, it means a bimolecular charge carrier recombination is the dominant recombination pathway in the device. On the contrary, the slope value close to 2 represents a trap-assisted charge recombination. As shown in Figure 5a, slope values of 1.80 and 1.63 $k_B T/e$ are obtained for the 2D and 3D perovskite devices, respectively. The 2D device has a larger slope of 1.80 $k_B T/e$, which implies that heavier trap-assisted Shockley−Read−Hall (SRH) recombination happens in the 2D device, indicating a higher defect density in the 2D perovskite device compared to the 3D perovskite device. Figure 5b shows the light intensity-dependent current density. On the basis of the common relation of $J_{SC} \propto I^\alpha$, the slope values $\alpha$ for 3D (1.014) and 2D (0.927) perovskite devices are derived. The $\alpha$ value of 2D perovskite is 0.927, indicating charge carrier losses are dominated by monomolecular recombination.[31] At the same time, the 3D devices are closer to the ideal case, suggesting a decrease in the dimension of the materials leads to an increase in the trap density in the perovskite materials. Combined with the results from light intensity-dependent $V_{OC}$, serious trap-assisted SRH recombination exists in the 2D perovskite device compared with 3D counterparts. The results are in good agreement with AS and SCLC measurements.

In conclusion, defect profiles in quasi-2D halide perovskite thin films were comprehensively depicted and compared with those of the 3D perovskites for the first time via a series of characterizations, including AS, SCLC, light intensity-dependent $V_{OC}$, and TRPL. The $E_a$ (0.398 eV) for defects in 2D perovskite is much greater than that of 3D perovskite (0.075 eV), indicating that the defects in 2D perovskite films are deep level defects; thus, the carrier traps hardly escape. Meanwhile, the electron and hole trap densities of 2D perovskite (6.82 × $10^{16}$ and 8.22 × $10^{16}$ cm$^{-3}$, respectively) are an order of magnitude higher than those of 3D perovskite (4.12 × $10^{15}$ and 3.22 × $10^{15}$ cm$^{-3}$, respectively), which is confirmed by SCLC and AS measurement. Furthermore, we found that the monomolecular recombination through a trap state or recombination center is dominant by characterizing $V_{OC}$ at various light intensities. It further aggravates the decrease in photovoltaic efficiency in the corresponding devices beyond the poor carrier transport due to crystal orientation. With the focus on the defects and carrier recombination in 2D perovskite, it sheds light on the nature of 2D perovskite materials applied in solar cells, emphasizing the decrease in the trap density and activation energy of defects is an effective strategy for improving the efficiency of 2D perovskite solar cells.

## EXPERIMENTAL METHODS

*Materials*. Poly(3,4-ethylenedioxythiophene):poly-(styrenesulfonate) (PEDOT:PSS) water dispersion (Clevios VP AI 4083) was acquired from Heraeus. Butylamine iodine (BAI), bathocuproine (BCP), Spiro-OMeTAD, and [6,6]-phenyl-C61-butyric acid methyl ester (PC61BM) were purchased from Xi'an baolaite Technology Ltd. Methylamine iodide (MAI) was prepared according to the reported procedure. Lead iodide (PbI$_2$, 99.999%), *N,N*-dimethylforma-mide (DMF, 99.99%), chlorobenzene (CB, 99.9%), 4-*tert*-butylpyridine (TBP, 99.9%), isopropanol (99.99%), and methyl alcohol (MA, 99.9%) were purchased from Sigma-Aldrich. Spiro-OMeTAD was purchased from Lumitech. All reagents were used as received without further purification.

*Device Fabrication*. (i) *2D Perovskite Solar Cell Fabrication*. The inverted planar heterojunction 2D perovskite solar cells were fabricated on ITO substrates. The indium tin oxide (ITO) substrates were successively cleaned using an ultra-sonicator in acetone, water, and isopropanol. After UV−O$_3$ treatment for 45 min, the PEDOT:PSS was spin coated on the substrate at 3000 rpm for 25 s and then annealed on a hot plate at 120 °C for 20 min. The perovskite precursor solution (100 mg of BAI, 119.25 mg of MAI, and 461 mg of PbI$_2$ dissolved in 1.25 mL of DMF) was spin coated on the ITO/PEDOT:PSS substrate at 70 °C and 2000 rpm for 25 s. After the annealing on a hot plate at 80 °C for 20 min, 30 $\mu$L of a PC$_{61}$BM (20 mg/mL in chlorobenzene) solution was then spin-coated on the top of the perovskite layer at 2000 rpm for 30 s and BCP (2.5 mg/mL in methanol) was dropped onto PC$_{61}$BM at a rotational speed of 6000 rpm to form an electron extracting layer, and the samples were annealed on a hot plate at 70 °C for 10 min. Finally, 100 nm Ag was deposited via thermal evaporation at a pressure of 1 × $10^{-4}$ Pa.

(ii) *3D Perovskite Solar Cell Fabrication*. The indium tin oxide (ITO) substrates were successively cleaned using an ultrasonicator in acetone, water, and isopropanol. After UV−O$_3$ treatment for 45 min, the SnO$_2$ film was spin coated on the substrate with the SnO$_2$ colloidal solution at 3000 rpm for 30 s and then annealed on a hot plate at 150 °C for 30 min. The perovskite precursor solution (159 mg of MAI and 461 mg of PbI$_2$ dissolved in 0.6 mL of DMF) was spin coated on the ITO/SnO$_2$ substrate at 4000 rpm for 25 s. After the annealing on a hot plate at 90 °C for 5 min, the hole-transport layer that contained 80 mg/mL Spiro-OMeTAD, 30 $\mu$L/mL *tert*-butylpyridine, and 35 $\mu$L/mL of bis(trifluoromethane)-sulfonimide lithium salt (260 mg/mL in acetonitrile) were spin coated at 3000 rpm for 30 s. Finally, 100 nm Ag was deposited via thermal evaporation under a pressure of 1 × $10^{-4}$ Pa.

*Characterization*. The current density−voltage characteristics of photovoltaic devices were obtained using a Keithley 2400 source measure unit. The photocurrent was measured under AM1.5 G illumination at 100 mW cm$^{-2}$ using a Newport Thermal Oriel 91192 1000 W solar simulator. The light intensity was calibrated using a KG-5 Si diode. The effective area of each cell was 0.102 cm$^2$ defined by masks for all of the photovoltaic devices discussed in this work. External quantum efficiencies (EQEs) were determined on a solar cell quantum efficiency measurement system (QER) provided by Enli Technology Co. UV−visible absorption spectra were recorded with a UV−visible spectrophotometer (Agilent 8453). Transient state photoluminescence (TRPL) was measured by using an FLS980 instrument (Edinburgh Instruments Ltd.) with excitation at 470 nm. Electrochemical impedance spectroscopy (EIS) measurements were performed by using an electrochemical workstation (Zahner Co.). EIS spectra were recorded at room temperature (25 °C) in the dark at different applied biases (0−1.2 V). The frequency range of 0.1−1 MHz with an AC perturbation signal of 20 mV was employed in all EIS measurements.

## ASSOCIATED CONTENT

**ⓢ Supporting Information**

The Supporting Information is available free of charge at https://pubs.acs.org/doi/10.1021/acs.jpclett.0c00772.

Top-view and cross-sectional SEM images, XRD patterns, PL measurements, and details of device performance (PDF)

## AUTHOR INFORMATION

### Corresponding Authors

**Qi Chen** − *School of Materials Science and Engineering, Beijing Institute of Technology, Beijing 100081, P. R. China;* orcid.org/0000-0002-9647-5873; Email: qic@bit.edu.cn

**Yang Bai** − *School of Materials Science and Engineering, Beijing Institute of Technology, Beijing 100081, P. R. China; Guangdong Provincial Key Lab of Nano-Micro Materials Research, School of Chemical Biology and Biotechnology, Peking University Shenzhen Graduate School, Shenzhen 518055, China;* Email: mse.ybai@bit.edu.cn

### Authors

**Na Liu** − *School of Materials Science and Engineering, Beijing Institute of Technology, Beijing 100081, P. R. China*

**Pengfei Liu** − *School of Materials Science and Engineering, Beijing Institute of Technology, Beijing 100081, P. R. China*

**Huanping Zhou** − *Beijing Key Laboratory for Theory and Technology of Advanced Battery Materials, Department of Materials Science and Engineering, Department of Energy and Resources Engineering, College of Engineering, Peking University, Beijing 100871, P. R. China;* orcid.org/0000-0002-0070-5540

Complete contact information is available at:
https://pubs.acs.org/10.1021/acs.jpclett.0c00772

### Notes

The authors declare no competing financial interest.

## REFERENCES

(1) Green, M. A.; Ho-Baillie, A.; Snaith, H. J. The Emergence of Perovskite Solar Cells. *Nat. Photonics* **2014**, *8*, 506−514.

(2) Dong, Q.; Fang, Y.; Shao, Y.; Mulligan, P.; Qiu, J.; Cao, L.; Huang, J. Solar Cells. Electron-Hole Diffusion Lengths > 175 Mum in Solution-Grown Ch3nh3pbi3 Single Crystals. *Science* **2015**, *347*, 967−70.

(3) Lee, M. M.; Teuscher, J.; Miyasaka, T.; Murakami, T. N.; Snaith, H. J. Efficient Hybrid Solar Cells Based on Meso-Superstructured Organometal Halide Perovskites. *Science* **2012**, *338*, 643.

(4) Zhou, H.; Chen, Q.; Li, G.; Luo, S.; Song, T.-b.; Duan, H.-S.; Hong, Z.; You, J.; Liu, Y.; Yang, Y. Interface Engineering of Highly Efficient Perovskite Solar Cells. *Science* **2014**, *345*, 542−546.

(5) NREL. Research Cell Efficiency Records.

(6) Liang, J.; et al. All-Inorganic Perovskite Solar Cells. *J. Am. Chem. Soc.* **2016**, *138*, 15829−15832.

(7) Yuan, S.; Qian, F.; Yang, S.; Cai, Y.; Wang, Q.; Sun, J.; Liu, Z.; Liu, S. F. Nbf5: A Novel A-Phase Stabilizer for Fa-Based Perovskite Solar Cells with High Efficiency. *Adv. Funct. Mater.* **2019**, *29*, 1807850.

(8) Han, Y.; Zhao, H.; Duan, C.; Yang, S.; Yang, Z.; Liu, Z.; Liu, S. F. Controlled N-Doping in Air-Stable Cspbi2br Perovskite Solar Cells with a Record Efficiency of 16.79%. *Adv. Funct. Mater.* **2020**, *30*, 1909972.

(9) Zhao, H.; Han, Y.; Xu, Z.; Duan, C.; Yang, S.; Yuan, S.; Yang, Z.; Liu, Z.; Liu, S. F. A Novel Anion Doping for Stable Cspbi2br Perovskite Solar Cells with an Efficiency of 15.56% and an Open Circuit Voltage of 1.30 V. *Adv. Energy Mater.* **2019**, *9*, 1902279.

(10) Smith, I. C.; Hoke, E. T.; Solis-Ibarra, D.; McGehee, M. D.; Karunadasa, H. I. A Layered Hybrid Perovskite Solar-Cell Absorber with Enhanced Moisture Stability. *Angew. Chem., Int. Ed.* **2014**, *53*, 11232−5.

(11) Stoumpos, C. C.; Cao, D. H.; Clark, D. J.; Young, J.; Rondinelli, J. M.; Jang, J. I.; Hupp, J. T.; Kanatzidis, M. G. Ruddlesden−Popper Hybrid Lead Iodide Perovskite 2d Homologous Semiconductors. *Chem. Mater.* **2016**, *28*, 2852−2867.

(12) Mao, L.; Ke, W.; Pedesseau, L.; Wu, Y.; Katan, C.; Even, J.; Wasielewski, M. R.; Stoumpos, C. C.; Kanatzidis, M. G. Hybrid Dion-Jacobson 2d Lead Iodide Perovskites. *J. Am. Chem. Soc.* **2018**, *140*, 3775−3783.

(13) Soe, C. M. M.; et al. New Type of 2d Perovskites with Alternating Cations in the Interlayer Space, (C(Nh2)3)(Ch3nh3)-Npbni3n+1: Structure, Properties, and Photovoltaic Performance. *J. Am. Chem. Soc.* **2017**, *139*, 16297−16309.

(14) Tsai, H.; et al. High-Efficiency Two-Dimensional Ruddlesden−Popper Perovskite Solar Cells. *Nature* **2016**, *536*, 312−316.

(15) Zhang, X.; et al. Stable High Efficiency Two-Dimensional Perovskite Solar Cells Via Cesium Doping. *Energy Environ. Sci.* **2017**, *10*, 2095−2102.

(16) Zhou, N.; Shen, Y.; Li, L.; Tan, S.; Liu, N.; Zheng, G.; Chen, Q.; Zhou, H. Exploration of Crystallization Kinetics in Quasi Two-Dimensional Perovskite and High Performance Solar Cells. *J. Am. Chem. Soc.* **2018**, *140*, 459−465.

(17) Chen, A. Z.; Shiu, M.; Ma, J. H.; Alpert, M. R.; Zhang, D.; Foley, B. J.; Smilgies, D. M.; Lee, S. H.; Choi, J. J. Origin of Vertical Orientation in Two-Dimensional Metal Halide Perovskites and Its Effect on Photovoltaic Performance. *Nat. Commun.* **2018**, *9*, 1336.

(18) Liu, J.; Leng, J.; Wu, K.; Zhang, J.; Jin, S. Observation of Internal Photoinduced Electron and Hole Separation in Hybrid Two-Dimentional Perovskite Films. *J. Am. Chem. Soc.* **2017**, *139*, 1432−1435.

(19) Steirer, K. X.; Schulz, P.; Teeter, G.; Stevanovic, V.; Yang, M.; Zhu, K.; Berry, J. J. Defect Tolerance in Methylammonium Lead Triiodide Perovskite. *ACS Energy Lett.* **2016**, *1*, 360−366.

(20) Walsh, A.; Scanlon, D. O.; Chen, S.; Gong, X. G.; Wei, S. H. Self-Regulation Mechanism for Charged Point Defects in Hybrid Halide Perovskites. *Angew. Chem., Int. Ed.* **2015**, *54*, 1791−4.

(21) Eames, C.; Frost, J. M.; Barnes, P. R.; O'Regan, B. C.; Walsh, A.; Islam, M. S. Ionic Transport in Hybrid Lead Iodide Perovskite Solar Cells. *Nat. Commun.* **2015**, *6*, 7497.

(22) Ni, Z.; Bao, C.; Liu, Y.; Jiang, Q.; Wu, W.-Q.; Chen, S.; Dai, X.; Chen, B.; Hartweg, B.; Yu, Z.; Holman, Z.; Huang, J. Resolving Spatial and Energetic Distributions of Trap States in Metal Halide Perovskite Solar Cells. *Science* **2020**, *367*, 1352−1358.

(23) Mahmud, M. A.; Duong, T.; Yin, Y.; Pham, H. T.; Walter, D.; Peng, J.; Wu, Y.; Li, L.; Shen, H.; Wu, N.; Mozaffari, N.; Andersson, G.; Catchpole, K. R.; Weber, K. J.; White, T. P. Double-Sided Surface Passivation of 3d Perovskite Film for High-Efficiency Mixed-Dimensional Perovskite Solar Cells. *Adv. Funct. Mater.* **2020**, *30*, 1907962.

(24) Akin, S.; Arora, N.; Zakeeruddin, S. M.; Grätzel, M.; Friend, R. H.; Dar, M. I. New Strategies for Defect Passivation in High-Efficiency Perovskite Solar Cells. *Adv. Energy Mater.* **2020**, *10*, 1903090.

(25) Liu, N.; et al. Extremely Low Trap-State Energy Level Perovskite Solar Cells Passivated Using Nh2-Poss with Improved Efficiency and Stability. *J. Mater. Chem. A* **2018**, *6*, 6806−6814.

(26) Zarazua, I.; Bisquert, J.; Garcia-Belmonte, G. Light-Induced Space-Charge Accumulation Zone as Photovoltaic Mechanism in Perovskite Solar Cells. *J. Phys. Chem. Lett.* **2016**, *7*, 525−8.

(27) Zarazua, I.; Han, G.; Boix, P. P.; Mhaisalkar, S.; Fabregat-Santiago, F.; Mora-Sero, I.; Bisquert, J.; Garcia-Belmonte, G. Surface Recombination and Collection Efficiency in Perovskite Solar Cells from Impedance Analysis. *J. Phys. Chem. Lett.* **2016**, *7*, 5105−5113.

(28) Duan, H.-S.; Yang, W.; Bob, B.; Hsu, C.-J.; Lei, B.; Yang, Y. The Role of Sulfur in Solution-Processed Cu2znsn(S,Se)4and Its Effect on Defect Properties. *Adv. Funct. Mater.* **2013**, *23*, 1466−1471.

(29) Ye, S.; Rao, H.; Zhao, Z.; Zhang, L.; Bao, H.; Sun, W.; Li, Y.; Gu, F.; Wang, J.; Liu, Z.; Bian, Z.; Huang, C. A Breakthrough Efficiency of 19.9% Obtained in Inverted Perovskite Solar Cells by Using an Efficient Trap State Passivator Cu(Thiourea)I. *J. Am. Chem. Soc.* **2017**, *139*, 7504.

(30) Rajagopal, A.; Yang, Z.; Jo, S. B.; Braly, I. L.; Liang, P.-W.; Hillhouse, H. W.; Jen, A. K. Y. Highly Efficient Perovskite-Perovskite Tandem Solar Cells Reaching 80% of the Theoretical Limit in Photovoltage. *Adv. Mater.* **2017**, *29*, 1702140.

(31) Yang, D.; Zhou, X.; Yang, R.; Yang, Z.; Yu, W.; Wang, X.; Li, C.; Liu, S.; Chang, R. P. H. Surface Optimization to Eliminate Hysteresis for Record Efficiency Planar Perovskite Solar Cells. *Energy Environ. Sci.* **2016**, *9*, 3071−3078.

# 关于国家自然科学基金资助项目批准及有关事项的通知

白阳　先生/女士：

根据《国家自然科学基金条例》的规定和专家评审意见，国家自然科学基金委员会（以下简称自然科学基金委）决定批准资助您的申请项目。项目批准号：21805010，项目名称：界面修饰对二维钙钛矿生长取向的影响及其在太阳能电池中的特性研究，直接费用：27.50万元，项目起止年月：2019年01月至2021年12月，有关项目的评审意见及修改意见附后。

请尽早登录科学基金网络信息系统（https://isisn.nsfc.gov.cn），获取《国家自然科学基金资助项目计划书》（以下简称计划书）并按要求填写。对于有修改意见的项目，请按修改意见及时调整计划书相关内容；如对修改意见有异议，须在计划书电子版报送截止日期前提出。

计划书电子版通过科学基金网络信息系统（https://isisn.nsfc.gov.cn）上传，由依托单位审核后提交至自然科学基金委进行审核。审核未通过者，返回修改后再行提交；审核通过者，打印为计划书纸质版（一式两份，双面打印），由依托单位审核并加盖单位公章后报送至自然科学基金委项目材料接收工作组。计划书电子版和纸质版内容应当保证一致。向自然科学基金委提交和报送计划书截止时间节点如下：

1、提交计划书电子版截止时间为**2018年9月11日16点**（视为计划书正式提交时间）；

2、提交计划书电子修改版截止时间为**2018年9月18日16点**；

3、报送计划书纸质版截止时间为**2018年9月26日16点**。

**请按照以上规定及时提交计划书电子版，并报送计划书纸质版，未说明理由且逾期不报计划书者，视为自动放弃接受资助。**

附件：项目评审意见及修改意见表

国家自然科学基金委员会

化学科学部

2018年8月16日

**附件：项目评审意见及修改意见表**

| 项目批准号 | 21805010 | 项目负责人 | 白阳 | 申请代码1 | B050804 |
|---|---|---|---|---|---|
| 项目名称 | 界面修饰对二维钙钛矿生长取向的影响及其在太阳能电池中的特性研究 ||||||
| 资助类别 | 青年科学基金项目 || 亚类说明 ||||
| 附注说明 ||||||
| 依托单位 | 北京理工大学 |||||
| 直接费用 | 27.50 万元 || 起止年月 | 2019年01月 至 2021年12月 |||

通讯评审意见：

〈1〉该项目拟开展界面修饰对二维钙钛矿多晶薄膜生长行为，结晶取向，质量及界面载流子分离的影响方面的研究，探讨相关电荷传输机制，及对器件效率的影响。该项目立足于二维钙钛矿层的界面修饰，思路具有较好的创新性，所用方法具有先进性，申请人前期在相关领域的研究亦具有较为系统性的研究积累。研究内容与研究方案套话术语过多，内容过于简略。

〈2〉项目申请提出对基材进行界面分子修饰来调整二维钙钛矿晶体生长，拟研究界面修饰对二维钙钛矿晶体结构和取向的影响，界面诱导的不同取向和载流子界面分离行为，二维钙钛矿结构和取向对载流子传输的影响规律。

建议予以资助。

1. 申请者提出进行基于NiO基底的研究出发点应该明确指出

2. 钙钛矿沉积过程是个快速/复杂过程，研究可以集中在原子级平整基底进行，在获得规律基础上进行一定的拓展。自然科学基金不是支持我们去做高效率的事情，而是要提出科学问题进行相应的研究。二维钙钛矿晶体薄膜的生长是高性能器件的关键。但是如果我们还是在比较粗糙的基底上研究这种基础研究，很可能得到还是以效率为指标来衡量界面修饰的效果，这往往就局限了研究的价值 '

3. 申请者并未给出如何能够修饰NiO基底的材料体系，并且给出二维钙钛矿的材料体系，及其这两种体系间的相互作用机制等。

4. 申请者提出的研究手段和技术方案和常规三维钙钛矿电池材料研究无异，体现不出研究的价值

〈3〉该项目希望控制钙钛矿的生长取向，获得垂直的二维钙钛矿层，从而在保证高效率的基础上，提升钙钛矿电池的稳定性。三维的钙钛矿吸光强，激子和电荷传输快，容易实现高的光电转换效率，但是，三维钙钛矿极易受到外界水等因素的影响，造成晶体破坏，材料分解，器件性能下降。而二维钙钛矿中含有较大的有机分子，稳定性强，不过，二维钙钛矿一般都是平行于基底生长的，较大的有机分子阻隔了激子和载流子在垂直方向的传输，光电转换效率往往较低。项目通过界面修饰来控制生长方向，获得的垂直于基底的二维钙钛矿兼顾了效率和稳定性，创新性强，具有较好的科学意义，研究思路明确，设计的技术路线合理，可行性高，研究基础较好，有望取得重要的研究成果，建议优先资助。

修改意见：

化学科学部

2018年8月16日

# 重点实验室开放课题任务书

## （2019 年）

| | |
|---|---|
| 课 题 名 称： | 调控二维钙钛矿生长取向及其对太阳能电池性能和稳定性影响研究 |
| 甲　　　方： | 广东省纳米微米材料研究重点实验室 |
| 甲方所在单位： | 北京大学深圳研究生院 |
| 乙　　　方<br>（项目负责人）： | 白阳 |
| 乙方所在单位： | 北京理工大学 |
| 联 系 电 话： | 13436513387 |
| 起 止 年 限： | 2019 年 3 月 至 2020 年 2 月 |

广东省纳米微米材料研究重点实验室制

二〇一九年二月

首页　申请与受理　项目批准　在研与结题　**查询与统计**　管理

项目信息查询 ▼　项目经费信息查询 ▼

全文反馈意见查询 | **批准项目综合查询** |

| 项目批准号 ▼ | | 项目名称 ▼ | | 项目年度 ▼ 2021 | | 隐藏查询 ≫ |

| 申请代码1 ▼ | | ☐模糊 | 依托单位 ▼ | | 姓名 ▼ | |

| 资助类别 ▼ | | 附注说明 ▼ | | 关键词 ▼ | |

🔍 查询　重置

**金额总计：58.00**

| 批准号 / 项目名称 / 姓名 / 依托单位 / 资助类型 / 申请代码1 / 批准经费 （万元） | 项目起止年月 |
| --- | --- |
| 52172182， 钙钛矿材料阳离子相分离行为调控与稳定性研究 白阳， 北京理工大学 面上项目，E0208，58.00 | 2022-01 - 2025-12 |

---

项目详细信息 - Google Chrome　　　　　　　　　　　　　— ☐ ✕

🔒 isisn.nsfc.gov.cn/egrantweb/view/view-project?prjNo=XUFO%2FEskEkIbftboq1OVSbIyxQmI09%2FCrYucFgQNsFeY0rew57kqWA%3D...

| 项目批准号： | **52172182** |
| 负责人： | **白阳** |
| 项目名称： | 钙钛矿材料阳离子相分离行为调控与稳定性研究 |

**项目基本信息**　项目摘要　人员信息　研究成果　相关文件　间接费用拨款计划

| 资助类别： | 面上项目 | 亚类说明： | |
| --- | --- | --- | --- |
| 附注说明： | | | |
| 项目批准号： | 52172182 | 申请代码1： E0208 | 申请代码2： E02 |
| 项目名称： | **钙钛矿材料阳离子相分离行为调控与稳定性研究** | | |
| 英文名称： | The Cations Segregation Manipulation and Stability Improvement of Perovskite Materials | | |
| 单位名称： | 北京理工大学 | | |
| 项目批准文件号： | | | |
| 院系所： | 材料学院 | | |
| 合作研究单位： | | | |
| 负责人： | **白阳** | 职称： | 副研究员 |
| 资助金额： | 58万元 | 研究性质： | 起止年月： 2022.01 - 2025.12 |

**登分册点名册打印** 2019-2020学年 1学期 更改

| 课程号 | | 课程名 | | 课序号 | | 开课单位 | 请选择... | | 课程性质 | 请选择... | |
|---|---|---|---|---|---|---|---|---|---|---|---|
| 课程类别 | 请选择... | 学分 | | — | | 学时 | | — | | 上课教师 | |
| 课容量 | | 选课总人数 | | | | 上课班级 | | | | | |

搜索

清空条件 | 更多条件 收起 >

打印点名册 | 打印登分册 | 导出

| | 操作 | 课程号 | 课程名 | 课序号 | 开课单位 | 课程性质 | 课程类别 | 学分 | 学时 | 上课教师 | 上课班级 | 课容量 | 选课总人数 |
|---|---|---|---|---|---|---|---|---|---|---|---|---|---|
| ☐ | 点名册 \| 登分册 | 100091222 | 新能源材料与... | 2019100091... | 材科学院 | 选修 | 专业课 | 2 | 32 | 白阳[6120180129],陈棋[6120160008] | 09111602 | 14 | 14 |

**登分册点名册打印** 2020-2021学年 1学期 更改

| 课程号 | | 课程名 | | 课序号 | | 开课单位 | 请选择... | | 课程性质 | 请选择... | |
|---|---|---|---|---|---|---|---|---|---|---|---|
| 课程类别 | 请选择... | 学分 | | — | | 学时 | | — | | 上课教师 | |
| 课容量 | | 选课总人数 | | | | 上课班级 | | | | | |

搜索

清空条件 | 更多条件 收起 >

打印点名册 | 打印登分册 | 导出

| | 操作 | 课程号 | 课程名 | 课序号 | 开课单位 | 课程性质 | 课程类别 | 学分 | 学时 | 上课教师 | 上课班级 | 课容量 | 选课总人数 |
|---|---|---|---|---|---|---|---|---|---|---|---|---|---|
| ☐ | 点名册 \| 登分册 | 100091222 | 新能源材料与... | 211001473 | 材科学院 | 选修 | 专业课 | 2 | 32 | 白阳[6120180129],陈棋[6120160008] | 09111702 | 13 | 13 |

☐ **[开课课程]列表**

| | 开课学年 | 开课学期 | 教学班名称 | 课程代码 | 课程中文名称 | 课程类别 | 开课单位 | 授课教师 | 实际上课人数 | 成绩状态 | 是否上传教... | 是否停开 | 是否禁选 | 发布状态 | 提交人 | 提交时间 |
|---|---|---|---|---|---|---|---|---|---|---|---|---|---|---|---|---|
| ☐ | 2019-2020 | 第一学期 | 1 | 0901001 | (英)固体化学 | 专业课 | 材科学院 | 徐萌,白阳 | 40 | 已提交 | 否 | 否 | 否 | 已发布 | 徐萌(10.0.6... | 2020-02-28... |

# 界面改性对钙钛矿太阳能电池降解路径调控
# 及机制探究

| | |
|---|---|
| 作 者 姓 名 | 章骁 |
| 学 院 名 称 | 材料学院 |
| 指 导 教 师 | 白阳  副研究员 |
| 答辩委员会主席 | 胡劲松  研究员 |
| 申 请 学 位 | 工学硕士 |
| 学 科 专 业 | 材料科学与工程 |
| 学位授予单位 | 北京理工大学 |
| 论文答辩日期 | 2021 年 6 月 |

# 钙钛矿薄膜结晶动力学的研究及高效率太阳能电池制备

| | |
|---|---|
| 作 者 姓 名 | 刘 娜 |
| 学 院 名 称 | 材料学院 |
| 指 导 教 师 | 李煜璟副教授 |
| 答辩委员会主席 | 薄志山教授 |
| 申 请 学 位 | 工学博士 |
| 学 科 专 业 | 材料科学与工程 |
| 学位授予单位 | 北京理工大学 |
| 论文答辩日期 | 2021 年 6 月 |

中图分类号：O793
UDC 分类号：540

# 钙钛矿太阳能电池材料微结构与光电性能调控

作者姓名      <u>朱    城</u>

学院名称      <u>材料学院</u>

指导教师      <u>陈棋教授</u>

答辩委员会主席      <u>薄志山教授</u>

申请学位      <u>工学博士</u>

学科专业      <u>材料科学与工程</u>

学位授予单位      <u>北京理工大学</u>

论文答辩日期      <u>2021 年 6 月</u>

Journal of Renewable Materials

☞ Make Submissions

☐ Propose a Special Issue

## Journal Menu

- JRM Homepage
- Aims and Scope
- Indexing & Abstracting
- About Editors
- Editorial Board
- Instructions for Authors
- Article Processing Charge
- Editorial Workflow
- Publication Ethics
- Contact Information

## Special Issues Menu

- All Special Issues
- Open Special Issues
- Closed Special Issues

## All Issues

- 📁 Online First
- ▶ 📁 2022
- ▶ 📁 2021
- ▶ 📁 2020
- ▶ 📁 2019
- ▶ 📁 2018
- ▶ 📁 2017
- ▶ 📁 2016
- 📁 Back Issues

**PORTICO**

All of TSP's content is archived in Portico

available online at **ingenta** CONNECT

## Special Issue "Perovskite Solar Cells"

**Submission Deadline: 30 November 2021**

**Submit to Special Issue**

### Guest Editors

Haining Chen, Associate Professor, School of Materials Science and Engineering, Beihang University, Beijing, China.
Dr. H.N. Chen obtained his PhD degree from Beihang University in 2013 following which he worked as a postdoctoral fellow at The Hong Kong University of Science and Technology. He is working at Beihang University since 2016. He specializes in organic-inorganic hybrid perovskite solar cells, inorganic perovsktie solar cells, quantum dot solar cells, photoelectrochemical cells, water splitting, luminescence materials. He has published more than 90 peer-reviewed articles and 10 patents, with his H-Index of 39.

Zhanhua Wei, Professor, College of Materials Science & Technology, Huaqiao University, Xiamen, China.
Dr. Z.H Wei obtained his PhD degree from The Hong Kong University of Science and Technology in 2015 following which he worked as a postdoctoral fellow at Nanyang Technological University. He is working at Huaqiao University since 2016. He specializes in the synthesis of perovskite materials, perovskite light-emitting diodes, perovskite solar cells, and other optoelectronic devices. He has published more than 60 peer-reviewed articles, with his H-Index of 31.

Yang Bai, Assistant Professor, School of Materials Science and Engineering, Beijing Institute of Technology Beijing, China.
Dr. Bai obtained his B.Sc degree from Beihang University in 2013 and PhD degree from The Hong Kong University of Science and Technology in 2017, following which he worked as a postdoctoral fellow at The Hong Kong University of Science and Technology. He is working at Beijing Institute of Technology since 2018. He specializes in hybrid organic-inorganic halide perovskite solar cells, low-dimensional materials, interfacial design of semiconductor, nanomaterials. He has published more than 50 peer-reviewed articles, with his H-Index of 29.

Teng Zhang, Associate Professor, School of Materials Science and Engineering, China University of Petroleum, Qingdao, China.
Dr. T. Zhang is an Associate Professor of the China University of Petroleum. He received his PhD degree in Nanoscience and Nanotechnology in 2017 from the Hong Kong University of Science and Technology (HKUST). Then he stayed in HKUST for 2 years of Post-Doc research before joining the China University of Petroleum in 2019. Dr. Zhang is specialized in solar conversion materials especially solar cells and photocatalysis.

### Summary

The increasing environmental concerns and decreasing petroleum resources have made it necessary and urgent to develop various kinds of renewable sources. Solar energy is one of the most promising alternatives and as a result, solar cells that could convert solar energy to electric energy have been widely developed. However, due to the high cost of Si-based solar cells, the applications of solar cells have been greatly inhibited. Very recently, perovskite solar cells (PSCs) have shown great promise to solve the above problem because high power conversion efficiency (PCE) could be easily achieved by simple and low-cost solution-based processes. In the last decade, the PCE of PSCs has been rapidly boosted from original 3.8% to over 25%. Besides, various device structures and perovskite materials have been exploited for PSCs, which would help expand the application fields of PSCs. This Special Issue " Perovskite Solar Cells " covers the development of PSCs with different device structures. The scope of interests includes but is not limited to the following topics:

(1) Organic-inorganic hybrid perovskite solar cells
(2) Inorganic perovskite solar cells
(3) 2D perovskite solar cells
(4) Lead-free perovskite solar cells
(5) Perovskite solar cells based on carbon electrodes
(6) Tandem perovskite solar cells
(7) Perovskite solar cells with other structures

### Keywords

Organic-inorganic hybrid perovskite; Inorganic perovskite; 2D perovskite; Lead-free perovskite; Carbon electrode; Tandem structure.

## Invitation to review for Materials Today Energy

**ME** em.mtener.0.6c5608.7a12ce5f@editorialmanager.com 代表
Materials Today Energy <em@editorialmanager.com>
周四 2020/7/2 9:22
收件人: Yang Bai <mse.ybai@bit.edu.cn>

Manuscript Number: MTENER-D-20-00359
The effect of the ambient oxygen on operation of sputtered NiOx hole transport layer for planar type MAPbI3 perovskite solar cells
Hae-Jun Seok; Jin-Hyeok Park; Ahra Yi; Hanbin Lee; Hyo Jung Kim, Ph.D; Han-Ki Kim, Ph.D

Dear Dr Bai,

I would like to invite you to review the above referenced manuscript submitted by Professor Han-Ki Kim, as I believe it falls within your expertise and interest. The abstract for this manuscript is included below.

You should treat this invitation, the manuscript and your review as confidential. You must not share your review or information about the review process with anyone without the agreement of the editors and authors involved, even after publication. This also applies to other reviewers' "comments to author" which are shared with you on decision (and vice versa).

Please respond to this invitation at your earliest opportunity.

If you would like to review this paper, please click this link:
https://www.editorialmanager.com/mtener/l.asp?i=61564&l=OPMFAU3V

If you have a conflict of interest or do not wish to review this paper, please click this link:
https://www.editorialmanager.com/mtener/l.asp?i=61565&l=H0B6VLVK

If you decline to review, I would appreciate your suggestions for alternate reviewers.

If, for any reason, the above links do not work, please log in as a reviewer at https://www.editorialmanager.com/mtener/.

Since timely reviews are of utmost importance to authors, I would appreciate receiving your review within 14 days of accepting this invitation.

I hope you will be able to review this manuscript.

## Invitation to review for Materials Advances - MA-ART-07-2021-000650

**MA** Materials Advances <onbehalfof@manuscriptcentral.com>
周日 2021/8/8 8:00
收件人: Yang BAI

08-Aug-2021

Dear Dr Bai:

TITLE: Fast Non-ambipolar Diffusion of Charge Carriers and the Impact of Traps and Hot Carriers on it in CSMAFA Perovskite and GaAs
AUTHORS: Pasanen, Hannu; Liu, Maning; Kahle, Hermann; Vivo, Paola; Tkachenko, Nikolai
(See below for abstract )

I invite you to review this manuscript, which has been submitted for publication in Materials Advances, published by the Royal Society of Chemistry.

At Materials Advances we aim to provide a rapid service for our authors. Therefore, please respond to this invitation by clicking on the appropriate link below within 3 days of receiving this email, and provide your report within 10 days of agreeing (7 days for communications and 14 days for reviews). If you need longer to provide your report please let me know. If you are unable to review at this time, I would be grateful if you could recommend another expert reviewer.

*** PLEASE NOTE: This is a two-step process. After clicking on the link, you will be directed to a webpage to confirm. ***

Agreed: https://mc.manuscriptcentral.com/ma?URL_MASK=6f706c01b7a949b699ae1c5833145361

Declined - other reason: https://mc.manuscriptcentral.com/ma?URL_MASK=ec7d3e33631a43a6839a68d22ce8e4eb

Declined - out of expertise: https://mc.manuscriptcentral.com/ma?URL_MASK=e751d2df85ba45569a6d073bc2c12405

Once you accept the invitation to review this manuscript, you will receive a second email giving you access to the manuscript and our reviewer guidelines.

Please read our Ethical Guidelines which contain full information on the responsibilities of reviewers:

https://www.rsc.org/journals-books-databases/journal-authors-reviewers/reviewer-responsibilities/

Please note that:
- your anonymity as a reviewer will be strictly preserved;
- you have the responsibility to treat the manuscript and any communications on the manuscript as confidential;
- the manuscript (or its existence) should not be shown to, disclosed to, or discussed with others, except in special cases, where specific scientific advice may be sought.

**Invitation to review for Journal of Physics and Chemistry of Solids**

J  em.pcs.0.707d64.e61fcb0f@editorialmanager.com 代表
Journal of Physics and Chemistry of Solids <em@editorialmanager.com>
周四 2021/1/7 11:21
收件人: Yang BAI

Manuscript Number: PCS-D-20-00347

Effect of defects on homojunction perovskite solar cells

Youpeng Xiao

Dear Dr. Bai,

I would like to invite you to review the above-referenced manuscript. To maintain our journal's high standards we need the best reviewers, and given your expertise in this area I would greatly appreciate your contribution.

You should treat this invitation, the manuscript and your review as confidential. You must not share your review or information about the review process with anyone without the agreement of the editors and authors involved, even after publication. This also applies to other reviewers' "comments to author" which are shared with you on decision (and vice versa).

Please respond to this invitation at your earliest opportunity.

If you would like to review this paper, please click this link:
https://www.editorialmanager.com/pcs/l.asp?i=196687&l=7GMEVOAI

If you have a conflict of interest or do not wish to review this paper, please click this link:
https://www.editorialmanager.com/pcs/l.asp?i=196688&l=0QRE384G

If you decline to review I would appreciate your suggestions for alternate reviewers.

If, for any reason, the above links do not work, please log in as a reviewer at https://www.editorialmanager.com/pcs/

Since timely reviews are of utmost importance to authors, I would appreciate receiving your review within 14 days of accepting this invitation.

---

**Invitation to Review Short Manuscript jz-2019-034136**                    📎 2 ⌄

T  The Journal of Physical Chemistry Letters <onbehalfof@manuscriptcentral.com>
周五 2019/11/22 11:50
收件人: mse.ybai@bit.edu.cn
抄送: zhong-office@jpclett.acs.org

| 📄 Attached standard file:... ⌄ | 📄 Attached standard file:... ⌄ |
| 79 KB | 82 KB |

2 个附件(161 KB)   全部下载   全部保存到 OneDrive - HKUST Connect

21-Nov-2019

Journal:  The Journal of Physical Chemistry Letters
Manuscript ID : jz-2019-034136
Title : "Self-Healing of Photocurrent Degradation in Perovskite Solar Cells: The Role of Defect-Trapped Excitons"
Author(s): Nan, Guangjun; Zhang, Xu; Lu, Gang

Dear Dr. Bai:

We would greatly appreciate your agreeing to review the referenced Letter for The Journal of Physical Chemistry Letters. Letters are short articles that report results whose immediate availability to the scientific community is deemed important.  We would especially appreciate your evaluation on its scientific merit, significance to the field of physical chemistry, and appropriateness for this Journal.

Please note that, due to the large number of papers that we are receiving currently, and our intent to publish only the results of "forefront research" in physical chemistry, we are now asking authors to provide clear evidence in their paper for a "significant advance" in the particular area of physical chemistry concerned. This new criterion for publication is in addition to the various other criteria for publication that are noted on the review form.

We would greatly appreciate it if you would review this manuscript within 10 days.  This will help us expedite the processing of the Letters. If you need additional time please do not hesitate to contact us.

To assist you in making your decision to review, the abstract for this short manuscript is available at the end of this message.

## Invitation to Review Manuscript jp-2020-11119v

**The Journal of Physical Chemistry** <onbehalfof@manuscriptcentral.com>
周二 2020/12/15 8:57
收件人: mse.ybai@bit.edu.cn
抄送: gewirth-office@jpc.acs.org

14-Dec-2020

Journal:  The Journal of Physical Chemistry
Manuscript ID : jp-2020-11119v
Title : "Excitonic Solar Cells Using 2D Perovskite of $(BA)_2(FA)_2Pb_3I_{10}$"
Author(s): Hu, Shu; Yang, Xiao; Yang, Bo; Zhang, Yang; Li, Heng; Sheng, Chuanxiang

COVID-19 Support: Please visit the following website to access important information for ACS authors and reviewers during the COVID-19 crisis:
https://axial.acs.org/2020/03/25/chemists-covid-19-coronavirus/

We are flexible in these unprecedented times affecting the global research community.  If you need more time to complete authoring or reviewing tasks, please contact the editorial office and request an extension.

Dear Dr. Bai:

We would greatly appreciate your agreeing to review the referenced manuscript for The Journal of Physical Chemistry. I would especially like your evaluation on its scientific merit, significance to the field of physical chemistry, and appropriateness for this Journal. To assist you in making your decision to review, the abstract for this manuscript is available at the end of this message.

The hyperlinks below can be used to accept or decline this invitation automatically:

To automatically respond click below:

*** PLEASE NOTE: This is a two-step process. After clicking on the link, you will be directed to a webpage to confirm. ***

Agreed: https://acs.manuscriptcentral.com/acs-jp?URL_MASK=35f00d98b2ee4ccca5f068c71c7e0016

Declined: https://acs.manuscriptcentral.com/acs-jp?URL_MASK=22727dd4366e420e841cd320f4bd6a36

If you are unable to review this manuscript, the decline link will provide you with fields to suggest alternative reviewers (with email addresses). In the comment field, you

## Request To Referee Manuscript cplu.201800481 from Miss. Prof. Dr. Frau Prof. Dr. Erin Chernick et al.

em.cplu.0.5e4982.6bf99a1f@editorialmanager.com 代表
**ChemPlusChem** <em@editorialmanager.com>
周二 2018/10/2 0:11
收件人: Yang BAI

Dear Dr. Bai,

The above-mentioned manuscript has been submitted for publication as a Communication in ChemPlusChem. We kindly request your assistance in evaluating the quality of the manuscript.

Please find below further details on 1) the manuscript abstract and PDF, 2) responding to this invitation, and 3) quality criteria to ensure the highest quality, originality, relevance, significance, and validity. Note that as a referee you have the responsibility to treat the manuscript and your report as confidential.

The editorial office is aware of the very large number of review requests that researchers receive, possibly one or more per day from different journals and/or publishers. Also on behalf of the authors, we greatly appreciate your consideration, time, and effort.

With kind regards,
Dr. Marisa Spiniello
Editor
ChemPlusChem

_____

ChemPlusChem is a ChemPubSoc Europe journal published by Wiley-VCH
Impact Factor: 3.20
Ranked 64/171 (Chemistry, Multidisciplinary)
2017 Journal Citation Reports® (Clarivate Analytics, 2018)

<a href="http://onlinelibrary.wiley.com/doi/10.1002/cplu.v83.1/issuetoc">Issue 1, 2018</a> is free to read

Download the new multi-journal app with Angewandte Chemie, Chemistry – A European Journal and more: <a href="https://itunes.apple.com/de/app/chempubsoc-europe/id1276511515">Apple iOS</a> and <a href="https://play.google.com/store/apps/details?id=com.wiley.jas.cpse">Android</a>.

Wiley-VCH

**Reviewer Invitation for TSF-D-20-01298**

em.tsf.0.6f804b.d50b06d7@editorialmanager.com 代表
Thin Solid Films <em@editorialmanager.com>
周二 2020/11/24 10:24
收件人: Yang Bai <mse.ybai@bit.edu.cn>

Ref. No.: TSF-D-20-01298
Title: Grain size control of perovskite films based on β-alanine self-assembled monolayers surface treatment
submitted to Thin Solid Films

Dear Bai,

The manuscript described below has been submitted for publication as a Full Length article in Thin Solid Films. I would be grateful if you could review the paper described below and send your comments to me. Your comments on the scientific merit of this paper and its suitability for publication will be greatly appreciated.

The abstract and a direct link to the complete version of the manuscript are included below. The contents of the manuscript are, of course, confidential until published. A review form is available on the Editorial Manager.

Please confirm that you can or cannot review this manuscript using the link below. If you accept this invitation, we would appreciate receiving your comments within 21 days following your acceptance. If you are unable to act as a reviewer at this time, I would greatly appreciate your suggestions for other potential reviewers.

To accept this invitation, please click here:
https://www.editorialmanager.com/tsf/l.asp?i=831877&l=HG3822GB

To decline this invitation, please click here:
https://www.editorialmanager.com/tsf/l.asp?i=831878&l=G1J8FNYB

As a reviewer you are entitled to complimentary access to references, abstracts, and full-text articles on ScienceDirect and Scopus for 30 days. Full details on how to claim your access via Reviewer Hub (reviewerhub.elsevier.com) will be provided upon your acceptance of this invitation to review.

Please visit the Elsevier Reviewer Hub (reviewerhub.elsevier.com) to manage all your refereeing activities for this and other Elsevier journals on Editorial Manager.

I look forward to hearing from you in the near future.